EBERHARD KARLS
UNIVERSITÄT
TÜBINGEN

UNIVERSITÀ DEGLI STUDI
DI TRENTO


EBERHARD-KARLS-UNIVERSITÄT
TÜBINGEN
Fakultät für Mathematik und Physik

UNIVERSITÀ DEGLI STUDI
DI TRENTO
Facoltà di Scienze MM. FF. e NN.


**Diplomarbeit - Elaborato finale**

Diplomstudiengang Physik - Corso di laurea specialistica in fisica

# *A detailed analysis of the galactic TeV source HESS J1804-216*

**Eine detaillierte Analyse der galaktischen TeV Quelle HESS J1804-216**

**Un'analisi dettagliata della sorgente galattica TeV HESS J1804-216**


Betreuer: Prof. Dr. Andrea Santangelo
Relatore: Prof. Dr. Ignazio Lazzizzera

A.A. 2008/2009

Diplomand/Laureando: Gabriele Cologna

Kepler center - IAAT Tübingen
June 2009



EBERHARD-KARLS-UNIVERSITÄT
TÜBINGEN
Fakultät für Mathematik und Physik

UNIVERSITÀ DEGLI STUDI
DI TRENTO
Facoltà di Scienze MM. FF. e NN.

# *A detailed analysis of the galactic TeV source HESS J1804-216*

Diplomarbeit / Elaborato finale

Diplomstudiengang Physik - Corso di laurea specialistica in fisica
A.A. 2008/2009

***Gabriele Cologna***

A tutti quelli che
mi hanno sostenuto ed aiutato.

# Abstract

H.E.S.S. (High Energy Stereoscopic System) is an array of four Imaging Atmospheric Cerenkov Telescopes located in Namibia in the Khomas Highlands and is designed to detect very high energy (VHE $>$ 100 GeV) $\gamma$-rays in the energy range up to 100 TeV by looking at the Cherenkov light emitted in the air showers induced by the interaction of such VHE $\gamma$-rays with the atmosphere.

The VHE $\gamma$-ray source HESS J1804-216 was discovered in the inner part of the Galactic Plane by H.E.S.S. during the 2004-2005 Galactic Plane survey and has revealed to be one of the largest, brightest and softest known sources, with a flux about 25% of the Crab Nebula above 200 GeV. Its dimensions and structure, together with the presence of the energetic pulsar PSR B1800-21 in the emission region, make of it a possible candidate for a Pulsar Wind Nebula. Taking into account the new 2006-2007 dataset, a morphological and a spectral analysis are performed, confirming the already published results. In particular, the dataset allows to look for gradients in the spectral index through a spatially resolved spectral analysis. The results show a possible composite nature of HESS J1804-216 and indicate that PSR B1800-21 is probably physically associated to the TeV emission region, since a hardening in the spectrum is visible towards its position.

# Contents

# Introduction

TeV $\gamma$-ray astronomy is quite a new branch in astrophysics. Only with the advent of the current generation of TeV telescopes such as the High Energy Stereoscopic System (H.E.S.S.), sufficient sensitivity was achieved to allow for surveys of significant fractions of the sky. As an obvious choice, the Galactic plane was the first area which was scanned with the H.E.S.S. telescopes. This survey revealed several tens of TeV $\gamma$-ray sources, which in many cases could not be unambiguously identified with known objects. The identification of these sources is challenging. In many cases, the counterparts may not have been detected yet because the sky was not looked at with sufficient sensitivity in lower frequency bands. However, some TeV sources are co-located with one or several plausible counterparts, but a unique identification with one of those is not unambiguously possible yet.

The work presented here was carried out to improve the quality of the TeV characterisation of one of those unidentified TeV sources, HESS J1804-216, which belongs to the class of sources where multiple counterparts exist. Since the source is substantially extended beyond the point spread function of H.E.S.S., the data set analyzed allows for a morphological characterisation of the TeV source, which has not been achieved before. The goal of the studies is to help identifying the TeV source with one (or possibly several) of the known counterparts.

In the first chapter the radiative processes and the hadronic interactions that lead to the VHE $\gamma$-ray emission will be explained as well as the particle acceleration mechanisms. The physical objects in which such acceleration can take place will also be described. At last, simplified models of the air showers responsible for the emission of the Cherenkov light detected by the Imaging Atmospheric Cherenkov Telescopes like H.E.S.S. will be presented. In the second chapter an introduction to the Imaging Atmospheric Cherenkov technique will be done and the H.E.S.S. telescope system will be described in detail as well as the data collection and event reconstruction methods. In the third chapter the techniques used for the spectral and morphological data analysis will be described and particular attention will be given to the background estimation methods. The fourth chapter will be dedicated to the description and analysis of the unidentified VHE $\gamma$-ray source HESS J1804-216. The possible counterparts suggested in the literature will also be briefly presented. Besides the standard morphological and spectral analysis a spatially resolved spectral analysis will be performed and an alternative method to the standard background estimation for the spectral analysis will be studied systematically. Taking into account the obtained results some considerations on the possible counterparts of HESS J1804-216 will be done. In the final chapter the whole work will be summarized.

# 1

# Theory

When looking at photons coming from some kind of source, one may want to know which kind of process did create such photons[1]. The radiation is usually divided in thermal and non-thermal. Thermal radiation is emitted by matter in thermal equilibrium and the radiated spectrum is described by the blackbody. For a certain temperature $T$ it is described by the Planck Law, that gives the emitted power per unit of emitting area, per unit of solid angle, and per unit of frequency [Rybicki and Lightman, 1979]:

$$B_\nu(T) = \frac{2h\nu^3}{c^2} \cdot \frac{1}{\exp^{\frac{h\nu}{kT}} - 1} \;\leftrightarrow\; B_\lambda(T) = \frac{2hc^2}{\lambda^5} \cdot \frac{1}{\exp^{\frac{hc}{\lambda kT}} - 1}, \tag{1.1}$$

remembering that $B_\lambda d\lambda = B_\nu d\nu$. Here are $\nu$ the frequency ($\lambda$ the wavelength), $h$ the Plank constant, $k$ the Boltzmann constant and $c$ the speed of light. In the limit of low frequencies (small energies, $h\nu \ll kT$) one obtains the classical limit of the Rayleigh-Jeans Law (straight-line part of the plot in Fig. 1.1), allowing, if integrated for all frequencies, the *ultraviolet catastrophe*, since the integral would diverge. The high frequency limit gives a pure quantistic result that avoid the divergence [Rybicki and Lightman, 1979]:

$$\begin{cases} h\nu \ll kT \quad B_\nu^{RJ}(T) = \frac{2\nu^2}{c^2} kT \quad \text{Rayleigh-Jeans Law} \\ \\ h\nu \gg kT \; B_\nu^{W}(T) = \frac{2\nu^3}{c^2} \exp^{-\frac{h\nu}{kT}} \qquad \text{Wien Law} \end{cases} \tag{1.2}$$

In the universe, the hottest objects have a thermal emission in the soft X-ray range up to $\sim$10 keV. Therefore, when going to hard X-rays ($\sim$10-100 keV), soft $\gamma$-rays ($\sim$100 keV - 1 MeV), high energy (HE) $\gamma$-rays ($\sim$ MeV-GeV) and very high energy (VHE) $\gamma$-rays ($\sim$50 GeV-100 TeV) one has to look for other processes that are able to create photons at such energies. This is the range of non-thermal radiation, in which photons are emitted or scattered to higher energies by populations of high energy particles (cosmic rays - CR) after their interaction with a magnetic field or with other local particles or photons. Moreover, another evidence for a different kind of process taking place is the spectral shape of the photon distribution, which follows the power-law shape of the primordial CR spectrum $dN/dE \propto E^{-\Gamma}$.

[1] For a more detailed discussion about the arguments presented in this chapter see e.g. [Heitler, 1954], [Rybicki and Lightman, 1979], [Longair, 1992], [Longair, 1994], [Pohl, 2002].

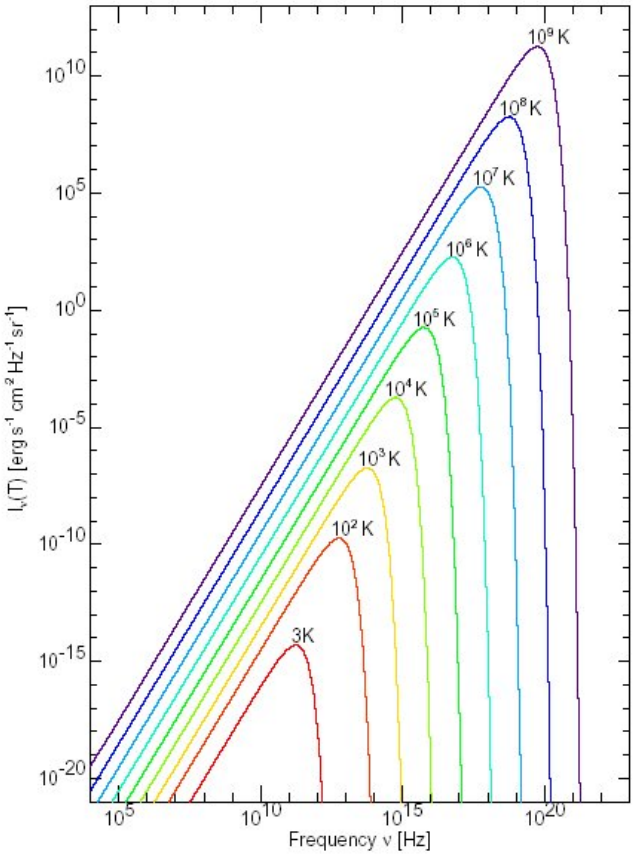


**Fig. 1.1.** Blackbody spectrum at various temperatures (J. Wilms).

## 1.1 Radiative processes

In the following the radiative processes through which CR are able to emit $\gamma$-rays will be described. Interactions between them and the interstellar medium or electromagnetic fields have to occur in order to permit the emission.

### 1.1.1 Inverse Compton

The scattering interaction between a flux of high energy electrons with low energy photons is known as Inverse Compton (IC). In this process after each interaction in average the photons increase their energy proportionally to their initial energy [Longair, 1992]

$$h\nu = \frac{4}{3}\gamma^2 \left(h\nu\right)_0 , \tag{1.3}$$

where $\gamma$ is the Lorentz factor of the electron. It easy to see that in case of high values of $\gamma$ ($\sim$100-1000) this process is really efficient, since it is able to scatter infrared and optical photons from diffuse galactic dust background and starlight up to the X-ray, soft $\gamma$-ray range after a single interaction. The production of VHE $\gamma$-rays is dominated by IC with the cosmic microwave

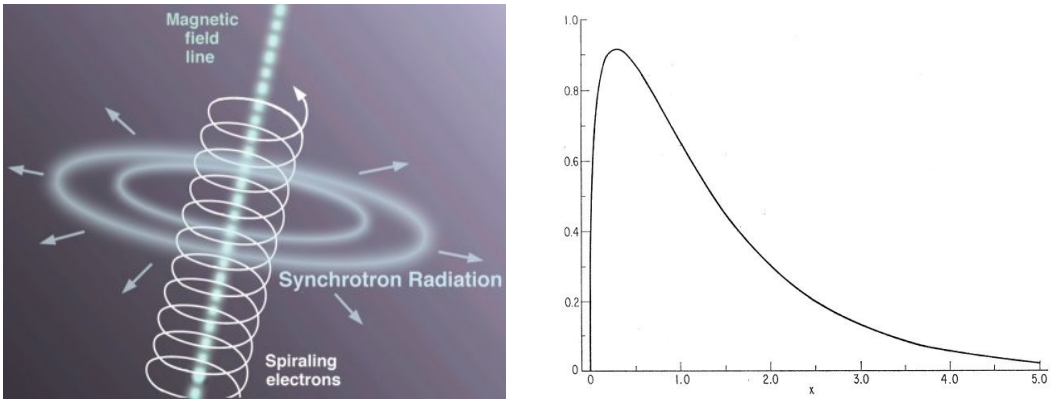


(a) (b)

**Fig. 1.2.** (a) Representation of the synchrotron process. (b) Synchrotron spectrum from a single electron as a function of $x = \nu/\nu_c$ (from [Blumenthal and Gould, 1970]).

background radiation (CMB). The power emitted by the electrons in the case of an isotropic photon distribution is [Longair, 1992]

$$\left(\frac{dE}{dt}\right)_{IC} = P_{IC} = \frac{4}{3}\sigma_T c\beta^2\gamma^2 U_{rad}, \tag{1.4}$$

where $\beta = v/c$, $\sigma_T = 8/3\pi r_0^2$ is the Thomson cross section ($r_0 = e^4/m^2c^4$ is the classical electron radius) and $U_{rad}$ is the radiation energy density of the photon field before the scattering. The spectral emissivity of relativistic high energy electrons scattering a monochromatic isotropic photon field with frequency $\nu_0$ and number density $N(\nu_0)$ is [Longair, 1992]

$$I(\nu)\, d\nu = \frac{3\sigma_T c}{16\gamma^4}\frac{N(\nu_0)}{\nu_0^2}\nu\left[2\nu\ln\left(\frac{\nu}{4\gamma^2\nu_0}\right) + \nu + 4\gamma^2\nu_0 - \frac{\nu^2}{2\gamma^2\nu_0}\right] d\nu. \tag{1.5}$$

In the low frequency limit the term in the square brackets is constant, hence the photon flux is simply proportional to the frequency ($I(\nu) \propto \nu$).

### 1.1.2 Synchrotron emission

Particles moving in a magnetic field $B$ feel an acceleration perpendicular to the field and will therefore radiate. If the particles are non-relativistic this process is known as cyclotron radiation, if they are relativistic a more complex process known as synchrotron radiation takes place, allowing the emission of high energy photons. The power emitted by an isotropic distribution of relativistic electrons is [Longair, 1992]

$$\left(\frac{dE}{dt}\right)_{sync} = P_{sync} = \frac{4}{3}\sigma_T c\beta^2\gamma^2 U_B, \tag{1.6}$$

where $U_B = B^2/8\pi$ is the magnetic energy density. It is apparent that Eq. 1.6 has the same

form as Eq. 1.4. Therefore, if the synchrotron radiation is emitted by the same population of electrons that emit by IC a correlation between the two emissions can be found. The ratio between radiation losses due to synchrotron emission and IC can be expressed as the ratio between the magnetic field energy density and the photon field energy density:

$$\frac{P_{sync}}{P_{IC}} = \frac{U_B}{U_{rad}}. \tag{1.7}$$

This result is actually valid for arbitrary values of the electron velocity, as long as the Thomson scattering approximation in the rest frame holds. The spectral distribution of a synchrotron emission is quite complex and for a single electron is [Pohl, 2002]

$$I(\nu) \simeq \frac{\sqrt{3}e^3 B_\perp}{mc^2} 1.8 \left(\frac{\nu}{\nu_c}\right)^{1/3} \exp\left(-\frac{\nu}{\nu_c}\right), \tag{1.8}$$

where $B_\perp$ is the normal component of $B$ and

$$\nu_c = \frac{3eB_\perp}{4\pi mc}\gamma^2 \simeq 16MHz \left(\frac{B}{\mu G}\right)\left(\frac{E}{GeV}\right)^2 \tag{1.9}$$

is the characteristic synchrotron frequency. The spectrum has a peak at $\nu \simeq 0.3\nu_c$ and a tail to higher energies (Fig. 1.2). In the more general case the real synchrotron spectrum is a convolution of the single electron synchrotron spectrum with the electron distribution spectrum. For a power-law distribution of electrons $N(E)dE \propto E^{-p}dE$ with spectral index $p$ also the synchrotron spectrum will follow a power-law $I(\nu) \propto \nu^{-s}$ with [Rybicki and Lightman, 1979]

$$s = \frac{p-1}{2}. \tag{1.10}$$

Measuring the spectral index of the synchrotron emission one is therefore able to derive the energy spectrum of the electron distribution. The emitted light has also an high degree of polarization (theoretically up to 75% for the frequency integrated emission of particles of the same $\gamma$) given for a power-law distribution of particles by [Rybicki and Lightman, 1979]

$$\Pi = \frac{p+1}{p+\frac{7}{3}}. \tag{1.11}$$

### 1.1.3 Bremsstrahlung

The bremsstrahlung is important with regards to the $\gamma$-ray emission in air-showers (sec. 1.6). In this process, charged particles undergo an acceleration because of the presence of an electrical field, for example the Coulomb field of another charged particle. Photons can be produced with energies comparable to those of the emitting particle, typically low mass particles like $e^-$ and $e^+$ moving through the field of nuclei, ions or protons. Emission due to interactions of particles of the same kind is zero in first approximation. In the case of small angle scattering, considering a

gas of electrons with density $n_e$ moving with velocity $v$ through a gas of ions with density $n_i$, the total emission per unit of time, per unit of volume, per unit of frequency range is [Rybicki and Lightman, 1979]:

$$\frac{dE}{d\nu dV dt} = \frac{16e^6}{3c^3 m_e^2 v} n_e n_i Z^2 \ln\left(\frac{b_{max}}{b_{min}}\right), \tag{1.12}$$

where $Z$ is the ion's atomic number and $b_{min}$ and $b_{max}$ are the minimum and the maximum impact parameter respectively, i.e. they define the distance range that permit the interaction. One has [Rybicki and Lightman, 1979]

$$\begin{cases} \frac{b_{max}}{b_{min}} = \frac{2\pi^2 m_e v^3}{4Ze^2\nu} & \text{for } \frac{1}{2}m_e v^2 \ll Z^2 Ry \text{ classical limit} \\ \\ \frac{b_{max}}{b_{min}} = \frac{m_e v^2}{h\nu} & \text{for } \frac{1}{2}m_e v^2 \gg Z^2 Ry \end{cases} \tag{1.13}$$

where $Ry = me^4/(2\hbar^2)$ is the Rydberg energy for the hydrogen atom. For the production of VHE $\gamma$-rays one needs relativistic particles. The total energy loss rate in the relativistic case is [Longair, 1992]

$$\frac{dE}{dt} \simeq \frac{Z^2 e^6 n_i}{12\pi^3 \varepsilon_0^3 m_e^2 c^4 \hbar} E \ln\left(\frac{192}{Z^{\frac{1}{3}}}\right). \tag{1.14}$$

## 1.2 Hadronic interactions and production of VHE $\gamma$-rays

The radiation created by the processes presented above is dominated by the emission of low mass particles such as electrons and positrons (hence leptons) since the emitted power is inversely proportional to the square of the particle's mass. In the case of high mass particles such as hadrons, $\gamma$-rays are created indirectly, mostly as consequence of the decay of unstable particles generated by hadronic interactions, normally inelastic scattering of high energy protons with nuclei. In such interactions mostly mesons like pions ($\pi^0$, $\pi^+$ and $\pi^-$), but also kaons, nucleons ($p$ and $n$) and hyperions ($\Delta, \Lambda, \Sigma$ and $\Xi$), together with the fragments of the target nucleus are created. Extremely important for the VHE $\gamma$-ray production is the $\pi^0$ decay. The neutral pion $pp \rightarrow \pi^0$ has an extremely short lifetime of $8 \times 10^{-17}$s and decays almost instantly in $2\gamma$-rays $\pi^0 \rightarrow 2\gamma$ with same energy. As given in [Aharonian and Atoyan, 2000], the $\gamma$-ray emissivity due to decay of $\pi^0$ in the case of any broad energy distribution of CR is

$$q_\gamma(E_\gamma) = 2\int_{E_{min}}^{\infty} \frac{q_\pi(E_\pi)}{\sqrt{E_\pi^2 - m_\pi^2 c^4}} dE_\pi, \tag{1.15}$$

where $E_{min} = E_\gamma + m_\pi^2 c^4/4E_\gamma$, $m_\pi$ is the $\pi^0$ rest mass and

$$q_\pi(E_\pi) = \frac{cn_H}{K_\pi}\sigma_{pp}\left(m_p c^2 + \frac{E_\pi}{K_\pi}\right) n_p\left(m_p c^2 + \frac{E_\pi}{K_\pi}\right) \tag{1.16}$$

is the $\pi^0$ emissivity. $\sigma_{pp}(E_p)$ is the total cross-section of inelastic $pp$ collisions, $K_p$ is the mean fraction of the kinetic energy $E_{kin} = E_p m_p c^2$ transferred from the proton to the secondary $\pi^0$ per collision and $n_p(E_p)$ is the energy distribution of the protons. Even in this case the $\gamma$-ray spectrum follows the spectrum of the parent particles, the spectral index showing just small differences. At energies under 70 MeV the hadronic contribution to the $\gamma$-emission is practically zero and leptonic processes dominate. The hadronic emission dominates at high energies, the IC at very high energies (see Fig. 1.3).

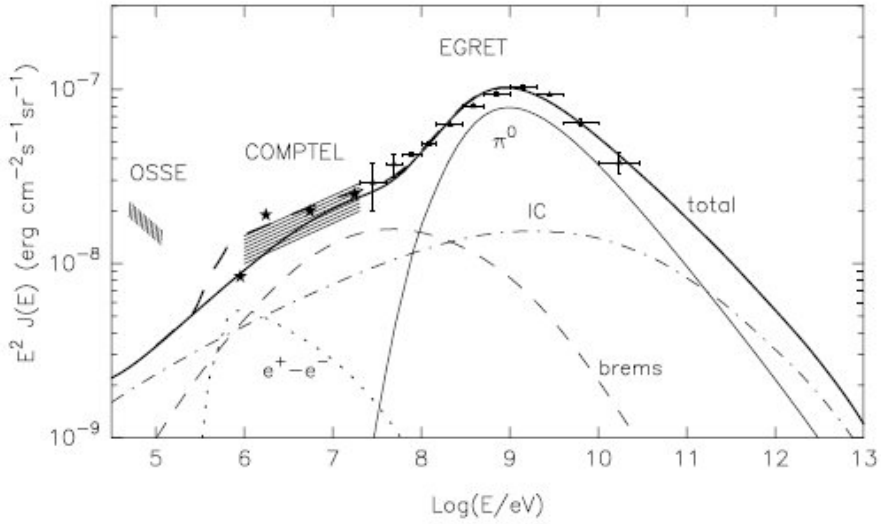


**Fig. 1.3.** Calculated fluxes of diffuse radiation produced by both electronic and nucleonic components of cosmic rays in the inner Galaxy. Contributions from $\pi_0$-decay (thin solid line), bremsstrahlung (dashed), IC (dot-dashed), and positron annihilation in flight (dotted line) to the $\gamma$-radiation mechanisms are shown. The heavy solid line shows the total flux without contribution from the positron annihilation, and the heavy dashed line takes this flux into account (from [Aharonian and Atoyan, 2000]).

## 1.3 Particle acceleration - second order Fermi mechanism

After having seen which mechanisms make possible the VHE $\gamma$-ray emission, it has to be understood how CR can be accelerated at high energies. It was Fermi who in 1949 proposed for the first time an acceleration mechanism in which particles gain energy colliding with clouds in the interstellar medium. They are reflected by randomly moving "magnetic mirrors" associated with irregularities in the Galactic magnetic field in a sequence of head-on and following collisions. In the case of relativistic particles ($v \approx c$) the average energy gain per collision is [Longair, 1994]

$$\left\langle \frac{\Delta E}{E} \right\rangle = \frac{8}{3} \left( \frac{V}{c} \right)^2 , \tag{1.17}$$

where $V$ is the velocity of the cloud. Since the energy increase goes with the square of $V/c$, this

mechanism is known as *second order* Fermi mechanism. This method leads also to a power-law energy spectrum [Longair, 1994]

$$N(E) \propto E^{-1+(\alpha\tau)^{-1}} \text{ with } \alpha = \frac{4}{3}\left(\frac{V^2}{cL}\right) \tag{1.18}$$

where $\tau$ is the characteristic time for which the particle remains in the acceleration region and $L$ is the mean free path between two clouds. However, considering collision with interstellar clouds the main source of energy leads to problems, mostly due to the fact that indeed the number of collisions per year and the effective exchanged energy are really low, since $L \sim 1pc$ and $V/c \leq 10^{-4}$, with the consequence of very little hope of gaining significant acceleration. One more efficient method is then needed.

## 1.4 Particle acceleration - first order Fermi mechanism

In the 1970s the original Fermi mechanism was revisited and adapted to strong shock waves independently by several authors (e.g. [Bell, 1978] and [Blandford and Eichler, 1987]). With simple assumptions on the mean particle energy after one collision ($E = \xi E_0$) and on the escape probability ($P$) from the acceleration region one has that [Longair, 1994]

$$\frac{dN(E)}{dE} \propto E^{-1+\left(\frac{\ln P}{\ln \xi}\right)}, \tag{1.19}$$

hence finding again a power-law. In the case of a strong shock (as can be in a supernova explosion) a flux of high energy relativistic particles is considered to be present both in front (upstream region) and behind the shock (downstream region). The shock moves at highly supersonic (but not relativistic) velocity $U \approx 10^4 km/s \gg v_s \approx 10 km/s$ ($v_s$ is the sound speed in the medium), but is hardly noticed by the particles, since their gyroradius, due to the high energy, is normally

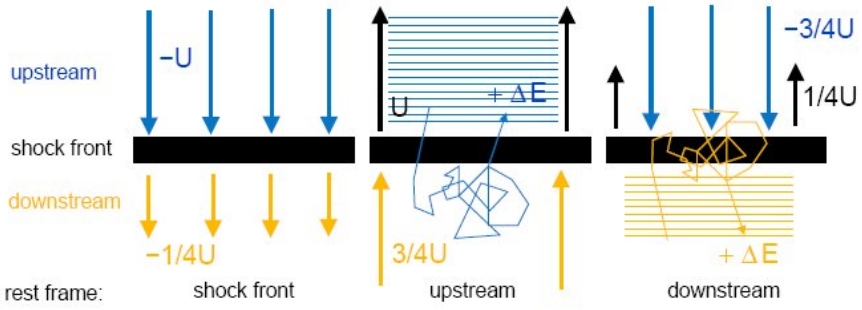


**Fig. 1.4.** Representation of *first order* Fermi mechanism. **Left**: Rest frame of the shock front. The gas in the upstream region moves towards the shock front with velocity $U$, while in the downstream region with velocity $1/4U$ (in the case of a monoatomic or fully ionized ideal gas). **Middle**: Rest frame of the upstream region. **Right**: Rest frame of the downstream region. In both cases the particles at rest encounter the gas coming from the other region with velocity $3/4U$, get scattered by the turbulences on the other side of the shock front becoming isotropic and gaining an energy $\Delta E$ (from [Funk, 2005]).

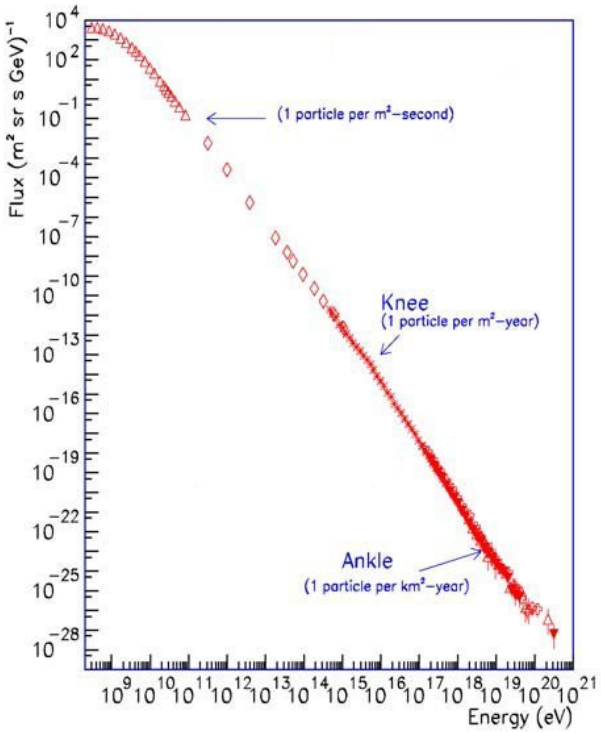


**Fig. 1.5.** The cosmic ray spectrum. A steepening at $\sim 10^{15}$TeV (*knee*) and a flattening at $\sim 10^{19}$TeV (*ankle*) are also visible. It is generally believed that CR below the *knee* have a galactic origin, while those above the *ankle* are produced outside the Milky Way.

very much larger than the shock thickness. Moreover a magnetic field with turbulences and irregularities is considered, so that the particles that cross the shock in either directions are scattered and their velocity distribution becomes isotropic with respect to the frame of reference in which the gas is at rest on either side of the shock. Observing the dynamics in turn from the rest frames in the upstream and in the downstream region one can see that the particles undergo the same process, in both cases seeing the other region moving towards the shock front with the same velocity $3/4U^2$ and in both cases gaining a little amount of energy every time they cross the shock front. This is the improvement in efficiency with respect to the classical Fermi mechanism: the process is symmetric in both directions from upstream to downstream region and vice versa, there are just head-on collision leading to an increase of energy every time the shock is crossed, no matter in which direction. Such average energy gain per cycle (i.e. particle moving from one region to the other and back) is [Longair, 1994]

$$\left\langle \frac{\Delta E}{E} \right\rangle = \frac{U}{c}. \tag{1.20}$$

In this case the energy increase goes linearly with the shock velocity, it is a first order process

[2] For a monoatomic or fully ionized gas.

and therefore the mechanism is called *first order* Fermi mechanism. From here the value of $\frac{\ln P}{\ln \xi}$ in the spectrum can be calculated, resulting [Longair, 1994]

$$\frac{\ln P}{\ln \xi} = \frac{\ln\left(1-\frac{U}{c}\right)}{\ln\left(1+\frac{U}{c}\right)} = \frac{-\frac{U}{c}}{\frac{U}{c}} = -1, \tag{1.21}$$

so that one obtains

$$\frac{dN\left(E\right)}{dE} \propto E^{-2}. \tag{1.22}$$

The value of 2 for the spectral index is not actually the real measured one for CR, though it is very close to it (∼2.7). However, the goodness of this method lies in the fact that it explains simply but with excellent physical reasons why one can find power-law energy spectra with equal index looking at different astrophysical environments. Taking into account just supernova explosions, their lifetime and the mean times for a cycle and for a particle to escape from the acceleration region, CR up to 100 TeV can be explained. At higher energies more powerful accelerators or other mechanisms or theories are needed.

## 1.5 Galactic accelerators

After having seen how the acceleration mechanism works, in the next paragraphs the objects in which such acceleration takes place will be briefly presented. Inside our galaxy the most common

**Fig. 1.6.** Type Ia supernova SN1994D in the disk galaxy NGC 4526 (from [APOD, 2009]).

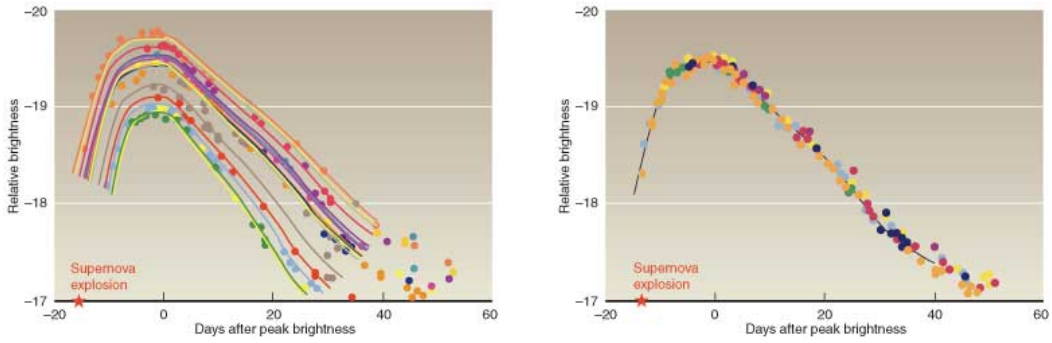


**Fig. 1.7.** (a) Supernova type Ia light curves. Brightness is plotted against time before and after peak light (Day 0). (b) Same light curves scaled. It is apparent that they all obey a general width luminosity relationship. The supernovae can thus be used as standard candles to infer the distance to their host galaxies (from [Science and technology review, 2008]).

systems thought to be CR accelerators are the remnants of supernova explosions, considered as a whole, that is not only the supernova shock fronts, but also their compact remnants like the pulsars and their pulsar wind nebulae. These have been found to be sources of VHE $\gamma$-rays.

### 1.5.1 Supernova remnants

Supernova explosions are the violent death of massive stars, during which an enormous amount of energy is released. Part of this energy is emitted as kinetic energy of the ejected material that expands in the interstellar medium (ISM) with supersonic velocity (some thousand kilometers per second), creating a shock front where particle acceleration up to $10^{15}$eV can occur. Supernova explosions are classified after the shape of their light curves and after the presence of certain emission lines like H, He, Si, Fe, C, O. Two fundamental classes can however be defined, taking into account the dynamic of the explosion: the thermonuclear disruption of a white dwarf owing to mass accretion from another star (type Ia) and the gravitational core collapse of a massive star (type II, Ib and Ic). What determines the one or the other dynamic is the initial mass of the star ($M_{initial}$) being smaller or larger than 8 solar masses ($M_{\odot}$). In the first case the star ends up its life as a white dwarf and if nothing else occurs it will cool down on time scales of $10^{10}$ years becoming eventually a black dwarf[3]. In the case of binary systems however the white dwarf can accrete matter from the companion star until the Chandrasekhar limit is reached ($M_C \sim 1.44 M_{\odot}$). At that point the electron degeneracy pressure that sustains the white dwarf is overcome by the additional gravitational pressure and the resultant compression starts the next fusion stage. The released kinetic energy ($\sim 10^{51}$erg) leads to the destruction of the white dwarf in a type Ia supernova, with an ejection of about $1 M_{\odot}$. Since they appear in all types of galaxies and the initial parameters are very narrow, the development of this kind of supernova show only little variations and this makes them useful as standard candles, e.g. as distance markers in cosmology (Fig. 1.7).

[3] No black dwarf has been detected so far.

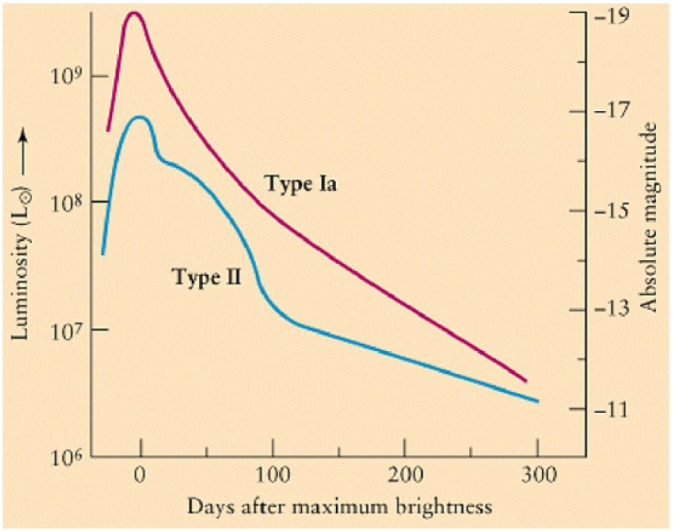


**Fig. 1.8.** Comparison between the light curves of a type Ia and a type II supernova.

On the other hand, in the case of more massive stars the electron degeneracy pressure is not enough to sustain a white dwarf, so that the contraction keeps going on and nuclear fusion continues up to iron, accreting mass on the core with a rate of $\sim 1 M_\odot/s$. Due to the high density and temperature, inverse $\beta$-decay ($e^- + N(Z,A) \rightarrow N(Z-1,A) + \nu_e$) and photo-disintegration ($\gamma + \ ^{56}\mathrm{Fe} \rightarrow 13\ ^4\mathrm{He} + 4n$, $\gamma + \ ^4\mathrm{He} \rightarrow 2p + 2n$) occur, resulting in loss of energy and of electron pressure that speed up the gravitational collapse even further. This continues until the density becomes so high that the repulsive component of the nuclear force sets in. Neutrinos are emitted from the core at a high luminosity and deposit part of their energy into the medium surrounding the core, creating an outgoing shock front which causes the explosive ejection of the outer parts of the star (supernova type II, Ib, Ic). Core collapse supernovae show a large variability since they have a broad range of initial parameters. The ejected mass can have values up to (and even beyond) ten solar masses and the kinetic energy of the ejecta cover a range from about $10^{51}$ up to $10^{52}$ erg. Furthermore they are observed only in spiral and irregular galaxies and are concentrated in the spiral arms.

In both mass accretion and core collapse supernovae the kinetic energy is only about 1% of the total emitted energy ($\sim 3 \cdot 10^{53}$erg), the rest is carried away mostly by neutrinos. The optical shape of their lightcurves differs, both having a rapid increase and an exponential decrease due to the decay of unstable isotopes, but in the case of core collapse supernovae the maximum is less bright and broader ($L \sim 10^8 L_\odot$, lasting for about 100 days) with respect to mass accretion supernovae ($L$ up to $\sim 5 \cdot 10^9 L_\odot$) and also the decrease is more complex. In both cases their optical luminosity at maximum is comparable to that of their whole host galaxy (Fig. 1.6). Even though supernova explosions occur with a rate of about 2 per century in a Milky Way type of galaxy, they are believed to be the most likely source for CR up to $10^{15}$eV. A 10% efficiency in accelerating particles is indeed sufficient to explain the CR flux and theoretical models predict efficiencies above this value.

### 1.5.2 Pulsar and Pulsar Wind Nebulae

In the case of a supernova type II a neutron star with high angular velocity and strong magnetic field can be left behind. Such properties are due to the conservation of angular momentum and magnetic flux. Since the explosion can be asymmetric, the neutron star can also acquire a random space velocity, a kick of typical magnitude 400-500 km/s ([Gaensler and Slane, 2006]). If the rotation and the magnetic field axes are misaligned, the highly energetic radiation emitted near the magnetic poles will reach a potential observer as a periodic signal. The neutron star is then called pulsar. The rotation period of a pulsar covers a range from few milliseconds up to several seconds. The magnetic field can vary from $10^8$G for millisecond pulsar up to $10^{15}$G for magnetars. Typical values lie however in the range between $1 \cdot 10^{12}$ and $5 \cdot 10^{13}$G. Each pulsar is characterized by a spin down luminosity, defined as the rate at which the rotational kinetic energy is dissipated, mostly because of magnetic dipole radiation [Gaensler and Slane, 2006]:

$$\dot{E} = -\frac{dE_{rot}}{dt} = 4\pi^2 I \frac{\dot{P}}{P^3}, \tag{1.23}$$

where $I$ is the momentum of inertia of the neutron star and $P$ its period. Measured spin down luminosities range between $\sim 3 \cdot 10^{28}$erg/s and $\sim 5 \cdot 10^{38}$erg/s. Only pulsars with $\dot{E} \geq 4 \cdot 10^{36}$erg/s are known to power bright pulsar wind nebulae. A characteristic age $\tau_c$ of the pulsar can be estimated under the assumption of pure magnetic dipole braking and of an initial period $P_0$ much smaller than the current period:

$$\tau_c \equiv \frac{P}{2\dot{P}} \tag{1.24}$$

$\tau_c$ actually does often overestimate the real age, indicating that $P_0$ is not much smaller than $P$.

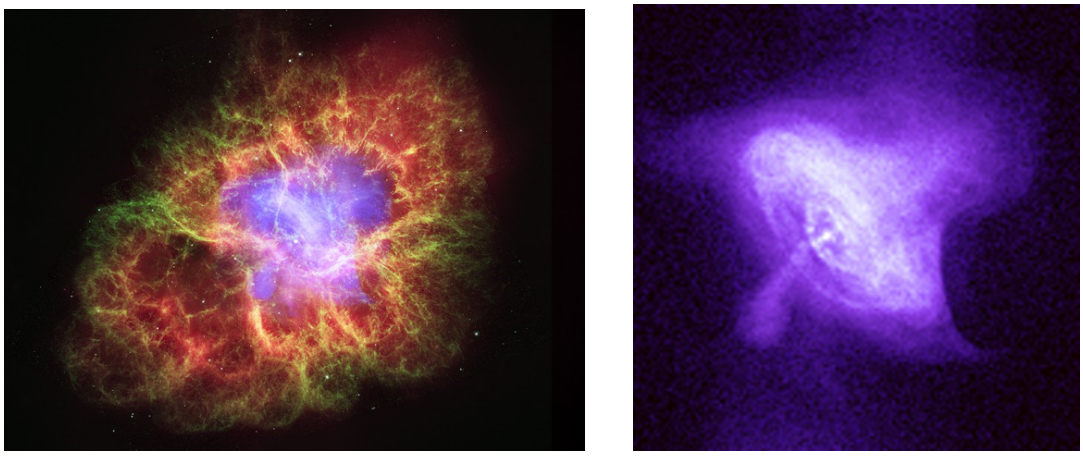

(a) (b)

**Fig. 1.9.** The Crab Nebula. (a) False color image combining Xray data from Chandra (purple), optical from Hubble (green) and infrared from Spitzer (red). (b) X-ray image from the Chandra. The pulsar, the torus and the jets are clearly visible. Taken from [APOD, 2009]

A pulsar wind nebula[4] (PWN) is a complex structure generated and powered by the pulsar's powerful winds, made up by electromagnetic energy and highly relativistic particles. These winds are generated in the pulsar's magnetosphere, that co-rotates with the pulsar itself. They travel outwards with highly relativistic velocity ($\gamma \sim 10^4 - 10^6$) until they are decelerated at the smaller expanding velocity of the ambient material. At that point a termination shock is formed and the wind is particle-dominated and not isotropic, but concentrated into an equatorial belt. Due to the presence of the shock the wind's particles are then thermalized and re-accelerated and a torus (visible in X-rays from synchrotron emission) perpendicular to the rotation axis is formed. Jets are also present, created by shocked plasma collimated by the magnetic field. An expanding bubble is formed far beyond the torus (Fig. 1.9). The PWN expands supersonically into the SNR ejecta producing therefore an other termination shock. This is the first stage of a PWN after a SN explosion. After few thousand years the expanding bubble encounters the inverse shock of the SNR (caused by the ejecta falling inwards) and is crushed by it. An oscillation of the PWN size takes place ([Gaensler and Slane, 2006]), leading to a mixing of thermal and non-thermal material. It can happen that the inverse shock does not arrive simultaneously at the PWN boundary, causing strong asymmetries in the PWN shape and even an offset from the pulsar position. This can occur if the pulsar has a high kick velocity and offsets the PWN from the SNR center before it meets the inverse shock, or if there is a density gradient in the ejecta so that the inverse shock is created at different times. Since the ejecta have now been heated by the reverse shock, the expansion of the PWN becomes subsonic. The original PWN is constantly inflated by the pulsar, as long as it is not far offset from the current pulsar position. In this case it is not powered anymore and becomes a relic PWN. If the pulsar was born with a high kick velocity, at a certain point it will approach the edge of (and possibly even leave) the SNR, driving a cometary bow shock until its power output becomes so low that the PWN can not be powered anymore (Fig. 1.10).

The VHE emission region of a PWN is often largely extended and wider than its synchrotron counterpart visible in X-rays. This is due to the radial decrease of the magnetic field that limits the size of the synchrotron emission region. A synchrotron X-ray counterpart can even not be detected if the magnetic field is low enough, and the pulsar itself can be "invisible" if the neutron star's cooling time and the non-thermal radiation time scale are exceeded, avoiding hence the (non-)thermal X-ray emission. That would lead to a VHE PWN without X-ray counterpart. The center of gravity of the VHE PWN is also often offset from the current pulsar position either because of a high kick velocity of the pulsar or because of inhomogeneities in the ISM.

Different types of $\gamma$-ray emission are expected in a PWN. Within the pulsar magnetosphere, because of the curvature radiation of the ultra-relativistic electrons, a pulsed component in the GeV range with an exponential cut-off around 10 GeV is expected. Possibly also an additional TeV component due to IC scattering can be present. In the region between the pulsar and the termination shock no synchrotron emission is present because the electrons move with the magnetic field lines frozen into the wind. However there can be an IC component in the range 10 GeV - 10 TeV produced by the interaction of the high relativistic wind with the thermal photons emitted from the pulsar or with the non-thermal photons from the magnetosphere. At the termination shock front, the thermalized and re-accelerated particles emit synchrotron and IC radiation, con-

[4] It is also known as plerion.

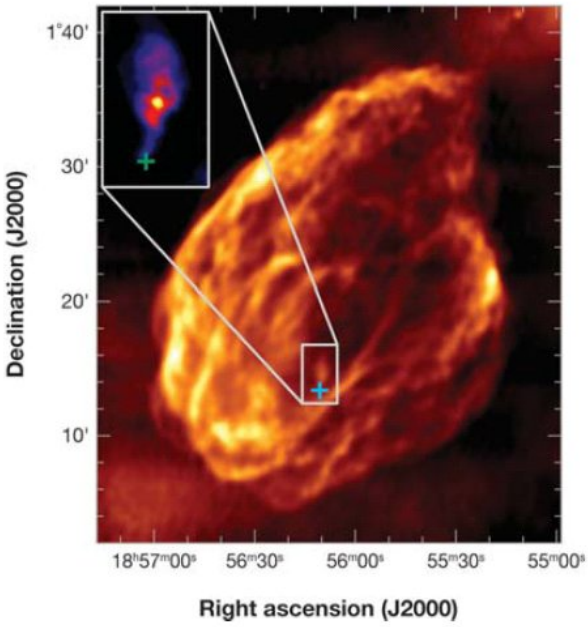


**Fig. 1.10.** The supernova remnant (SNR) W44 (G34.70.4). The main panel shows a 1.4 GHz VLA image of the SNR, while the inset shows 8.4 GHz VLA data on the region surrounding the associated young pulsar B1853+01, marked by a cross. The pulsar is nearing the edge of the SNR, and drives a small bowshock PWN (from [Gaensler and Slane, 2006]).

tributing most to the VHE $\gamma$-radiation. The maximal energy reachable by the particles is [de Jager and Djannati-Ataï, 2008]

$$E_{max} = (110\text{TeV})\,\kappa \left(\frac{\epsilon}{0.2}\right) \left(\frac{\sigma}{0.1}\frac{\dot{E}}{10^{36}\text{erg/s}}\right)^{1/2} \tag{1.25}$$

in the case of a low ambient magnetic field, or

$$E_{max} \simeq (200\text{TeV}) \left(\frac{\alpha}{\langle \sin^2\theta \rangle}\right)^{1/2} \left(\frac{B}{100\mu G}\right)^{-1/2} \tag{1.26}$$

in the case of strong magnetic fields. In Eq. 1.25 $1 < \kappa < 3$ is the magnetic compression ratio, $\epsilon < 1$ is the fractional size of the shock front radius required for the containment of the particle in the shock and $\sigma$ is the wind magnetization parameter (ratio between electromagnetic and particle energy density). In Eq. 1.26 $\alpha \leq 1$ and $\theta$ is the electron's pitch angle.

## 1.6 Air showers

Air showers are generated as VHE particle hit the atmospheric nuclei creating secondary particles through strong, electromagnetic and weak interactions. These in turn interact with other nuclei, starting a cascade that will eventually die out when the available energy becomes too low. Part

of the transferred energy is converted in kinetic energy, allowing the particles to move in the air faster than the speed of light and to emit therefore Cherenkov light. There are two kind of air showers, depending on the object that causes them and in which different processes take place: hadronic- and electromagnetic-showers. Almost all the showers are hadronic showers from cosmic rays (CR), being the proton events ∼87% of the total, $\alpha$-particles ∼12% and a small fraction of heavier nuclei. Electromagnetic showers caused by $\gamma$-rays, electrons, positrons and high energy neutrinos are just a minor fraction (∼0.2%). In electromagnetic showers the main processes are bremsstrahlung and pair production, in the hadronic ones also hadronic interactions have an important role. In case of bremsstrahlung a charged particle is decelerated and deflected in the coulomb field of a nucleus and a $\gamma$-ray photon with an energy proportional to the particle energy is emitted as a consequence of the effective acceleration. A radiation length $X_0$ is simply defined as the thickness of the medium that reduces the particle energy by a factor $e$ and has a value of 37.2 g/cm$^2$ in the air, corresponding to 300 meters at sea level. The photons generated by bremsstrahlung are emitted in a cone with an opening angle $\Theta$=1/$\gamma$=$\mu$c$^2$/E ($\mu$=particle mass). Since the energy loss by bremsstrahlung is inversely proportional to the square mass of the particle, mainly electrons and positrons take part at this process. The pair production mechanism consists in the creation of an electron-positron pair by a photon with an energy at least twice as big as the electron rest mass. A third particle is needed in this process because of momentum and energy conservation. The radiation length is 9/7 of the bremsstrahlung radiation length $X_0$, while the average opening angle is the same. In case of hadronic interactions the nuclei involved are mostly destroied and numerous subatomic particles and nuclear fragments are generated.

### 1.6.1 Electromagnetic showers

If a particle with sufficient energy interacts via electomagnetic interaction with the nuclei in the atmosphere an electromagnetic shower forms. The particles created in the shower lose their energy via pair produciton, bremsstrahlung and ionization. The number of particles first increases exponentially, then stops as the mean energy falls below a critical energy $E_C$ defined as the energy at which the energy loss due to bremsstrahlung becomes smaller than the one due to ionization ($E_C$≈81 MeV). Eventually the shower dies out. A simplified model that can easily explain the main properties of an electromagnetic air shower is the one introduced by Heitler [Heitler, 1954]. It takes into account only bremsstrahlung and pair production, sets both radiation length to $X_0$ and ignores energy losses by ionization. Moreover, the energy is always equally divided between the two created particles. A schematic representation is given in Fig. 1.11. In the case of a primary $\gamma$-ray with energy $E_0$ entering the atmosphere it generates within one radiation length an $e^-$-$e^+$ pair via pair production. In turn, after another radiation length, both electron and positron generate a photon by bremsstrahlung. After $m$ radiation lengths $X_0$ the cascade consists therefore of [Perkins, 2003]

$$N(m) = 2^m \text{ particles with energy } E(m) = E_0 \cdot 2^{-m}. \tag{1.27}$$

The maximal shower depth $m_{max}$ is given by:

$$E(m_{max}) = E_0 \cdot 2^{-m_{max}} \equiv E_C \Rightarrow m_{max} = \frac{\ln(E_0/E_C)}{\ln 2} \tag{1.28}$$

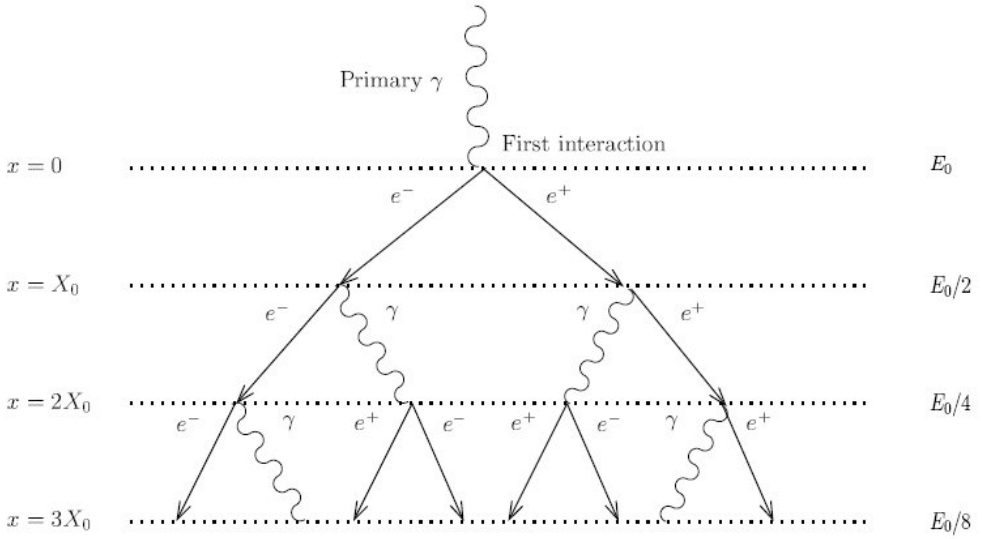


**Fig. 1.11.** The electromagnetic shower model by Heitler. Just bremsstrahlung and pair production are considered, both radiation length are set to $X_0$ and the energy is equally divided between the particles.

at which depth the shower consists of $N_{max}$ particles

$$N_{max} = 2^{m_{max}} = \frac{E_0}{E_C}. \tag{1.29}$$

From this simple model one can see how the number of particles in the shower grows exponentially until a maximum number $N_{max}$ proportional to the energy $E_0$ of the primary $\gamma$-ray is reached. The maximal depth $m_{max}$ is instead proportional to the logarithm of $E_0$. For a 1 TeV $\gamma$-ray, the typical height for the first interaction is $\sim$25 km, the maximal depth is $\sim$8 km and the complete electromagnetic shower evolves in $\sim 50\mu$s.

### 1.6.2 Hadronic showers

In the case of a hadron hitting the atmosphere, the development of the shower is more complex with respect to an electromagnetic one (Fig. 1.12). Indeed hadrons interact nearly only via strong interaction with the air nuclei producing mostly mesons like pions ($\pi^0$, $\pi^+$ and $\pi^-$), but also kaons, nucleons ($p$ and $n$) and hyperions ($\Delta, \Lambda, \Sigma$ and $\Xi$), together with the fragmets of the target nucleus. All these particles evolve then in hadronic and electromagnetic sub-showers. The neutral pions, having an extremely short lifetime of $8 \times 10^{-17}$s, undergo almost instantly an electromagnetic decay producing 2 $\gamma$-rays ($\pi^0 \rightarrow 2\gamma$) that will evolve in the previously described electromagnetic shower. Charged pions have instead a longer lifetime ($2.6 \times 10^{-8}$s) that increases the probability of new interactions with air nuclei before the decay $\pi^{\pm} \rightarrow \mu^{\pm} + \nu_{\mu}\,(\bar{\nu}_{\mu})$ takes place. In turn also muons will decay $\mu^{\pm} \rightarrow e^{\pm} + \nu_e\,(\bar{\nu}_e) + \bar{\nu}_{\mu}\,(\nu_{\mu})$. Such interactions give rise to hadronic sub-showers. Since muons do not have strong interaction, they lose their energy mainly because of ionization, therefore, if they have enough energy (>3 GeV) they can reach the ground

level (or even deep underground) without being brought to rest or decaying. Because of their penetrating property they are called the hard component of the cosmic rays.

The main differences between hadronic and electromagnetic showers are in the shower shape and in the energy distribution among the particles. Since hadrons have a larger interaction length with respect to the radiation length of the photons (85 g/cm$^2$ vs. 37.2 g/cm$^2$), they penetrate deeper into the atmosphere and have therefore a larger value of $m_{max}$. Particles participating to the strong interaction receive a higher transverse momentum with respect to those participating only to electromagnetic interaction (given by elastic multiple coulomb scattering), so that the lateral development of hadronic shower is is much larger than that of the electromagnetic ones. Furthermore, since more numerous and complex processes are involved, the hadronic showers are less regular, have larger fluctuations, and contain electromagnetic sub-showers created by neutral pion decays. At last, in the strong interaction a consistent part of the energy is lost in the creation of new particles like muons, other mesons, and secondary hadrons.

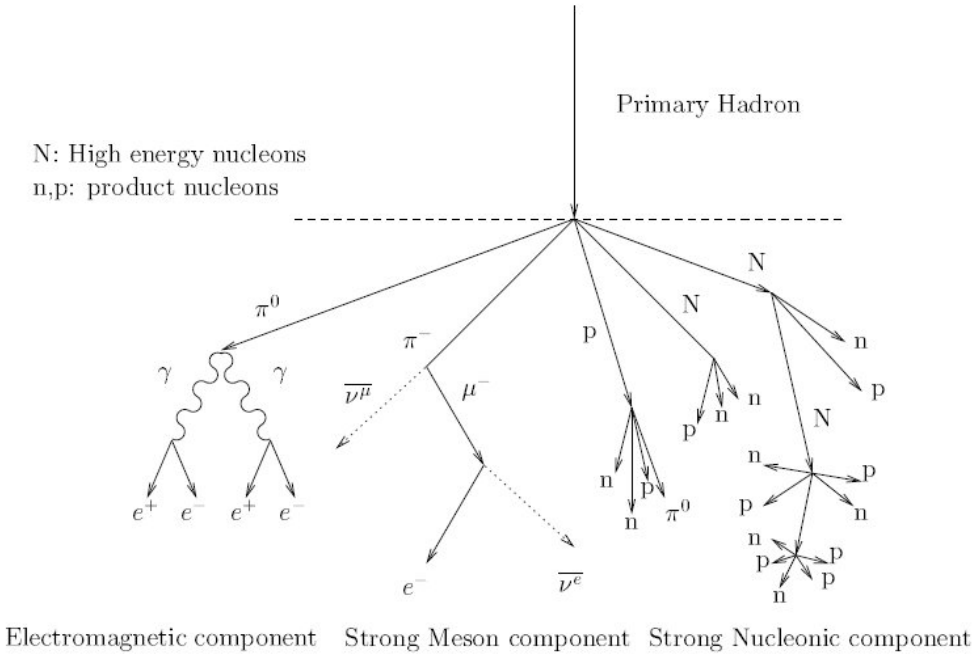


**Fig. 1.12.** Schematic representation of the different interactions occurring in an hadronic shower.

### 1.6.3 Cherenkov emission

As mentioned earlier, particles moving in the air with a speed greater than the phase velocity of light in that medium emit Cherenkov light. This forms a cone along the particle's path with a characteristic opening angle $\Theta_C$ between the Cherenkov light front (moving with velocity $c/n$) and the particle itself (moving with velocity $v$) given by [Rybicki and Lightman, 1979]:

$$\cos\Theta_C = \frac{1}{\beta \cdot n}, \tag{1.30}$$

where $n>1$ is the refraction index and $\beta = v/c$. Since $\cos\Theta_C$ has to be smaller than 1, from 1.30 it must be $\beta > 1/n$. One has therefore for the limit of ultrarelativistic particles ($\beta \simeq 1$) a maximum angle

$$\Theta_{C,max} = \cos^{-1}\left(\frac{1}{n}\right). \tag{1.31}$$

Typical values of the opening angle are $\sim$1°-2° depending on the refraction index and on the particle velocity. A minimum energy for the particle to emit Cherenkov radiation is requested:

$$E_{min} = \gamma_{min} m_0 c^2 = \frac{m_0 c^2}{\sqrt{1-n^{-2}}}. \tag{1.32}$$

Low mass particles dominate therefore the Cherenkov radiation that appears as a continuous spectrum. The loss rate per unit of path length is [Longair, 1992]

$$\frac{dE(\omega)}{dx} = \frac{\omega e^2}{4\pi\epsilon_0 c^3}\left(1 - \frac{c^2}{n^2 v^2}\right). \tag{1.33}$$

The peak of the emission is in the UV region, but, due to strong atmospheric absorption, what can really be observed is at wavelength around and bigger than 330nm. The light is also visible on the ground for just $\sim$10ns, even if the whole developement of the shower lasts about $\sim 50\mu$s. In the case of electromagnetic showers the light cone is focused in a homogeneous distribution (with a radius between 80m and 120m around the shower axis, even if some smearing due to scattering processes is present) that decreases slightly towards the axis (Fig. 1.13). In case of hadronic events, because of the intrinsic larger lateral development of the shower, the light distribution is more widely spread. Moreover, electromagnetic sub-showers are formed causing larger fluctuations in the Cherenkov emission. Secondary muons can often reach the ground with sufficient energy to emit Cherenkov radiation, hence adding an additional component to the Cherenkov light on the ground. Anyway, because of absorption processes like the absorption by the ozone and of scattering like the Mie scattering and the Rayleigh scattering, not all the Cherenkov radiation reaches the ground. Indeed, for a primary photon of 1 TeV energy, only about 100 photons/m$^2$ reach the ground.

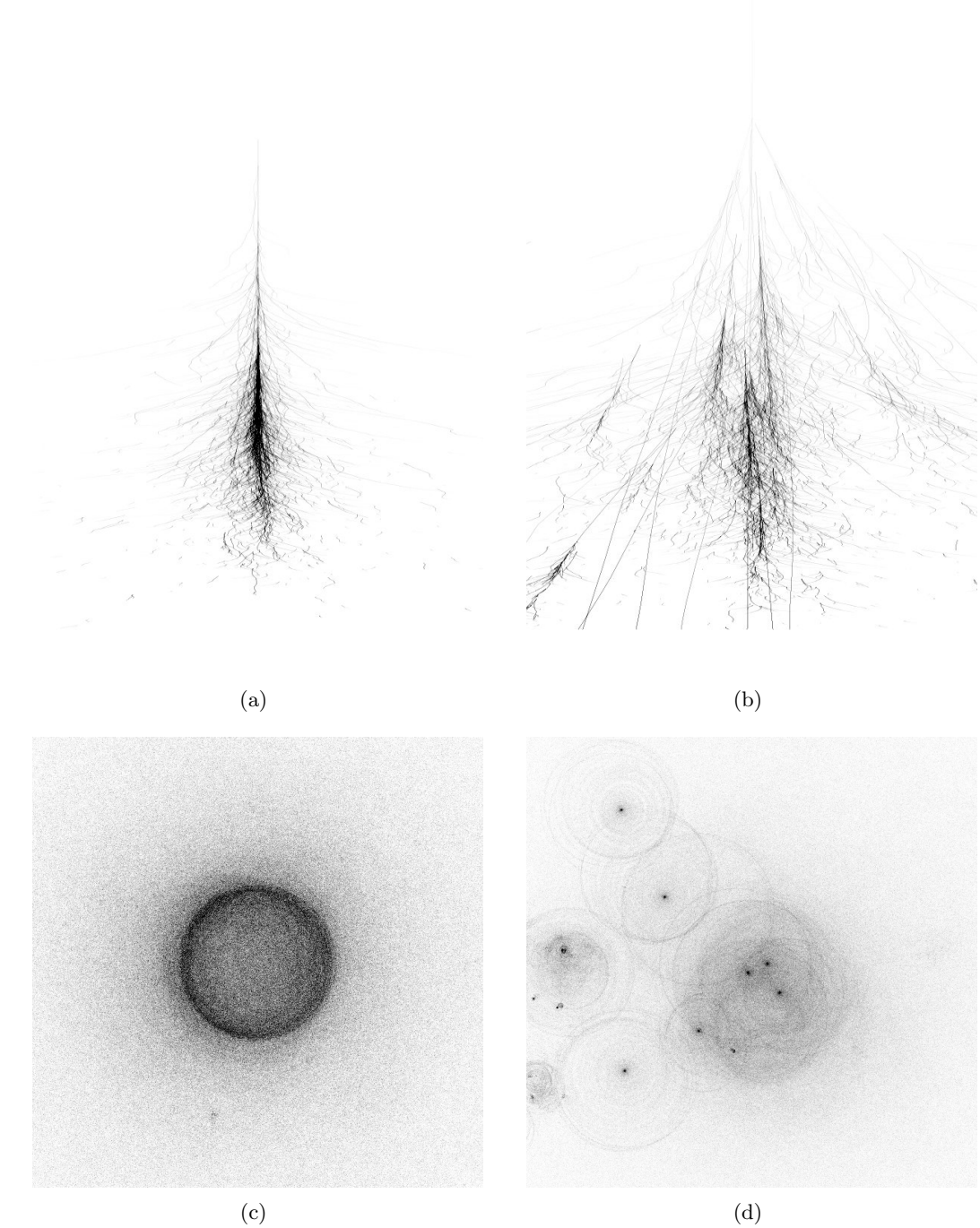

**Fig. 1.13.** Comparison of the longitudinal and lateral shower development between a 300 GeV photon (a and c) and a 1 TeV proton (b and d). The energies are different so that the amount of emitted Cherenkov light is the same in the two cases. (a) and (b) have an extension of 600m in width and 27 km in height, while (c) and (d) cover an area of 800x800m$^2$. [Bernlöhr, 2000]

# 2

# The H.E.S.S. experiment

## 2.1 Imaging Atmospheric Cherenkov Telescopes

VHE $\gamma$-rays are absorbed by interactions with the atmosphere. Satellite experiments are therefore required, but, since for energies above some tens of GeV the flux of $\gamma$-rays is so low, their detection area (some square meters) becomes too small to detect a significant number of events in a reasonable timescale. To have a large enough collection area, ground based telescopes are thus needed and a new detection method has to be used. The Imaging Atmospheric Cherenkov technique was then introduced: it records the Cherenkov light of secondary particles, generated by the interaction of the primary $\gamma$- or cosmic-ray (CR) with the particle in the atmosphere (sec. 1.6) and has, due to the large extension of the Cherenkov light cone on the ground, a much larger detection area available compared to satellite experiments. The telescopes that use this technique are called Imaging Atmospheric Cherenkov Telescopes (IACTs) and are currently the most sensitive instruments for VHE $\gamma$-ray astronomy in the energy range above 50-100 GeV.

This technique was pioneered by the Whipple collaboration which operated a single 10 m diameter IACT and achieved an energy threshold of $\sim$350 GeV. They were the first to detect a source of VHE gamma rays with the imaging technique, the Crab nebula in 1989 [Weekes et al., 1989]. Significant improvements in sensitivity were achieved in the successive generation of IACTs through the installation of an array of telescopes to allow stereoscopic imaging of air showers, like HEGRA in 1996 [Daum et al., 1997]. This approach has different advantages. Since a trigger coincidence of multiple telescopes can be required, random triggers of night-sky background light (NSB) and single-telescope triggers of local muons (local because their very narrow Cherenkov light cone triggers only a single telescope) as well as hadronic background events are strongly reduced. This is so that the telescopes can operate with reduced energy thresholds and higher sensitivity. Furthermore, multiple views of the same air shower increase the amount of information, which provides a more accurate measurement of the shower parameters and therefore allows a better reconstruction of the energy and direction of the primary ray compared to single telescopes. The stereoscopic approach was then adopted in all third generation instruments: H.E.S.S. [Hinton, 2004], Veritas [Weekes et al., 2002], Cangaroo-III [Kubo et al., 2004], MAGIC [Lorenz, 2004]. Compared to the previous generation instruments, the energy threshold was significantly lowered towards 100 GeV or less through the use of larger mirror areas.

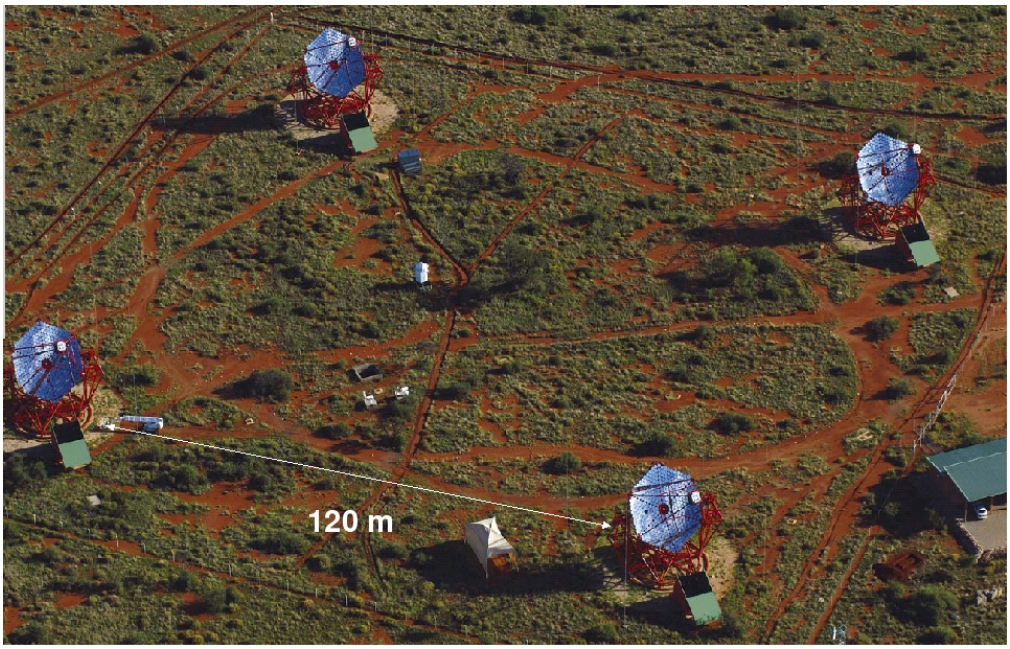


**Fig. 2.1.** The H.E.S.S. telescope array.

## 2.2 The H.E.S.S. telescope system

The H.E.S.S. system is an array of four IACTs, situated in the Khomas Highland in Namibia, 1800 m above the sea level. The acronym stands for High Energy Stereoscopic System and is a tribute to Victor Hess, who received the Nobel Prize in Physics in 1936 for his discovery of cosmic radiation in 1912. The first of the four telescopes has been operational since summer 2002 and the last one was completed in December 2003. The whole array has been functional since January 2004. The HESS system is characterized by a low energy threshold (∼100 GeV at zenith) and a 1% Crab flux sensitivity resulting from a good angular resolution and background rejection provided by the stereoscopic technique.

### 2.2.1 Site location

The location in the Khomas Highland ( 23° 16' 18" south, 16° 30' 00" east) was chosen for its close vicinity to the Gamsberg area, which is known for its excellent condition for astronomical observation [Wiedner, 1998], and for its position in the southern hemisphere. Indeed, about 57% and 64% of the ∼1700 dark moonless hours have respectively no clouds or a cloud coverage less than 25% above an altitude of 30° and 94% have a relative humidity under 90%. The southern location is important since one of the main scopes of H.E.S.S. is the quest for possible TeV galactic sources and the central part of the Galactic Plane culminates at zenith during autumn and winter, when there are the driest and most stable atmospheric conditions and the nights are longest.

### 2.2.2 Telescope structure

The four telescopes are identical and arranged in a square of 120 m side length, with the diagonals aligned in north-south and west-east direction. The distance was chosen to satisfy two main needs: to have a large collection area and a large base length for good stereoscopic view and to require that at least two telescope are able to observe the same air shower. Each telescope has a dish of 13 m diameter, mounted on a 13.6 m circular rail that permits movements in the azimuth direction. In both azimuth and elevation, the telescope is driven by friction drives that can reach an angular velocity of 100°/min, acting on 15.0 m diameter drive rails. The position is sensed by shaft encoders with a digital step size of 10" and a mechanical accuracy in tracking astronomical objects better than 3". However, due to systematic uncertainties induced by misalignments and deformation of the telescope structure, the precision for locating gamma-ray sources is about 30".

**Fig. 2.2.** The first operational H.E.S.S. telescope (from [HESS website, 2009]).

### 2.2.3 Mirrors

Each single telescope ([Bernlöhr et al., 2003] and [Cornils et al., 2003]) is constituted of a segmented reflector of diameter $d$=13 m and focal length $f$=15 m ($f/d$=1.2), composed of 380 round mirror facets of a 60 cm diameter arranged with Davies-Cotton optics ([Davies and Cotton, 1957]), for a total reflecting area of about 107 $m^2$. In such optics, all the facets have the same focal length (that is also the focal length of the whole telescope) and are arranged on a sphere of radius $f$. It also provides good off-axis imaging, which is important for having uniform response over the large field of view, which is required for observations of extended sources. The mirror

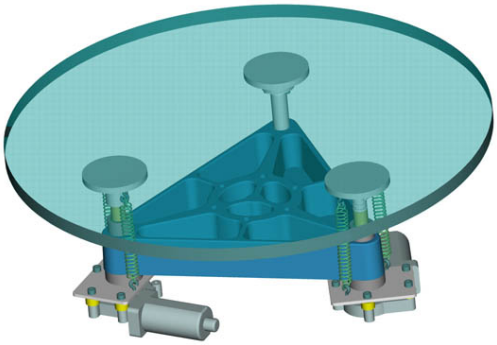

**Fig. 2.3.** Drawing of a mirror with its anchorage system (from [HESS website, 2009]).

facets are made with quartz-coated aluminized ground glass and have an average reflectivity of 80% for wavelengths above 330nm. To permit the anchorage at the dish structure and at the same time the remote position adjustment, the mirrors are attached at the dish in three points: one fixed and two mobile with motor-driven actuators (Fig. 2.3). The alignment is performed in the following way (Fig. 2.4): with a CCD camera positioned at the center of the dish, the image of a bright star is photographed on the closed camera lid (Fig. 2.4). Then each single facet is moved in both axes until the star spot is centered in the main focus. As all the facets are aligned, the star image is combined into a single spot at the center of the telescope camera.

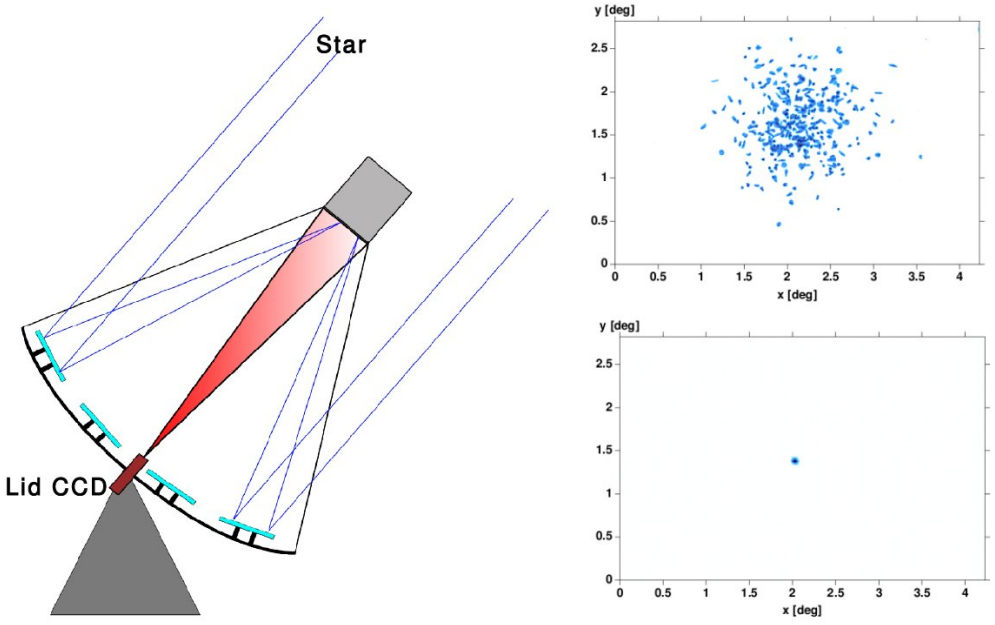


**Fig. 2.4.** Mirror alignment technique. Left: a star is observed by a CCD camera positioned at the center of the dish, viewing the closed lid of the PMT camera which acts as a screen. Upper right: star image before alignment. Lower right: star image after alignment. [Cornils et al., 2003]

The optical point spread function (PSF, defined by the radius of a circle enclosing 80% of the spot intensity, $r_{80}$) of the resulting image is well contained within the camera pixel size of 2.8 mrad and has a value of 0.25 mrad on-axis, well within its specifications. The optical PSF depends on the offset in the camera (due to spherical aberrations of the reflector) and on the elevation of the telescope (due to deformations of the dish structure), but is for all practical observations within the pixel size.

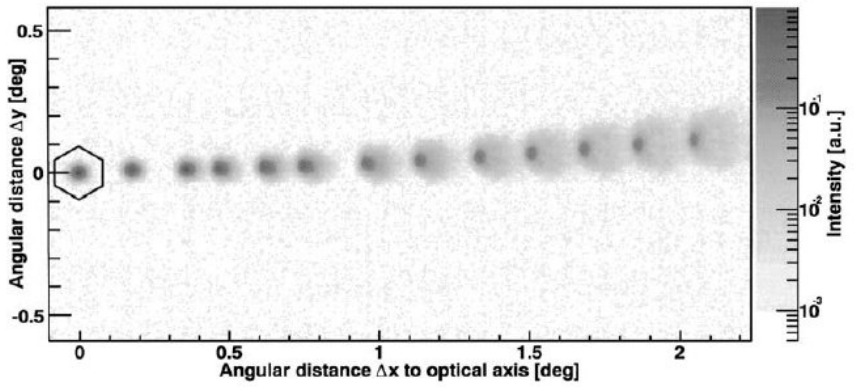


**Fig. 2.5.** Star images viewed at different offsets. The pixel size is is also indicated.[Cornils et al., 2003]

### 2.2.4 Camera

The HESS cameras are positioned in the focal plane of the reflector dishes and consist of an hexagonal array of 960 photomultiplier tubes (PMT or pixel) organized into drawers of 16 PMTs. Each pixel has an angular size of 0.16° (that is small enough to resolve image details) for a total field of view of the camera of about 5° of diameter (that allows observation of extended sources). The choice of PMTs above other alternatives is due to their quick response, needed due to the fact that Cherenkov flashes from air showers last only for a few ns. They are currently the most appropriate light sensors for IACT cameras even if their quantum efficiency is about 25%, with a maximum of 30%.

The trigger and readout electronics as well as the high voltage supply are contained inside the 1.4 m diameter camera body. Since the PMTs have circular shape, to reduce the insensitive area of the camera ($\leq 5\%$) hexagonal Winston cones [Welford and Winston, 1989] are used to funnel the light into the PMTs. They are also useful to limit the solid angle viewed by the PMT and to reduce the noise due to stray light from the ground, from the reflector, or even from the sky (if observed at low elevations).

### 2.2.5 Trigger

The signal pulse from the PMT is fed into three different channels: one into the trigger channel of the camera and two into the acquisition system with different gains [Funk et al., 2004]. By using a high gain and a low gain channel, the linear response of the PMT is increased to a dynamic

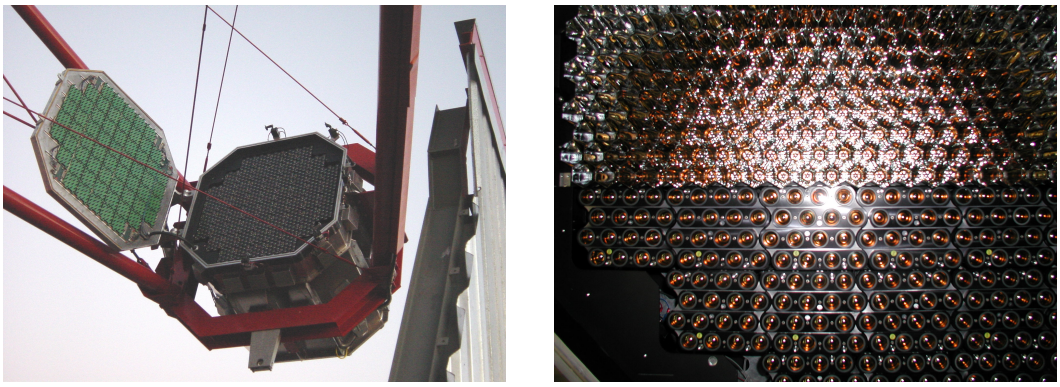

(a) (b)

**Fig. 2.6.** Left: the camera mounted on a telescope with open lid. Right: view on the photomultipliers and Winston cones (from [HESS website, 2009]).

range of up to 2000 photoelectrons (p.e.). This allows to resolve single photoelectrons from low energy showers without suffering from saturation at high Cherenkov photon densities originating from high energy showers.

The trigger system of H.E.S.S. is designed to make optimum use of the stereoscopic approach and is divided in two levels. In the first one, the local trigger for each telescope is done; in the second one a multi-telescope coincidence (at least 2 telescopes) is required by the central trigger system (CTS). In the local trigger, the camera is divided into 64 overlapping sectors with a programmable trigger requirement. A trigger occurs if the signals in $M$ pixels within a sector (sector threshold) exceed a threshold of $N$ photoelectrons (pixel threshold). A typical time-window for the multiplicity trigger is 1.3 ns. Upon receiving a camera trigger, the signal is stored in 128 ns deep analog memories from each PMT, sampled at 1 GHz and is integrated within 16 ns. Once a camera has formed a trigger, a signal is sent via optical fiber to the CTS, for the multiple-telescope coincidence requirement. This requirement leads to a significant reduction in the rate of background events, since hadronic showers have a more inhomogeneous light pool in comparison to the $\gamma$-ray events and therefore the coincidence is more hardly fulfilled. Also single muons from CR or hadronic showers are almost completely rejected by a telescope multiplicity requirement. All this gives the opportunity to reduce the camera trigger thresholds and thus lower the energy threshold of the instrument by a factor 2 compared to single telescope operation. This kind of selection already at the hardware level has the additional advantage of sensibly reducing the network, the disc space and the CPU time requirements.

### 2.2.6 Telescope pointing

Since the typical emission height of Cherenkov photons is at a depth of $\sim$10 km, the most effective observation strategy consists in slightly tilting the telescopes towards each other, so that they are looking at the same point in the sky at the height of maximum shower development. For the H.E.S.S. array, the angle that maximizes the overlap of the telescope field-of-views is around 0.7°. Maximizing the overlap results in $\gamma$-ray images that lie closer to the center of the cameras and increases the average number of usable images in the analysis. This improves the angular

resolution and hence increases the sensitivity. This "convergent" pointing is possible only at the expense of a reduced field of view, therefore it is not regularly performed.

## 2.3 Data collection

IACT telescopes generally make observations only during moonless nights, since they need astronomical darkness to be able to detect the very faint flashes of Cherenkov light. In the case of H.E.S.S., the available time is sub-divided into observations (runs) of typically 28 minutes in duration, during which a given astrophysical target or position in the sky is tracked and the data are continuously taken and stored to disk. Ideally, all other configuration parameters of the telescope system are kept constant during a run. The original and simplest observation strategy used for single telescope instruments with relatively small field of view such as the Whipple observatory [Weekes et al., 1989], was the ON/OFF observation mode. This method consists of alternated runs first on the actual target (ON-run) and then on an empty part of the sky (OFF-run) that is offset by 30 minutes in Right Ascension, but at equal zenith angle, to keep the conditions for the two runs as constant as possible. The OFF-runs can then be used to derive a background estimation for the ON-runs. The main disadvantage of this method is the need for spending half of the available observation time off-source. Since modern IACTs are built with a larger homogeneous field of view, the more appropriate wobble-mode observation method was introduced. Here the targeted source is kept in the field of view all the time, but slightly offset (0.5° to 1.0°) from the actual observation position, allowing the simultaneous taking of ON- and OFF-data. The offset is then normally alternated in four different directions in consecutive runs (i.e. at fixed Right Ascension changing the Declination or vice versa) so that the On-region is in the middle of the total field of view. The advantage of the wobble-mode is the elimination of off-source observations (and the consequent doubling of on-source time) since the background can be estimated from the same field of view as the on-data and the fact that the off-data are taken under the exact same conditions.

The Cherenkov radiation is collected by the large mirrors and reflected onto a sensitive camera. The resulting image on the camera plane is a two-dimensional projection of the shower. The mapping rule for a point $(x,y,z)$ in the atmosphere is:

$$\begin{pmatrix} u \\ v \end{pmatrix} = -\frac{f}{z} \begin{pmatrix} x \\ y \end{pmatrix}, \tag{2.1}$$

where $(u,v)$ are the resulting camera coordinates and $f$ is the focal length of the mirrors. Figure 2.7(a) illustrates for a simplified shower model the image of the shower axis in the focal plane (the "image axis"). The light emitted from the shower axis in infinite height would be mapped onto a point $(-\theta_x,-\theta_y)$ in the focal plane that indicates the inclination of the shower axis with respect to the optical axis of the telescope. In figure 2.7(b), one can see a sketch explaining the shape of the light distribution in the camera. The length of the shower image is given by the angle $\Delta\phi=\phi_2-\phi_1$ under which the shower is observed, its position by the distance $R$ between telescope and shower axis and the width by the showers lateral extent. Furthermore, the farther away a shower is from the telescope, the more the image will be elongated and near the border of the camera. The camera image of the shower is sketched in Fig. 2.8. For the narrow $\gamma$-ray induced showers, the

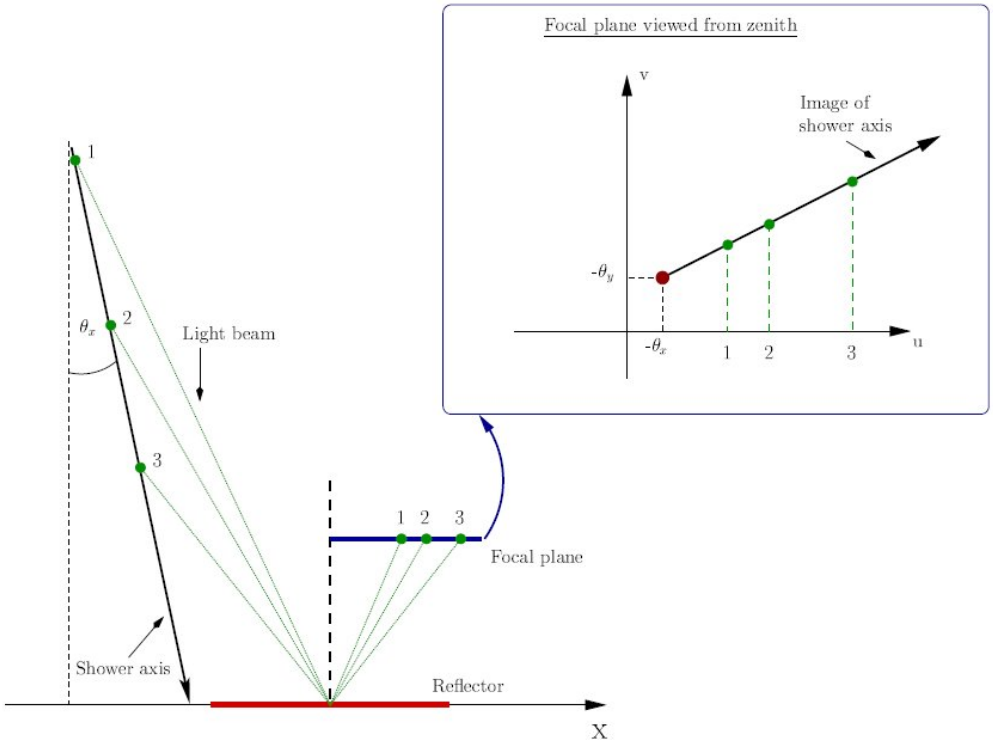


(a)

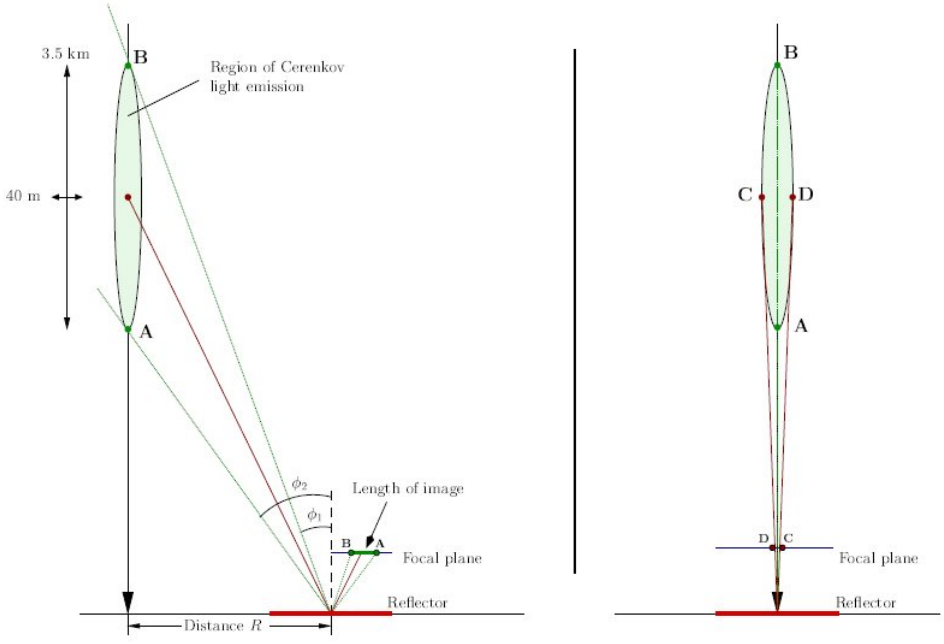


(b)

**Fig. 2.7.** (a) Mapping of the shower axis into the focal plane. (b) Basic dependencies between showers and camera images. Left: view of the shower-axis - telescope plane. Image's length and position are determined by $\Delta\phi$ and $R$. Right: view of the plane perpendicular to the previous one. (from [Berge, 2006])

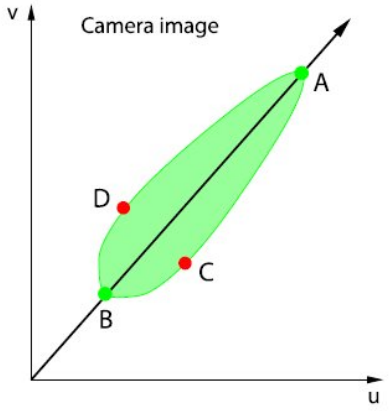


**Fig. 2.8.** Sketch of the camera image. The image shape is asymmetric due to the non-linear mapping of eq. 2.1 (from [Berge, 2006]).

images width is usually much smaller than its length, such that the image is roughly elliptical in shape. For most hadron-induced showers, the lateral spread is normally larger and they can therefore be distinguished from the $\gamma$-ray induced ones by the larger width of their images. The major axis of the image points on one side towards the direction of the primary $\gamma$-ray, and on the other side towards the shower impact point on the ground. Even though both parameters can be determined from a single shower image, the stereoscopic approach greatly improves the angular resolution, as well as the hadron rejection, since the inconsistency between reconstructed shower directions can be utilized. The energy of the primary particle can be estimated from the intensity of the shower image and from the distance between the telescope and the shower impact point on the ground.

## 2.4 Event reconstruction

Once the shower image has been recorded by the camera, the event must be reconstructed in its characteristics like type, energy and direction. The first step is the image cleaning, i.e. noisy pixels with intensities unrelated to the Cherenkov image, and therefore likely to be caused by photomultiplier noise or by NSB, are removed. For this operation, high and low thresholds are defined ($T_{high}$ and $T_{low}$), typically of 10 and 5 p.e. . The only pixels kept in the image are the ones with a p.e. content bigger than one threshold and that have a neighboring pixel with a p.e. content bigger than the other threshold. In addition, an intensity of more than $3\sigma$ of the pedestal RMS from the rest of the observation run is requested to avoid pixel suffering from bright star light (NSB threshold). All other pixel are discarded (Fig. 2.9).

As mentioned above, the shape of the image is roughly elliptical and as such it can be parametrized. The parametrization of the clean image is normally performed using the Hillas parameters [Hillas, 1985] (see Fig. 2.10(a)) which can be written in terms of moments of the light intensity distribution. The first moments of the two-dimensional intensity distribution have the mathematical form of a center of gravity ($COG$) and give the image's position, while the matrix of second moments can be interpreted as an ellipse around the $COG$. Its major and minor axis

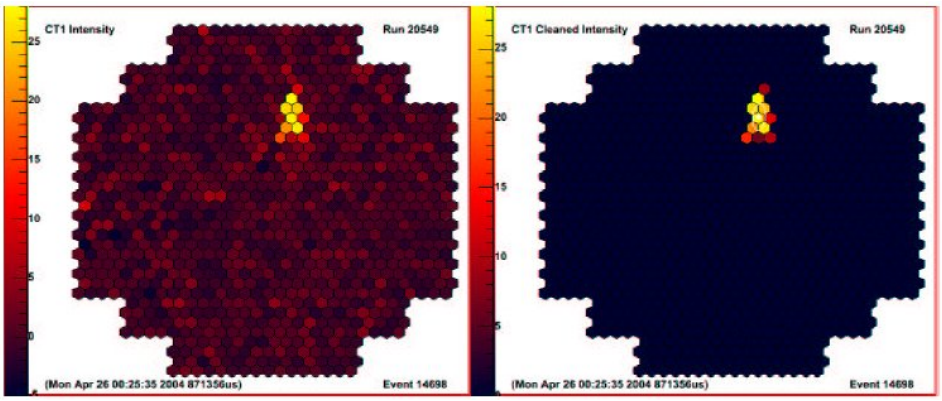


**Fig. 2.9.** Camera image before (left) and after (right) cleaning (from [Funk, 2005]).

(*length* and *width*) come from the diagonalization of the matrix as square root of the eigenvalues. The orientation angle of the ellipse ($\theta$) is given by the angle of the principal-axis-transformation. Furthermore, the shower images are characterized by their amplitudes in p.e. (*size*).

The use of the stereoscopic technique significantly improves the ability to reconstruct these properties, since the shower can be recorded under different viewing angles (Fig. 2.10(b)). The origin of the shower is located on the major axis of the ellipse, therefore, by intersecting the major axis from different cameras, one can determine precisely the direction and the impact point on the ground (the core). In the case of $N$ telescopes one has $N(N\text{-}1)/2$ intersections that are averaged after being weighted. To each intersection $i$ a weight

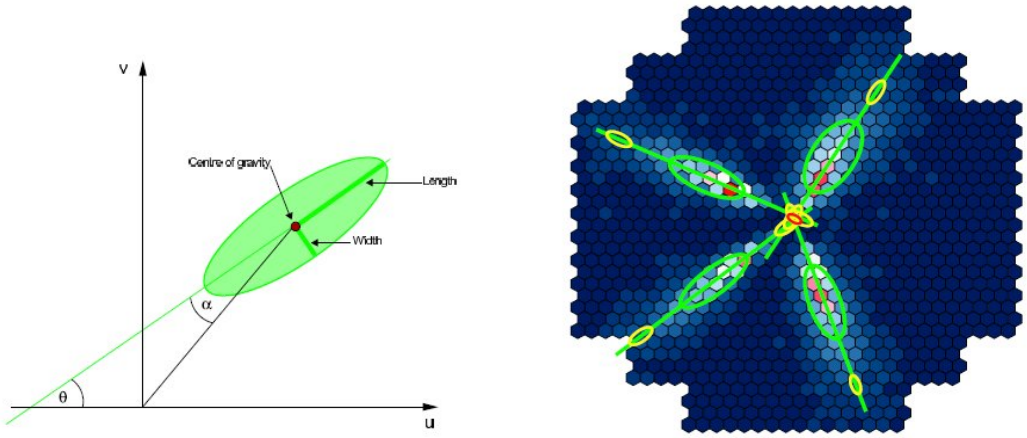


(a) (b)

**Fig. 2.10.** (a) Schematic representation of the Hillas parameters. (b) Superimposition of the images of four telescopes looking at a simulated 7 TeV $\gamma$-ray shower. Hillas ellipses are overlaid. The yellow ellipses are the estimated source regions. Their intersection gives the optimum source direction (red error ellipse) (from [Berge, 2006]).

$$W_i = \frac{sin\left(\varphi_1 - \varphi_2\right)}{\left(\frac{1}{s_1} + \frac{1}{s_2}\right)\left(\frac{w_1}{l_1} + \frac{w_2}{l_2}\right)} \tag{2.2}$$

is assigned, where $s$, $l$, and $w$ are respectively the *size*, *length* and *width* of the image. The weight takes into account that images with large stereo angle (i.e. bigger angle between images major axes) provide the most precise direction determination and that bright and elongated ($w/l$) images provide well defined shower characterization. The same mechanism can be applied to derive the position of the shower core. Typical values for the angular resolution are in the order of 0.1° and 10 m for the core location for showers which impact within 200 m from the center of the array.

Contrary to the direction estimation, the energy of the event can not be calculated directly from the image parameters, but, assuming that all particles are $\gamma$-rays, has to be determined from lookup tables generated from Monte-Carlo simulations (MC). Such simulations make use of parameters like *size*, impact parameter (i.e. the distance of the shower core from the telescope) and zenith and offset angles of observation for the telescope system

$$\langle E \rangle_{MC} = \langle E \rangle_{MC} \left(size, zenith, distance\right). \tag{2.3}$$

As the density of Cherenkov light at a fixed distance from the shower axis is approximately proportional to the primary energy, a precise reconstruction of the impact distance is important, because it determines how many photons from the shower arrive at the telescopes and therefore the energy. The $\gamma$-like event energy is then calculated using the mean of the energies determined independently for each telescope, with a typical resolution

$$\frac{\Delta E}{E} = \frac{E_{reco} - E_{MC}}{E_{MC}} \approx 15\%. \tag{2.4}$$

MC lookup tables have to be simulated for each single telescope because each telescope has a different optical efficiency due to different times of installation (and hence to different levels of degradation). As one can expect, the energy reconstruction gets better with increasing energy, since on average more light is collected by each camera and this leads to smaller statistical fluctuations in the image size. Furthermore, the intrinsic shower fluctuations also decrease with increasing energy. The energy reconstruction is also affected by other uncertainties due to systematic effects like the propagation of the Cherenkov light in the atmosphere, the optical response of the instrument and the camera response.

## 2.5 Monte-Carlo simulations

As said, for the energy reconstruction, Monte-Carlo simulations are needed. These are performed in two steps: first simulating a complete air-shower with CORSIKA (COsmic Ray SImulations for KAscade [Heck et al., 1998]) and then the response of the detector with sim_hessarray [Bernlöhr, 2002]. CORSIKA studies the evolution of air showers initiated by photons, protons, nuclei or other particles in the atmosphere, including the formation of Cherenkov light. It takes into account environmental parameters such as atmospheric absorption and geomagnetic field strength and

can be used with various particle interaction models. The sim_hessarray package simulates the response of an array of H.E.S.S. telescopes to Cherenkov light of air showers with a very high level of detail. The simulation takes into account the reflector layout and its orientation with respect to the shower, the shadow of the camera support structure, the mirror reflectivity, the transmission of the Winston cones, the optical point spread function (PSF) as well as the quantum efficiency of the PMTs and the pulse shapes of the PMT signals. Moreover, the decrease in optical efficiency of the telescopes can be taken into account.

$\gamma$-ray induced air-showers are then simulated between 20 GeV and 100 TeV, assuming the primary $\gamma$-ray spectrum to follow a power law $dN/dE \propto E^{-2}$. Each simulation is performed for 13 different zenith angles of observation (0°, 20°, 30°, 40°, 45°, 50°, 55°, 60°, 63°, 65°, 67°, 69°, and 70°) and for each zenith angle six different offset values (angular distance between source and pointing position) are taken into account (0°, 0.5°, 1°, 1.5°, 2°, 2.5°). Since the particles created in a $\gamma$-ray induced air-shower are mainly positron and electrons, the influence of the terrestrial magnetic field is important in the development of the shower and is taken into account using two different azimuth angles (0° and 180°). The need for simulations at different zenith angles derives from the fact that at large angles, air-showers are observed through a much greater atmospheric column depth. In this case, Cherenkov photons suffer more from scattering and absorption and have a larger (and dimmer) footprint on the ground, with a consequent reduction of the photon density in the light pool. This leads to an increase in the effective energy threshold of the system. However, the larger image on the ground results in a larger effective collection area and in an increased telescope multiplicity.

## 2.6 Gamma - Hadron separation

Almost all events detected by a stereoscopic system like H.E.S.S. have a hadronic cosmic ray (CR) nature and have therefore to be rejected as background. Even for bright sources the $\frac{\gamma}{CR}$ signal rate is $\sim 10^{-3}$. A first reduction of such background events is done after the cleaning through cuts on the image parameters. A standard analysis takes into account the *size*, the *COG*, the *width*, the *length* and, as already said, the telescope multiplicity (each event must trigger at least 2 telescopes and pass the successive cuts for each telescope). There are two different kinds of *size*-cuts, requiring that the image amplitude is above 80 p.e. (*standard*-cuts) or 200 p.e. (*hard*-cuts), at the expense of an increasing energy threshold. To avoid truncated images, it is required that the *COG* is inside a circle of typically 2° from the camera center (*nominal-distance*-cut). As mentioned before in par. 1.6.2 the CR induced showers are less regular and on average wider with respect to the $\gamma$ ones. Using a mean reduced scaled width (MRSW) and length (MRSL) (*shape*-cuts), one can therefore exploit this property to separate the $\gamma$-ray signal from the hadronic background. The MRSW and MRSL parameters are defined as the mean of the difference in standard deviations for each telescope of the width (length) observed in the image from that which is expected from $\gamma$-ray simulations based on image amplitude, reconstructed impact parameter, zenith angle and offset:

$$\mathrm{MRSW} = \frac{1}{N_{tel}} \sum_{i=1}^{N_{tel}} \frac{width_i - \langle width \rangle_{MC,i}}{\sigma_{MC,i}} \tag{2.5}$$

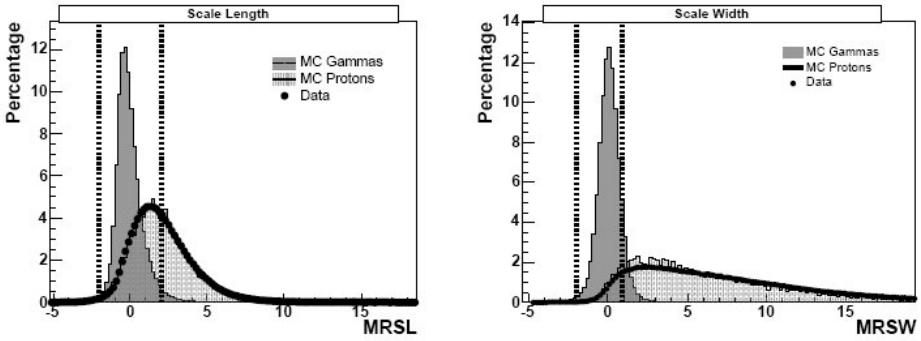


**Fig. 2.11.** MRSL (left) and MRSW (right) distributions for Monte-Carlo simulated $\gamma$-rays and protons and for real off-source data. The dashed vertical lines indicate the min and max cut values (from [Funk, 2005]).

and similar for MRSL. The $\gamma$-hadron-separation is then performed by rejecting all events with MRSW $<$ MRSW$_{min}$ and MRSW $>$ MRSW$_{max}$ (and similarly for MRSL). Most rejection is provided by the cut on MRSW$_{max}$. Since the *shape*-cut can not completely separate the hadronic component, what remains is then referred to as $\gamma$-like event. Since the hadronic background, on the contrary of the $\gamma$-rays, arrives isotropically, a directional cut (used only in the spectral analysis) is also applied, performing an additional efficient background rejection especially for point-like sources. In this case, only events with a squared angular distance $\theta^2$ from the candidate source position smaller than a certain value are kept. For point-like sources, the *standard*-cuts and the *hard*-cuts use slightly different values of $\theta^2$, respectively 0.02° and 0.01°. In the case of extended sources, larger on-source regions have to be used.

*Standard*-cuts and *hard*-cuts are optimized to yield the maximum significance per hour of observations for two different source classes. The first ones are optimized for luminous sources with a flux of 10% of the Crab nebula flux and a similar power-law spectrum ($\Gamma$=2.6) and are mostly used for spectral analysis, as they feature a lower energy threshold than the *hard*-cuts. These ones are optimized for faint point-like sources, with a flux of 1% of the Crab nebula flux and a hard spectrum with index $\Gamma$ = 2.0 and are mostly used for source detections and morphology studies, as they provide a superior sensitivity and angular resolution. They also have the advantage of reducing the background by a factor of 7.

| Configuration | MRSL | | MRSW | | $\theta^2$ | size | Distance |
|---|---|---|---|---|---|---|---|
| | min | max | min | max | max (deg) | min (p.e.) | max (deg) |
| *standard* | -2.0 | 2.0 | -2.0 | 0.9 | 0.02 | 80 | 2.0 |
| *hard* | -2.0 | 2.0 | -2.0 | 0.9 | 0.01 | 200 | 2.0 |

**Table 2.1.** Cuts values.

# 3

# Data analysis

In the previous chapter it has been shown how, after the data collection, almost all background events are rejected during the event reconstruction because of stereoscopic requirements and use of cuts on the reconstructed image. Nevertheless, not all the background can be removed in this way and it actually continues to dominate above the source signal even in the $\gamma$-like events dataset. This is due to hadronic events that are not recognized as such and to electrons and positrons, whose showers, being purely electromagnetic, can not be distinguished from the $\gamma$-rays induced ones. A method for the estimation of the remaining background is hence needed.

First of all, a two dimensional histogram containing all the reconstructed $\gamma$-like events has to be created (raw map). Each bin contains $N \geq 0$ events. A correlated On-map can be constructed in this way: a circle of radius $\theta$ is centered on each bin and the number of events $N_{On} \geq N \geq 0$ within this circle is assigned to that bin.

## 3.1 Signal determination and system acceptance

The $\gamma$-ray signal $N_\gamma$ from any test position is calculated as

$$N_\gamma = N_{On} - \alpha N_{Off} \text{ and the corresponding error } \Delta N_\gamma = \sqrt{N_{On} + \alpha^2 N_{Off}}, \tag{3.1}$$

where $N_{On}$ is the total number of events in the test region (On-region), $N_{Off}$ is the number of background events calculated independently in another region (Off-region) and $\alpha$ is a normalization factor. Since permitting a correct determination of the $\gamma$-ray signal $N_{Off}$ must consist only of background events, known $\gamma$-ray sources must be excluded from the estimation of $N_{Off}$ through the definition of exclusion regions $R_{excl}$. The normalization factor $\alpha$ takes into account the differences in the solid angle, exposure time $t$, zenith angle $\phi_z$ and acceptance $\epsilon$ between On- and Off-regions. The acceptance for $\gamma$-like showers is not a constant, but varies within the field of view as function of the position $(\theta_x, \theta_y)$, of the zenith angle and of the exposure time, dropping rather rapidly towards the edge.

$$\alpha = \frac{\int_{On} \epsilon_\gamma \left(\theta_x, \theta_y, \phi_z, t\right) d\theta_x d\theta_y d\phi_z dt}{\int_{Off} \epsilon_\gamma \left(\theta_x, \theta_y, \phi_z, t\right) d\theta_x d\theta_y d\phi_z dt}. \tag{3.2}$$

For wobble observations (sec. 2.3) and in general for methods that permit the estimation of the

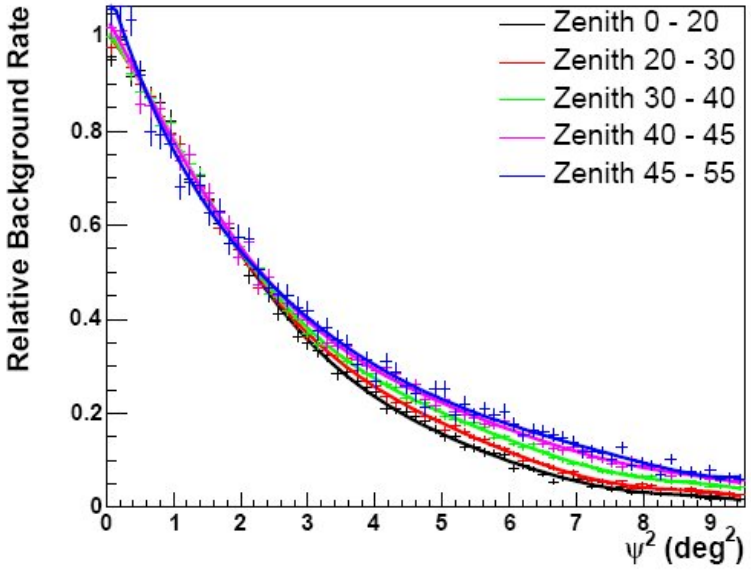


**Fig. 3.1.** System acceptance for different zenith angle bands derived from OFF-runs. These curves are normalized to the integral in the inner 1°. Note that in the picture the offset is referred to as $\Psi$ instead of $\theta$ (from [Funk, 2005]).

background from within the same field of view of the On-region, the exposure time is the same and also the zenith angle very similar for both On- and Off-regions, so that $\alpha$ is reduced to

$$\alpha = \frac{\int_{On} \epsilon_\gamma (\theta_x, \theta_y)\, d\theta_x d\theta_y}{\int_{Off} \epsilon_\gamma (\theta_x, \theta_y)\, d\theta_x d\theta_y} \tag{3.3}$$

To further simplify the estimation of the acceptance, this is assumed to be radially symmetric, so that it depends only on the angular distance $\theta$ from the center of the field of view (i.e. from the pointing position):

$$\alpha = \frac{\int_{On} \epsilon_\gamma (\theta)\, d\theta}{\int_{Off} \epsilon_\gamma (\theta)\, d\theta}. \tag{3.4}$$

As mentioned above, the acceptance is zenith angle dependent (Fig. 3.1). Although this dependence is ignored for each single position in the field of view within the same run, it is taken into account when the acceptance is calculated for different runs. What is completely ignored in the current HESS analysis is instead the (rather strong) energy dependence (Fig. 3.2). This implies the use of an acceptance independent background estimation for the spectral analysis.

The statistical significance $S_\gamma$ of a $\gamma$-ray signal (and more in general of any count signal) is given by the LiMa formula ([Li and Ma, 1983]):

$$S_\gamma = \sqrt{2} \left\{ N_{On} \ln \left[ \frac{1+\alpha}{\alpha} \left( \frac{N_{On}}{N_{On} + N_{Off}} \right) \right] + N_{Off} \ln \left[ (1+\alpha) \left( \frac{N_{Off}}{N_{On} + N_{Off}} \right) \right] \right\}^{1/2} \tag{3.5}$$

In order for this formula to work properly, $N_{On}$ and $N_{Off}$ should be larger than 10. A significance

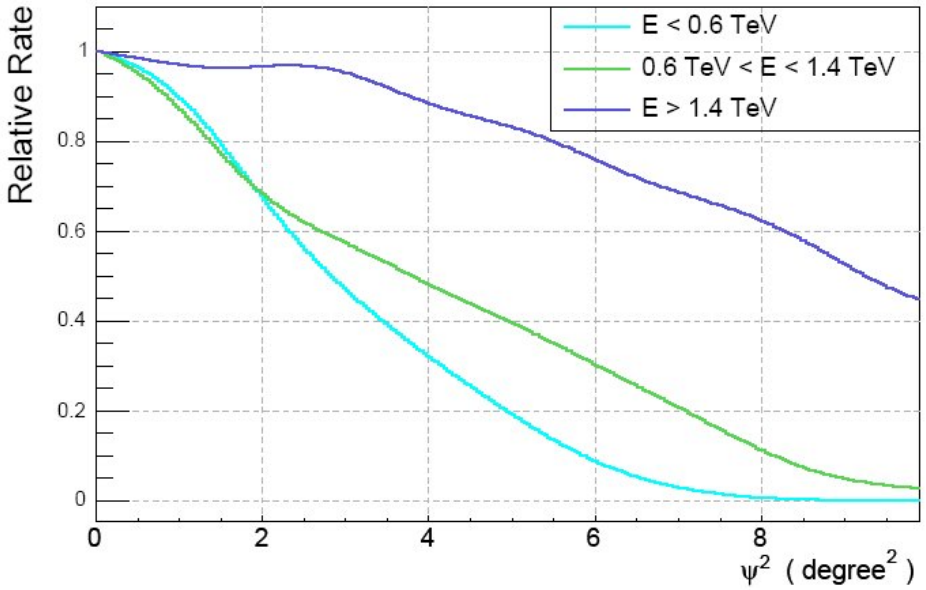


**Fig. 3.2.** System acceptance for three energy bands. The energy dependence is apparent. At small energies the acceptance declines rapidly with increasing offset, while it is much flatter for energies beyond 1.4 TeV. Note that in the picture the offset is referred to as $\Psi$ instead of $\theta$ (from [Berge, 2006]).

of at least 5 standard deviations ($\sigma$) is normally required for the reliable detection of a source. The probability that such a signal is caused by statistical fluctuations is of the order of $\sim 6 \cdot 10^{-5}$.

## 3.2 Background evaluation: 2-D Acceptance Background Model

To extract a two-dimensional $\gamma$-ray excess map from a $\gamma$-like event map, the background must be determined for each position in the sky. Since the system acceptance shows how a flat distribution would be seen by the telescope, and since the background distribution is isotropic, a two-dimensional acceptance map can be used as background model. Such an acceptance map can be created for each observation run by simply rotating the one-dimensional acceptance model correspondent to the run zenith angle around the pointing position. For intermediate values of the zenith angle, the acceptance model is created interpolating linearly between the two nearest zenith angle bands. The run-wise acceptance maps are then simply added together. The resulting "background" map must then be scaled before being subtracted from the raw map. The normalization factor $\alpha$ has to be determined letting the background map match the raw map away from the $\gamma$-ray sources. This method however, is not so reliable because of its susceptibility to gradients that could possibly be present in the acceptance.

During the work, this method was used to estimate the background qualitatively (not quantitatively). Radial profiles of regions in the field of view with no $\gamma$-ray sources were made and added together to reduce statistical fluctuations for both raw map and acceptance map. The resulting profiles were then scaled and compared, showing good agreement in the profile shape. A radial excess profile of the source region was also calculated by subtracting the normalized acceptance profile from the raw map radial profile. This was then compared with the excess obtained using

the Ring Background Model (sec. 3.3). Again, a good agreement was found, showing that the Ring Model interpretes correctly the background.

## 3.3 Background evaluation: The Ring Background Model

A more robust model for the background estimation for excess maps is the Ring Background model. The number of events $N_{Off}$ counting for the background are determined similar to the $N_{On}$ events in the correlated On-map (sec. 3), but in this case, a ring around each bin is used instead of a circle and an Off-map is created (Fig. 3.3). Given a mean radius of the ring (typically 0.5° for point-like sources), the inner and the outer radius are calculated so that the ratio between the On-area $A_{On}$ and the Off-area $A_{Off}$ is $\sim 1/7$. The factor 7 is chosen as a compromise between the need to minimize the statistical fluctuations of the background and that of not let its error become comparable or smaller with respect to the systematic one. As On-area is intended the area of the circle used for the creation of the correlated On-map. One has to make sure that the inner radius is quite larger than the source extension to avoid $\gamma$-ray contaminations. As mentioned before, exclusion region $R_{excl}$ around known $\gamma$-ray sources are defined and the ring-bins that lie in one $R_{excl}$ are not taken into account in the background estimation. This has as consequence the reduction of the Off-area, so that the ratio $A_{On}/A_{Off}$ becomes larger than 1/7. The normalization factor $\alpha$ can not be taken merely equal to the ratio $A_{On}/A_{Off}$, since the acceptance within the ring is not constant, covering the ring areas with different offsets from the camera center. Therefore, to take into consideration both the change of the acceptance and the area ratio, the following is done: On- and an Off-maps are created also for the acceptance map, exactly in the same way as for the $\gamma$-like event map. $\alpha$ is then given for each bin as the ratio between the bin content of the On- and the Off- acceptance maps. The resulting map is a correlated excess map. Instead of the On-maps, the raw $\gamma$-like and acceptance maps can also be used, resulting in an uncorrelated excess map. There is no intrinsic difference between the two excess maps, being one the correlated map of the other.

This kind of background estimation has different advantages with respect to the Region Background Model described in sec. 3.4. First of all, the background can be estimated in each point of the sky, a fact that makes it very suitable for the creation of sky-maps. Moreover, any linear gradients in the background are averaged out and deviations of the actual acceptance from the model acceptance function do not affect it appreciably. Instead, the main important disadvantage of this method is the fact that the energy dependence of the acceptance is completely ignored. The estimation of the excess in function of the energy is then affected by systematic errors, disfavoring in principle the utilization of the Ring Method for the evaluation of energy spectra.

## 3.4 Background evaluation: The Reflected Region Background Model

A background estimation that takes into account neither the energy dependence of the acceptance nor its offset-dependence is the Reflected Region Background Method. It just assumes the system acceptance to be rotationally symmetric. In this case, the background is estimated adding all the events of regions which have the same size and offset from the camera center as the On-region (Fig. 3.3). On- and Off-regions lie on the same ring around the observation position, therefore energy

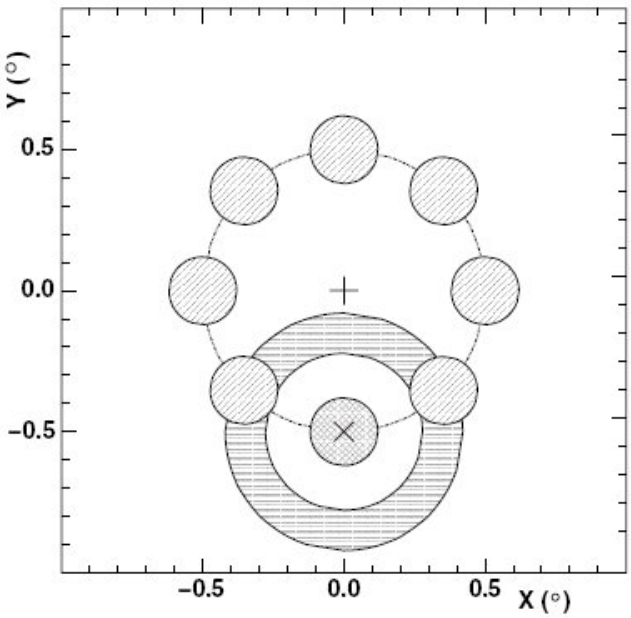


**Fig. 3.3.** Schematic illustration of the Ring and Region Background Models. The observation position of the telescopes is marked by a cross, the target position by an X. The On-region around the target position is marked by a cross-hatched circle. The Ring Background region is filled by horizontal lines, while the Reflected Region Background regions are filled by diagonal lines. In this case the two background regions have equal area (taken from [Aharonian et al., 2006a]).

and offset corrections can be avoided. To prevent $\gamma$-ray contaminations a minimum distance between On- and Off-regions is required and Off-regions overlapping with $R_{excl}$ are rejected. The number of Off-regions $N_{Off}^{reg}$ also depends from the size and offset of the On-region. Finally, the normalization factor $\alpha$ can be simply calculated as $1/N_{Off}^{reg}$.

This model is well suited for wobble observations (sec. 2.3) and for the spectral analysis, since the background estimation is energy independent. It actually requires the On-region to be offset from the camera center of a distance larger than the radius of the source, otherwise no Off-region can be determined. In this case another method has to be used, for example the background can be extracted from corresponding OFF-runs like in the case of ON/OFF observations (sec. 2.3). The number of Off-regions, however, is reduced to one and a good reduction of statistical fluctuations is not possible.

The main advantage of this method is the fact that On- and Off-events have the same acceptance, not needing the acceptance itself (and the relative corrections) to be taken into account, as long as it can be considered rotational symmetric for the system.

The Region Background Method does not permit the calculation of the background in each point of the field of view, therefore the creation of sky-maps is prevented. Another disadvantage is given from the fact that the number of Off-regions depends strongly on the size and offset of the On-region and on the presence of excluded regions. The larger the size and the number of $R_{excl}$, the smaller $N_{Off}^{reg}$ is, with the concrete possibility of not finding Off-regions for certain observation runs.

## 3.5 Position fitting

The position and size of the $\gamma$-ray source are determined through the two dimensional fit of the sky map, assuming that the centroid of the emission is not energy dependent and that source intensity profile has a radially symmetric Gaussian form. Normally a fine binning, an uncorrelated sky map and hard cuts are used, since they provide a better angular resolution (see sec. 2.6). The fitting procedure has to take into account also the intrinsic PSF of the instrument, that is usually described by a double Gaussian:

$$\mathrm{PSF} \propto K_1 \exp^{-\frac{\theta^2}{2\sigma_1^2}} + K_2 \exp^{-\frac{\theta^2}{2\sigma_2^2}} . \tag{3.6}$$

Given the Gaussian intensity profile

$$I\left(\theta^2\right) = K_{source} \exp^{-\frac{\theta^2}{2\sigma_{source}^2}} , \tag{3.7}$$

the actual fit function results from the convolution of these two functions

$$N_\gamma\left(x,y\right) = \mathrm{PSF}_{\mathrm{2D}}\left(x,y\right) = K_{source}\left[e^{-\frac{\theta^2}{2(\sigma_1^2+\sigma_{source}^2)}} + \frac{K_2}{K_1}\frac{\sigma_2^2}{\sigma_1^2}\frac{\sigma_1^2+\sigma_{source}^2}{\sigma_2^2+\sigma_{source}^2}e^{-\frac{\theta^2}{2(\sigma_2^2+\sigma_{source}^2)}}\right], \tag{3.8}$$

with

$$\theta^2 = \left[\left(X_0 - x\right)a\right]^2 + \left(Y_0 - y\right)^2 . \tag{3.9}$$

$(X_0, Y_0)$ is the centroid position, $(x, y)$ are the coordinates of the point on the sky-map and $a = 1/\cos\left(y\right)$ is a scaling factor due to the use of the spherical RA-Dec coordinate system with non Cartesian metrics. Free fit parameters are $(X_0, Y_0)$, the normalization factor $K_{source}$ and the source width $\sigma_{source}$. The PSF parameters are derived from MC simulations and depend on the zenith and offset distributions of the dataset.

Function 3.8 can be used to fit both the (uncorrelated) excess and the raw map. In the first case, the map is usually created using the Ring Background Method and the source is directly fit. If the emission region has an elliptical shape, an elongated Gaussian can be used instead of the simple Gaussian. In the second case the background is not yet subtracted and it is taken into account by adding a background component to $N_\gamma(x, y)$. This additional component can be a constant ($B_0$) or a two dimensional single Gaussian ($K_{back} \exp^{-\theta_{back}^2/2\sigma_{back}^2}$). In the first case, the background is assumed to be flat and is calculated from a ring around the source position. In the second one, it is determined in a previous step in which the background map is fit similarly to the On-map. Also in this case, the background map is created with the Ring Background Method.

Another difference between the fit to the excess map and to the raw On-map is the fact that in the latter case, the bins contain counting statistic so that Poisson statistic and likelihood fit are applicable, while in the other one this does not happen. The bin size has therefore to be arranged so that the statistic is sufficient and a Gaussian approximation is valid.

## 3.6 Spectral analysis

The spectral analysis is probably the most important part of the analysis of any source because it gives information about the physical processes and interactions occurring inside of it. In the case of $\gamma$-ray sources the particles acceleration mechanisms can be studied. The differential energy spectrum (or differential flux) is defined as the number of $\gamma$-rays $N_\gamma$ per unit of time $dt$, area $dA$ and energy $dE$ (therefore one has counts $\mathrm{TeV}^{-1} cm^{-2} s^{-1}$):

$$F(E) = \frac{dN_\gamma}{dt_{live} dA_{eff} dE}. \tag{3.10}$$

Here $t_{live}$ is the livetime of the observation and $A_{eff}$ the effective area of the run (see sec. 3.6.1).

For the evaluation of the spectrum the analysis has to be performed individually for each observation run. Histograms with a fine binning of 24 equal bins ($\Delta log(E) = const$) per energy decade are filled for both On- and Off-events. The bin width is smaller than the energy resolution. The effective area $A_{eff}$ is calculated using the mean values of the zenith and offset distributions of the On-events. The same $A_{eff}$ is assigned to the Off-events, under the assumption that they have the same system acceptance as the On-events. $A_{eff}$ is then multiplied by the observation livetime ($TA_{eff}$). Energy thresholds are applied at both low and high energy and are determined for each individual run on the basis of the zenith and offset angle of the pointing position. At low energies, the threshold is defined as the minimum energy for which the energy bias between the real and the reconstructed energy is less than 10%, so that too large of a bias which can lead to significant systematic errors are avoided. Moreover, also the initial strongly rising part of the effective areas that could suffer an imperfect description by the MC simulations is not taken into consideration. The high energy threshold is applied because the event statistics beyond it is not sufficient to derive meaningful values for the effective area. At this point, the run-wise histograms are summed together to obtain the On- and Off-histograms valid for the whole data set. A rebinning can also be performed taking into account the bin significance (*adaptive* rebinning) or giving to the bin a fixed size (*fixed* rebinning). In the rebinning the On- and Off-events are merely added, while the effective areas are averaged using an arithmetic mean. The flux histograms are created dividing the event histograms by $TA_{eff}$ and by the bin width $dE$. The differential source flux for each bin $i$ is then given by:

$$F_i(E) = \frac{N_{On,i}}{\Delta E_i} \sum_{runs} \frac{1}{TA_{eff,i}(\phi_z, \theta)} - \frac{N_{Off,i}}{\Delta E_i} \sum_{runs} \frac{1}{\alpha_{run}} \frac{1}{TA_{eff,i}(\phi_z, \theta)}, \tag{3.11}$$

where $\alpha_{run}$ is the background normalization factor derived from the background estimation. At last, the spectral points are fitted using a minimum $\chi^2$ procedure. One of the possible fit functions is a power-law:

$$F(E) = F_0 \left( \frac{E}{1\mathrm{TeV}} \right)^{-\Gamma}, \tag{3.12}$$

where $F_0$ is the flux normalization at 1 TeV and $\Gamma$ is the spectral index.

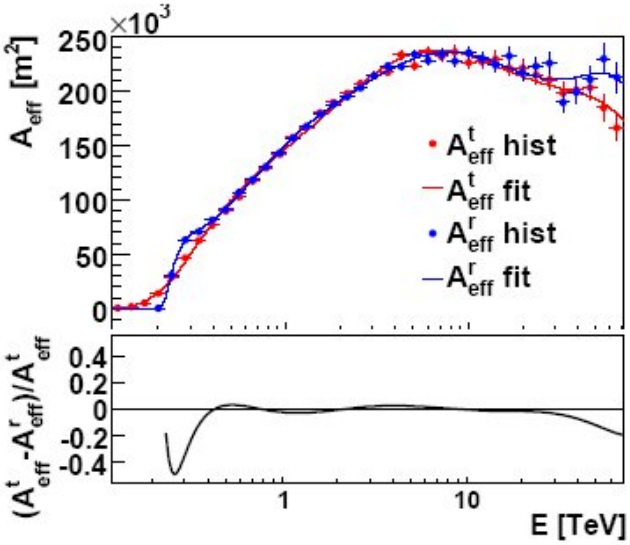


**Fig. 3.4. Top**: Effective areas as function of the reconstructed (blue) and true MC (red) energy for a zenith angle $\phi_z = 20°$, an offset angle $\theta = 0.5°$ and *standard*-cuts. The markers illustrate the MC results, while the lines are their analytical fits. **Bottom**: Effective area residuals between true and reconstructed energy (from [Hoppe, 2008]).

### 3.6.1 Effective area

The effective $\gamma$-ray collection area expresses the area within which the instrument can detect a $\gamma$-event, given its detection efficiency. It is given by

$$A_{eff}\left(E, \phi_z, \theta, \nu_{az}\right) = \int 2\pi r dr P, \tag{3.13}$$

where $P$ is the $\gamma$-ray detection probability that depends also on the efficiency of the $\gamma$-ray selection (i.e on the cuts), $r$ is the distance of the shower core from the center of the array, $\phi_z$ is the zenith angle, $\theta$ is the offset from the camera center and $\nu_{az}$ is the azimuth angle. The effective area has to be determined through MC simulations. This is done for different $\gamma$-ray selection cuts and for different sets of zenith, offset and azimuth angles (Fig. 3.5):

$$\begin{gathered}\phi_z = 0°, 20°, 30°, 40°, 45°, 50°, 55°, 60°, 63°, 65° \\ \theta = 0°, 0.5°, 1°, 1.5°, 2°, 2.5° \\ \nu_{az} = 0°, 180° \ .\end{gathered}$$

For each combination $N_\gamma^{MC}$ events following a power-law spectrum with spectral index $\Gamma = 2$ are simulated homogeneously on an area $A_{MC}$. The effective areas are then given as:

$$A_{eff}\left(E, \phi_z, \theta, \nu_{az}\right) = \frac{N_\gamma^{sel}}{N_\gamma^{MC}} A_{MC}, \tag{3.14}$$

where $N_\gamma^{sel}$ is the number of $\gamma$-like events that have passed all kind of cuts. These are then interpolated linearly in $\cos(\phi_z)$ and $\theta$ to obtain effective areas valid for arbitrary sets of $(\phi_z, \theta, \nu_{az})$.

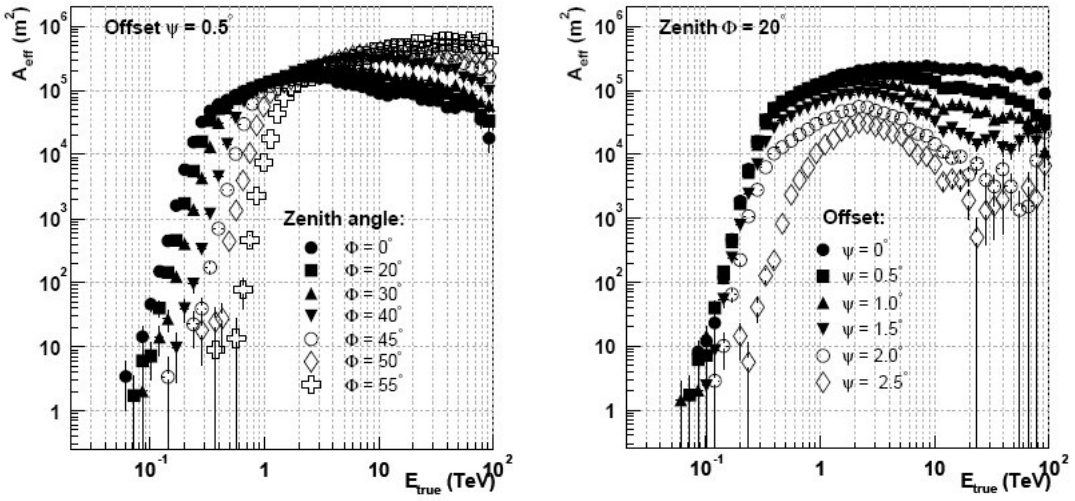


**Fig. 3.5. Left**: Effective area as a function of the true energy for different zenith angles at fixed camera offset $\theta = 0.5^\circ$ and fixed azimuth angle $\nu_{az} = 180^\circ$. **Right**: Effective area as function of the true energy for different camera offsets at fixed zenith angle ($\phi_z = 20^\circ$) and fixed azimuth angle $\nu_{az} = 180^\circ$. An increase of the energy threshold with increasing zenith angle as well as increasing offset is apparent. Note that in the picture the zenith angle is referred to as $\Phi$ and the offset as $\Psi$.(from [Funk, 2005]).

No interpolation is done for $\nu_{az}$ since the dependence on this parameter is rather weak. The azimuth angle actually characterizes two different sets of areas, the *north* ($\nu_{az} = 0^\circ$) and the *south* ($\nu_{az} = 180^\circ$) effective areas. This takes into account the fact that the development of the electromagnetic showers is influenced by the earth magnetic field. Since the effective areas depend on the cuts with which they are produced, they can just be used in analysis that use the same cut. As it has been seen in sec. 2.6 the cuts are also described by the On-source area $\theta^2$. Two kind of effective areas are defined: the *point-source* effective areas and the *full-enclosure* effective areas. In the first case, the value of $\theta^2$ is optimized for the analysis of point sources, in the latter, the On-source region is taken infinitely large. Lastly, also the telescope multiplicity (3 or 4 telescope running) is taken into account.

# 4

# HESS J1804-216

## 4.1 The source

HESS J1804-216 (Fig. 4.1) is an extended galactic source, discovered in the inner part of the Galactic Plane during the 2004-2005 HESS Galactic Plane Survey ([Aharonian et al., 2005a], [Aharonian et al., 2006b]). The Survey was performed with observations in a band of $\pm 30^\circ$ in longitude around the Galactic Center ($l = 0$) and at three different latitudes $b = +1^\circ, 0^\circ, -1^\circ$. The pointing positions differ by $0.7^\circ$ in longitude. At the time of its discovery, HESS J1804-216 was the largest of the new VHE $\gamma$-ray emission regions with a size of approximately $22'$ and still now it is one of the most extended known TeV sources. It is also characterized by a high brightness, with a flux of $\sim 25\%$ of the Crab Nebula above 200 GeV, and it is one of the softest sources, with a photon index $\Gamma = 2.72 \pm 0.06$. HESS J1804-216 is still unidentified, but several possible counterparts like pulsars (PSR) and supernova remnants (SNR) are in its neighborhood, though none of them is perfectly lined up with the TeV emission. HESS J1804-216 was observed in the TeV range also with CANGAROO-III by [Higashi et al., 2008], who confirm the extended morphology of the source and find values for the flux and the spectral index that are consistent with those found by HESS. Recently FERMI detected a $\gamma$-emission (0FGL J1805.3-2138), whose centroid lies well inside of HESS J1804-216, even if with an offset of $\sim 14.4'$ from the HESS centroid ([Abdo et al., 2009]). Among the possible counterparts it was suggested by [Aharonian et al., 2006b] the association with the south-western part of the shell of the SNR G8.7-0.1 (radius $\sim 26'$) or with the young Vela-like pulsar PSR B1800-21 (or PSR J1803-2137) ([Kassim and Weiler, 1990b]). In X-rays two possible counterparts were discovered by Suzaku near the center of HESS J1804-216: Suzaku J1804-2142 (Src1) and Suzaku J1804-2140 (Src2) ([Bamba et al., 2007]). The same sources were detected by Chandra ([Cui and Konopelko, 2006] and [Kargaltsev et al., 2007b], Fig. 4.3) and Src2 also by SWIFT ([Landi et al., 2006]). SWIFT detected other two sources in the same region, but both are associable to bright stars. At radio wavelengths the compact SNR G8.31-0.09 was discovered well inside the HESS emission ([Brogan et al., 2006], Fig. 4.2).

The brightness and extension of HESS J1804-216 make it possible to use TeV data to look for possible structures in the morphology and gradients in the spectrum, resulting in the opportunity to identify one of the several objects in its neighborhood as the actual counterpart.

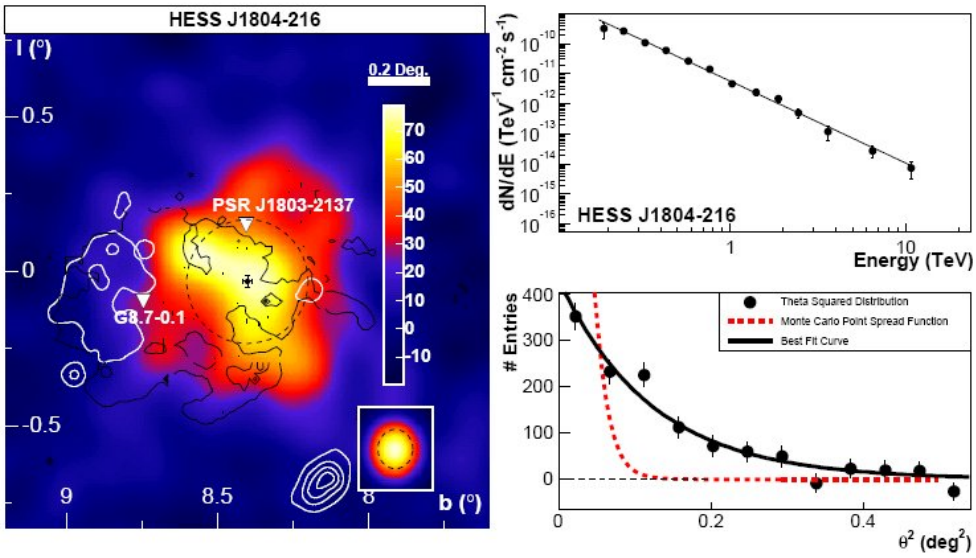


**Fig. 4.1.** HESS 1804-216 as appears in [Aharonian et al., 2006b]. **Left**: Smoothed excess map (smoothing radius 0.06°) of the HESS J1804-216 region with nearby pulsars and SNRs as possible counterparts. The white contours show the X-ray emission from G8.7-0.1 as detected by the ROSAT satellite in the 0.51-2.01 keV band ([Finley and Ögelman, 1994]), the black contours show the 20 cm radio emission detected by the VLA. **Right**: differential energy spectrum (top) and the radial $\theta^2$ distribution (bottom).

## 4.2 The possible counterparts

In the following the five possible counterparts listed above are briefly described. Also other three objects that lie in the neighborhood of HESS J1804-216 are presented.

- SNR G8.7-0.1: it is associated with the W30 complex, visible at radio wavelength as superposition of extended and smaller emission regions. Discrete H-II regions are present as well as molecular clouds, in which massive star formation may be occurring ([Ojeda-May et al., 2002]). The SNR nature of G8.7-0.1 was clearly determined by the detection of non-thermal extended radio emission ([Kassim and Weiler, 1990b]). A diffuse X-ray emission interpreted as thermal was detected by ROSAT in the northern half of the remnant in the range 0.51-2.01 keV ([Finley and Ögelman, 1994]). The distance was estimated using several methods that give slightly different results: $6 \pm 1$ kpc by [Kassim and Weiler, 1990b], $\sim$4.8 kpc by [Finley and Ögelman, 1994]. Its age was estimated by [Odegard, 1986] from the relation between the age and the surface brightness in the radio band to be $1.5 \cdot 10^4$ years and by [Higashi et al., 2008] under the assumption of a distance of 4.8 kpc to be $2.2 - 3.1 \cdot 10^4$ years. Its offset from the HESS centroid is $\sim 24'$ and its diameter is $\sim 50'$.

- PSR B1800-21 (PSR J1803-2137): it is a young Vela-like pulsar discovered during radio observations ([Clifton and Lyne, 1986]) and has an offset of $\sim 11'$ from the centroid of HESS J1804-216. It has a spin period $P$ of 133.6 ms, a spin period derivative $\dot{P}$ of $1.34 \cdot 10^{-13}$, a characteristic age $\tau_c$ of 15.8 kyears and a distance $d$ of $3.84^{+0.39}_{-0.45}$ kpc ([Brisken et al., 2006]). The resulting spin-down luminosity is $\dot{E} = 2.2 \cdot 10^{36}$ ergs/s or $\dot{E}/d^2 = 1.4 \cdot 10^{35}$ ergs/kpc$^2$·s

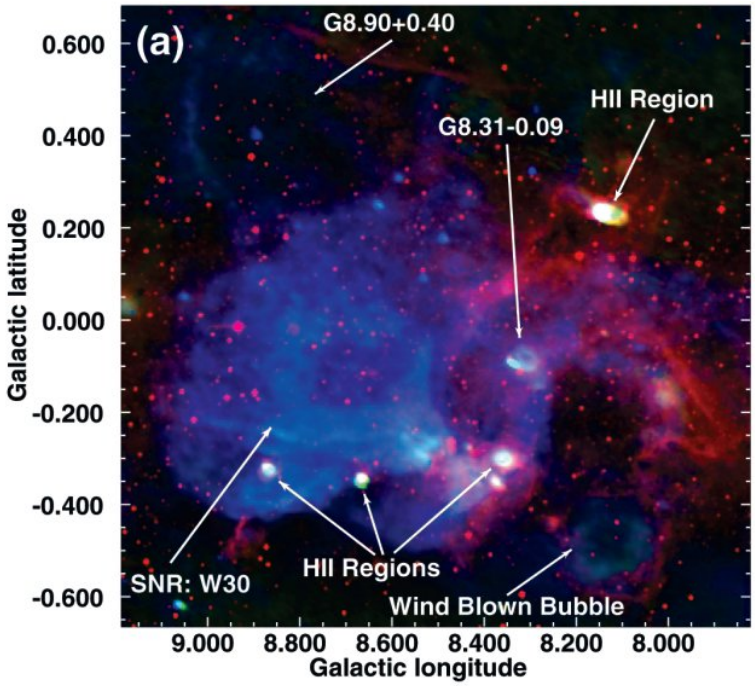


**Fig. 4.2.** Three-color image from VLA 90 cm (blue), MSX 8 mm (red), and SGPS+VLA 20 cm (green) data. The complex W30, SNR G8.31-0.09 and SNR G8.90+40 are visible, together with several H-II regions (from [Brogan et al., 2006]).

assuming the distance reported above. Given these values, [Aharonian et al., 2006b] state that the required efficiency to possibly power the $\gamma$-ray emission of HESS J1804-216 is only 1%, therefore PSR B1800-21 is considered the most likely counterpart. Based on ROSAT observation, a faint X-ray source near the radio pulsar position was attributed to PSR B1800-21 by [Finley and Ögelman, 1994]. The detection of an X-ray nebula around the pulsar was reported also by [Cui and Konopelko, 2006] and [Kargaltsev et al., 2007a], who saw two structures: a brighter compact $7'' \times 4''$ component (the inner PWN) and an extended ($12''$) fainter emission component (the outer PWN), both asymmetric with respect to the pulsar position and extended toward HESS J1804-216. This makes think about a PWN nature of HESS J1804-216.

- Suzaku J1804-2142 (Src1): it is offset $3'$ from the centroid of HESS J1804-216. It is reported by [Bamba et al., 2007] as point-like source (or at least compact with respect to the spatial resolution of Suzaku) with a diameter of $2'$, while by [Kargaltsev et al., 2007b] as extended or multiple ($1.5'$-$2'$) with a Chandra observation. Taking into account the spectral features, [Bamba et al., 2007] suggested that this source could probably be a high-mass X-ray binary (HMXB). Due to the low signal-to-noise ratio, [Kargaltsev et al., 2007b] were just able to estimate the unabsorbed flux using the best-fit parameters reported by [Bamba et al., 2007]. It revealed to be a factor of 1.7 smaller than that calculated from the Suzaku observation. This difference could be explained by systematic errors or by the variability of the source, fact that would support the HMXB interpretation.

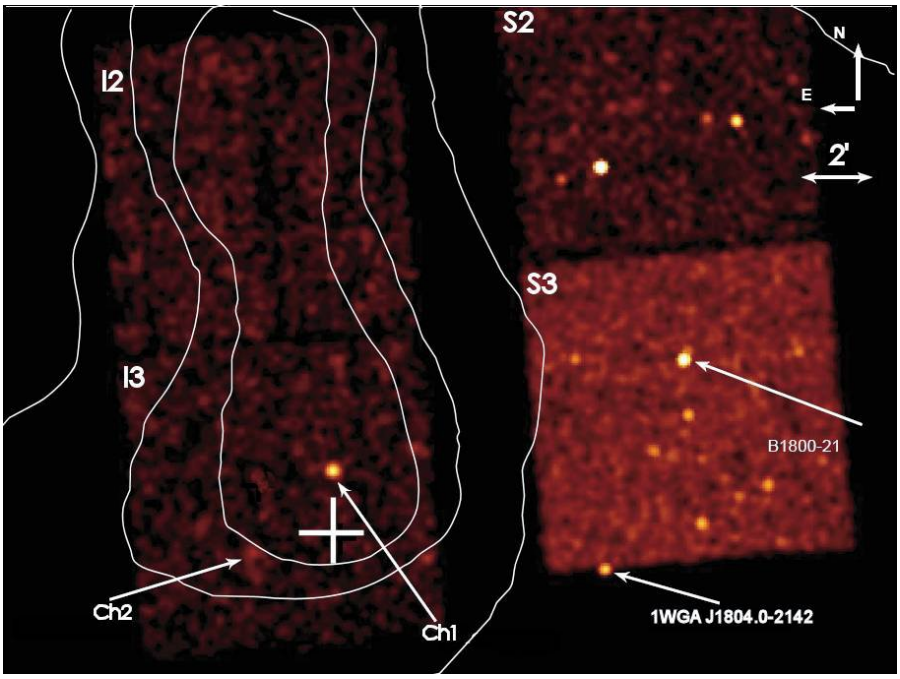


**Fig. 4.3.** Chandra ACIS image in the range 0.5-8 keV of the central part of HESS J1804-216 with the TeV contours overlaid. The best-fit position of HESS J1804-216 and its uncertainty are marked by the plus sign. The arrows indicate the sources Src1 (Ch2 in the image), Src2 (Ch1 in the image), and the pulsar B1800-21 (from [Kargaltsev et al., 2007b]).

- Suzaku J1804-2140 (Src2): it is offset 1.8′ from the centroid of HESS J1804216. It is reported by [Bamba et al., 2007] as extended or multiple, while by [Kargaltsev et al., 2007b] as point-like source. Since the Suzaku observations are more sensitive, a fainter extended PWN component could have been detected. For both [Bamba et al., 2007] and [Kargaltsev et al., 2007b] the best spectral fit is an absorbed power-law in which the absorbing column density is appreciably larger than the expected Galactic column. [Kargaltsev et al., 2007b] stated that Src2 could be located within (or even beyond) the Galactic Bulge, or that it shows an intrinsic absorption, which is often seen in the X-ray spectra of HMXBs. Furthermore they reported a pulsation of 106 s, which supports an HMXB interpretation. [Bamba et al., 2007] suggested instead that Src2 is a PWN or a shell-like SNR because of the extended morphology observed with Suzaku and the best-fit photon index of ∼1.7.

- SNR G8.31-0.09: it was discovered at radio wavelength (90 cm, 1.4 GHz) during a Galactic Plane survey conducted by the Very Large Array (VLA). It has a size of $5' \times 4'$, and an offset from the centroid of HESS J1804-216 of $7'$. The morphology is shell-like and the spectral index is $\alpha_r = 0.6$ for $F_\nu \propto \nu^{\alpha_r}$ ([Brogan et al., 2006]).

Due to the relative small offset between PSR B1800-21 and G8.7-0.1 and to their similar estimated distances, the association between these two objects has been discussed in several papers (e.g. [Finley and Ögelman, 1994], [Kassim and Weiler, 1990a]). Recently however it was showed by [Brisken et al., 2006] that the pulsar's proper-motion is driving the pulsar more nearly toward

the center of G8.7-0.1, rather than away from it, and this fact makes their association rather unlikely.

Other objects present just outside the TeV emission region are:

- PSR J1806-2125: it was discovered during the Parkes multibeam pulsar survey ([Morris et al., 2002]). It has an offset of $\sim 30'$ from the centroid of HESS J1804-216 and lies just outside the TeV emission on the north-est side, but inside the radio emission of SNR G8.7-0.1. It has a spin period $P$ of 481.8 ms, a spin period derivative $\dot{P}$ of $1.17 \cdot 10^{-13}$, a characteristic age $\tau_c$ of 65 kyears and a distance $d$ of 9.9 kpc ([Hobbs et al., 2002]). Since the distance is almost a factor two larger than that of SNR G8.7-0.1, it can not be physically related to this one. The spindown luminosity is $\dot{E} = 4.1 \cdot 10^{34}$ ergs/s or $\dot{E}/d^2 = 4.2 \cdot 10^{32}$ ergs/kpc$^2$·s assuming the distance reported above. Almost spatially coincident with PSR J1806-2125 (offset $\sim 1.6'$), but at the distance of SNR G8.7-0.1, a Maser OH(1720 MHz) emission was recently discovered ([Hewitt and Yusef-Zadeh, 2009]).

- PSR J1804-2228: it was also discovered during the Parkes multibeam pulsar survey ([Morris et al., 2002]). It has an offset of $\sim 46.2'$ from the centroid of HESS J1804-216 lieing well outside the TeV emission on the south part. It has a spin period $P$ of 570.5 ms, a spin period derivative $\dot{P}$ of $0.14 \cdot 10^{-15}$ and a distance $d$ of 5.3 kpc ([Morris et al., 2002]). The spindown luminosity is $\dot{E} = 3.0 \cdot 10^{31}$ ergs/s or $\dot{E}/d^2 = 1.1 \cdot 10^{30}$ ergs/kpc$^2$·s assuming the distance reported above. Since the spin-down energy is so low and the pulsar lies well outside of the TeV emission region, it is very unlikely as counterpart.

- SNR G8.90+0.40: it is a very faint shell like supernova remnant discovered at radio wavelength (90 cm, 1.4 GHz) during a Galactic Plane survey conducted by the Very Large Array (VLA). It has a size of $24' \times 24'$, and an offset from the centroid of HESS J1804-216 of $\sim 39.6'$. The spectral index is $\alpha_r = 0.6$ for $F_\nu \propto \nu^{\alpha_r}$ ([Brogan et al., 2006]).

## 4.3 Dataset

For the analysis of HESS J1804-216, runs relative to observations made between the 21st May 2004 and the 9th October 2007 were used. Only runs with a 4 telescope multiplicity and with a declination $> -23°$ (*north*-runs) were taken into account. On the basis of the offset of the HESS centroid from the observation position two lists were generated. The first one containing 83 runs within an offset of 2.5° (mean offset 1.52°) was used for the morphological analysis, the second one containing 58 runs within an offset of 2.0° (mean offset 1.22°) was used for the spectral analysis. This was done because the event reconstruction, and in particular the energy reconstruction, becomes less precise with increasing offset due to the radial and energy dependence of the acceptance (sec. 3.1). For the spectral analysis is then preferable to reduce the field of view in order to obtain a better energy resolution. All the runs were taken in survey mode, no dedicated wobble observation was performed on HESS J1804-216. In Fig. 4.4 the offset distribution of the two lists is shown.

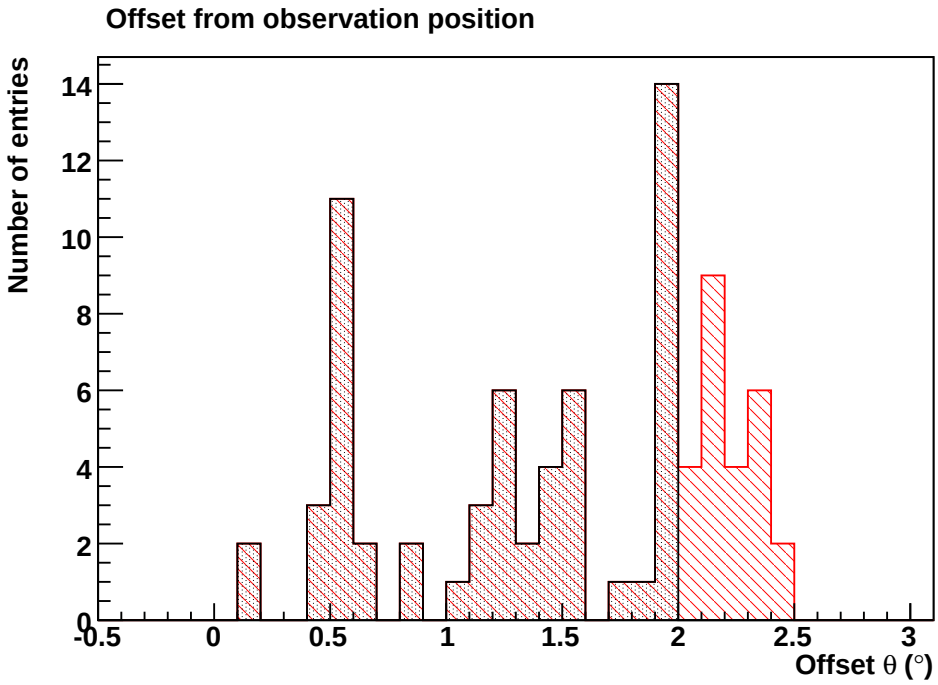


**Fig. 4.4.** Offsets distribution of the runs. Dotted black is the 2.0° list, dashed red is the 2.5° list.

## 4.4 Background estimation and significance

When the data are analysed, first of all a $\gamma$-like event raw skymap and an acceptance map are created for each run and divided into a fine binned grid (here a binsize of $0.02° \times 0.02°$ was chosen). The raw skymap is centered on the observation position and contains all the events that have passed the selection cuts, the acceptance map is created rotating the one-dimensional acceptance curve of that specific run. The single-run maps are then added together to obtain the raw skymap and the overall acceptance map of the entire region. During this step a maximal offset from the observation position (*bgrange* from now on) can be defined, so that only events inside this radius are taken into account. This is valid for both sky and acceptance maps.

For the background estimation of the skymaps the Ring Background Method was used (sec. 3.3). For each grid point the background was estimated in a ring with mean radius *ring-radius*=1.0° and an area 7 times the On-region area[1] $\theta^2 = 0.05(°)^2$ ($\theta \approx 0.22°$). Such a large *ring-radius* was chosen to be bigger than the diameter of the source, so that the ring is not affected too much by exclusion regions and the ratio $A_{On}/A_{Off}$ doesn't suffer large variations on the entire source. *Hard*-cuts (sec. 2.6) were chosen because they provide a much higher angular resolution and reduce the number of background events with respect to *standard*-cuts, even if at the expense of a smaller statistic and higher energy threshold. Events were considered within a *bgrange* of 2.5°. The statistical significance of HESS J1804-216 was calculated for the On-region $\theta^2$ centered on the source centroid position given in [Aharonian et al., 2006b] (R.A. 271.13° Dec -21.7°). The LiMa formula was used (sec. 3.1, [Li and Ma, 1983]), taking into account the On- and

[1] Note that this area is not the area of the source, that is actually much more extended.

**Table 4.1.** On-counts, scaled background ($\alpha$·Off-counts), excess, significance and livetime for the On-source region centered on the centroid of HESS J1804-216. A comparison with the literature values is shown. It has to be noted that for the CANGAROO-III analysis the On-source region is slightly more extended as for HESS and the energy threshold is higher.

| | New results *hard*-cuts | [Aharonian et al., 2006b] *hard*-cuts | [Higashi et al., 2008] E>600 GeV $\theta^2 < 0.06\ deg^2$ |
|---|---|---|---|
| On-Counts | 1268 | 887 | |
| Scaled Background | 660 | 508 | |
| Excess | 608 | 379 | 512±61 |
| Significance | 18.99 | 13.9 | 10.0 |
| Livetime (hr) | 35.34 | 15.7 | 76 |

Off-counts and the normalization factor $\alpha$ of this region. In about 35 hours of effective lifetime 608 excess events were detected, with a significance of ∼19. In Table 4.1 a comparison between the values obtained in the analysis and those published in [Aharonian et al., 2006b] and [Higashi et al., 2008] is shown.

The relative correlated significance distribution is shown in Fig. 4.5(a) for the whole region within 3.0° from the centroid of HESS J1804-216 and in Fig. 4.5(b) for the same region without the known $\gamma$-ray sources, taking into account therefore only the background. The Gaussian fit of this last distribution gives a mean value of -0.048±0.005 and a standard deviation of 1.055±0.003. If the background is determined correctly, the corresponding significance distribution should follow a perfect normal distribution with a mean of 0 and a standard deviation of 1. Since the discrepancy is just in the order of few percent, this indicates that the Ring Background Method evaluates the background correctly and that all $\gamma$-ray sources in the field of view were properly taken into account.

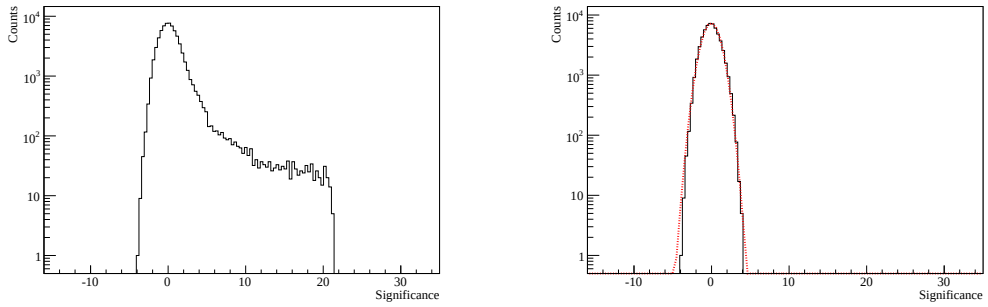


(a) (b)

**Fig. 4.5.** Correlated Significance distribution within a radius of 3.0° from the source centroid: (a) of the whole skymap (b) of background regions. The background distribution is fit with a Gaussian (red pointed line) of mean value -0.048±0.005 and width 1.055±0.003.

## 4.5 Morphology and position of HESS J1804-216

For the morphological and positional analysis the same parameters as before were used, except for the bin size, that was reduced to $0.006° \times 0.006°$ to permit an accurate determination of the position of the $\gamma$-events on the skymap. Under the assumption of a Gaussian intensity profile of HESS J1804-216 the uncorrelated excess map was fit using function 3.8 as described in sec. 3.5. Also fits on the raw skymap were performed, but the results were not satisfactory. The reason can be found in the fact that the fit functions suppose the background being either flat or Gaussian, but for the dataset used it can actually not be considered flat and it is badly described by a Gaussian distribution. The results of the position fitting are summarized in Table 4.2. In Fig 4.6 the differences between the new results and those of [Aharonian et al., 2006b] are graphically represented.

**Table 4.2.** Test position and size. All the values are given in degrees.

| | Best fit position | | | | $\sigma_{source}$ |
|---|---|---|---|---|---|
| | R.A. | Dec. | $l$ | $b$ | |
| New results | 271.155±0.013 | -21.691±0.012 | 8.419 | -0.04 | 0.212±0.008 |
| [Aharonian et al., 2006b] | 271.13 | -21.7 | 8.401±0.016 | -0.033±0.018 | 0.200±0.010 |
| [Higashi et al., 2008] | 271.079 | -21.727 | 8.353 | 0.000 | 0.160×0.274 |

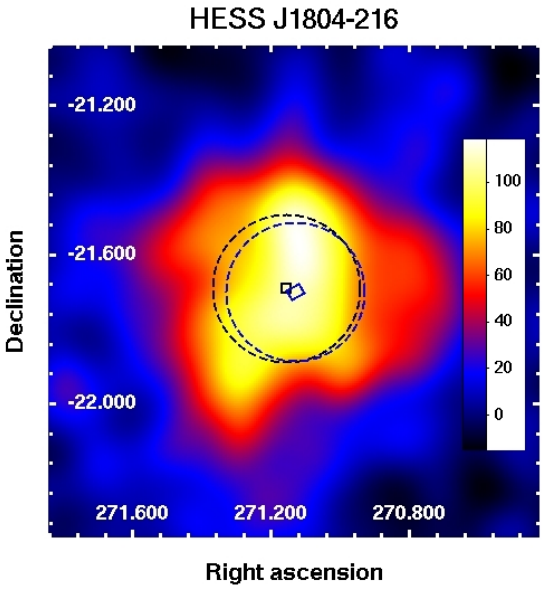


**Fig. 4.6.** HESS J1804-216 smoothed excess map (gaussian smooth 0.06°). The blue box and circle represent the position and size as given in [Aharonian et al., 2006b], the black ones those derived in the current analysis.

It is apparent from Fig. 4.6 that the emission of HESS J1804-216 does not follow a Gaussian distribution. Some structures are visible. The curved form of the central part of the emission suggests a spatial coincidence with the south-west part of SNR G8.7-0.1 (as already reported by [Aharonian et al., 2006b]) and the bow-shape of the emission in the southern part just below SNR G8.31-0.09 seems to follow the radio emission detected at 90 GHz by the VLA ([Brogan et al., 2006]).

## 4.6 Spectral analysis of HESS J1804-216

For the spectral analysis of the entire source HESS J1804-216 the background was estimated using the Region Background Method to avoid the need of taking into account energy corrections, since the offset distribution is the same for On- and Off-events (see sec. 3.4). *Standard*-cuts (sec. 2.6) with *full-enclosure* effective area (sec. 3.6.1) were used in order to increase the statistic, reduce the energy threshold (therefore be able to derive a spectrum for a wider energy range with respect to *hard*-cuts) and take into account the extended nature of the source. An On-region of radius $\theta = 0.36^\circ$ ($\theta^2 = 0.1296(^\circ)^2$) was chosen, centered on the source position as given in [Aharonian et al., 2006b]. As mentioned in sec. 4.3 a list of run (58) in which the source position has an offset smaller than 2.0° from the pointing position was used. Usually a *bgrange* of 2.0° is set to avoid regions in which the system acceptance suffers a significant energy dependence, declining rapidly at low energies (see Fig. 3.2), so that low energy events are poorly detected. However, besides this one value, since the number of observations is not extremely large, a *bgrange* of 2.5° was also used in order to avoid the rejection of too many runs, due to the analysis requirement that the On-region must lie completely inside the *bgrange*. The energy spectrum was then fit with a power-law $dN/dE = F_0 E^{-\Gamma}$. In table 4.3 the results are shown. As it would be expected, they are in very good agreement among themselves. A slightly hardening is present with respect to the published data, but the values are still consistent within the error bars. A significant reduction is instead apparent in the case of the flux and also a worsening of the $\chi^2$ is clearly visible. These discrepancies could be partly explained by the wider energy range on which the spectra were fit in this work.

**Table 4.3.** Results of the spectral analysis on the entire source. The values are derived for 2.0° and 2.5° *bgrange*.

| | | Flux > 200 GeV | | | |
|---|---|---|---|---|---|
| | $\Gamma$ | $(10^{-12} cm^{-1} s^{-1})$ | $\theta$ cut | $\chi^2$/do | Fit range |
| New results | 2.62±0.06 | 44.1±3.62 | 0.36 | 18.11/8 | 0.21 - 30.1 TeV |
| | 2.62±0.06 | 44.04±3.37 | 0.36 | 12.94/8 | 0.21 - 30.1 TeV |
| [Aharonian et al., 2006b] | 2.72±0.06 | 53.2±2.0 | 0.36 | 6.9/11 | 0.2-10 TeV |
| [Higashi et al., 2008] | 2.69±0.30 | 5.0±1.5† | 0.41 | -/4 | 0.6-2 TeV |

† This value is calculated for an energy range 0.6-2 TeV

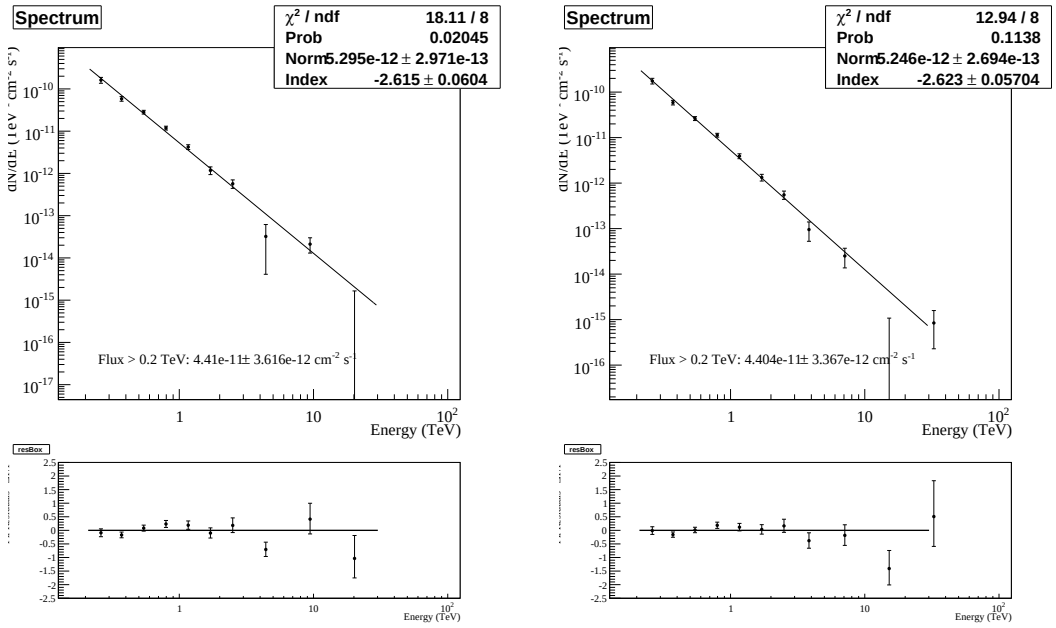


(a) (b)

**Fig. 4.7.** Spectra (top) and residuals (bottom) for the analysis with *bgrange*=2.0° (a) and 2.5° (b). Looking at the residuals, some kind of curvature in the spectrum seems to be present.

## 4.7 Spatially resolved spectral analysis

The central part of this work was to perform a spatially resolved spectral analysis, in order to look for possible gradients in the energy spectrum. The idea at the basis is that the spectrum should get harder in the proximity of the source injector and softer with increasing distance from it. In the presence of a significant gradient hence it could be possible to identify the counterpart among the known objects or at least the region in which to look for it if nothing has been yet detected there.

To perform such an analysis the source is divided into smaller subregions. In each of these the statistic must be sufficiently large in order to yield results that are not dominated by the error. Therefore, since the dataset chosen (2.0° list) is not extremely large, all the available runs must be used. Moreover, a common runlist for each region has to be used, to prevent differences in the results that could arise from the use of different datasets.

For the particular dataset of HESS J1804-216, in which almost all runs are survey observations and not dedicated observations, it is not possible to fulfill these requests using the standard Region Background Method for the evaluation of the background. This is due to the fact that survey observations are made "blindly" and provide therefore a large set of different offsets. This disadvantage respect to the wobble method becomes dramatic for a spatially resolved analysis, where a bunch of test positions are used, each creating its own set of offsets, with the consequence that each subregion has its own subset of runs fulfilling the request of the On-region lieing completely inside the *bgrange*. It is therefore not possible to have a common run-list for each subregion even for a *bgrange*=2.5° without rejecting a consistent number of runs. Another thing

that could give rise to some kind of problems is the fact that the number of Off-regions varies for each run in a range from 2 up to 20, affecting therefore the normalization of the background.

Considered all these remarks, it would be convenient to use a different background estimation rather than the Region Background Method. A possibility would be to use OFF-runs, but there are no dedicated ones like in the ON-OFF observation method, and the search for suitable ones is difficult and not always satisfactory and/or successful. Moreover just one Off-region per run would be used, so that statistical fluctuation in the background could become important. Therefore another method has to be found.

Finding an alternative to the standard Region Background Method for the background estimation would be interesting also for the spectral analysis of an entire extended source like HESS J1804-216. Indeed, if no wobble or ON-OFF observations (sec. 2.3) are available, there are difficulties in finding regions for the evaluation of the background that have the same size as the On-region and are confined in a ring around the camera center, since their number is determined by the run-offset and is affected by the presence of other extended sources in the neighborhood.

The Ring Background Method was chosen as possible alternative, although it would need energy corrections that are actually not performed. Nevertheless one could expect that the error on the energy averages out on the whole ring surface, becoming consequently not so important and causing just a constant shift in the spectral index. When looking for gradients this is not really important, since what really interests is the variation of the spectral index and not its absolute value. A big advantage of the Ring Background Method would be instead the fact that it is able to estimate the background for every point in the sky, avoiding the rejection of runs and increasing therefore the statistic. Furthermore the background relative to an On-region would be evaluated in the same region of the sky near the On-region for each run, on the contrary of the

**Table 4.4.** Differences between Ring and Region Background Methods.

| RegionBg | | RingBg | |
|---|---|---|---|
| Advantages | Disadvantages | Advantages | Disdvantages |
| Same acceptance for On- and Off-events, no need of energy corrections | | | Different acceptance for On- and Off-events, energy correction needed |
| | Different numbers of Off-regions in different regions of the sky ($2< N_{Off} <20$) | Same Off-region for all runs, near the On-region | |
| | Possibility to suffer large gradients in the background | Gradients in the background are more under control | |
| | Rejection of many runs | All runs are taken into account | |

Region Background Method for which it is estimated in different parts of the sky for each run. The spatial vicinity of On- and Off-region reduces also the probability to suffer large gradients in the background due to the background itself or to the telescope system. In Table 4.4 the differences between the two methods are summarized.

To estimate the quality of the Ring Background Method (from now on referred to as RingBg) systematic studies and comparisons with the Region Background Method (from now on referred to as RegionBg) were performed (sec. 4.7.1).

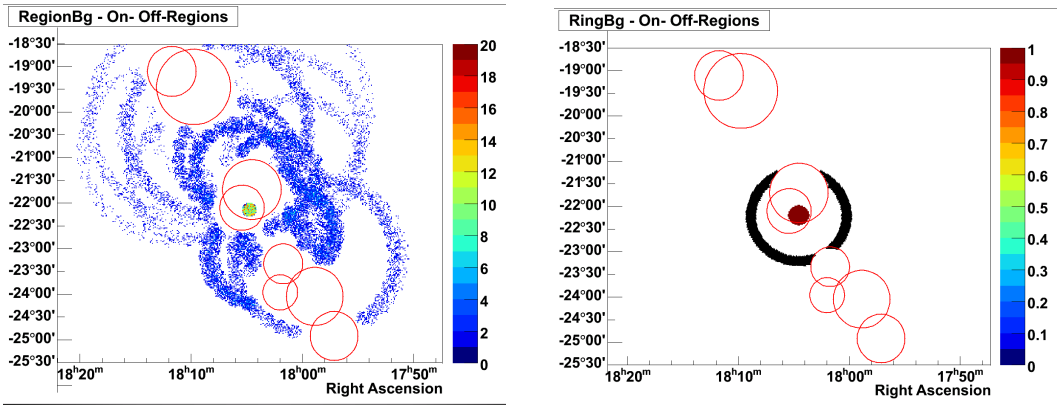


(a) (b)

**Fig. 4.8.** Example of the background estimation for Region (left) and Ring (right) Background Methods for a real analysis.

To perform the spatially resolved spectral analysis the three different mapping models shown in Fig. 4.9 were used. In all three cases the subregions are circles of radius $\theta = 0.15°$ and were chosen so that they provide enough statistic to obtain not too large errors. In Model C the circles are slightly overlapping and arranged in a way that the most of the emission is covered, in Model A they are disposed on a grid centered on the most probable counterpart PSR B1800-21 and in Model B on the same grid shifted to south-east so that PSR B1800-21 is in the middle of four subregions. The relative small number of the subregions is due to the fact that besides these positions the statistic is not sufficient.

### 4.7.1 Systematic studies

For the systematic studies the mapping Model C was used. Several analysis were performed changing the *ring-radius* (0.85°, 1.0° and 1.2°) and the *bgrange* (2.0°, 2.5° and 3.3°). The choice of these values has different reasons. For the *ring-radius* the value of 0.85° was chosen to be the smallest possible taking into account the size of HESS J1804-216, so that the ring relative to each subregion is not too much affected by its exclusion region. The values 1.0° and 1.2° are almost a direct consequence of the first one taking into account the fact that the rings must not overlap and that the background has to be estimated under rather different conditions in order to test if the method is solid for a spectral analysis. For the *bgrange* the value of 2.0° was chosen as it is the typical value used for the spectral analysis, 2.5° to avoid runs rejection due to the fact that

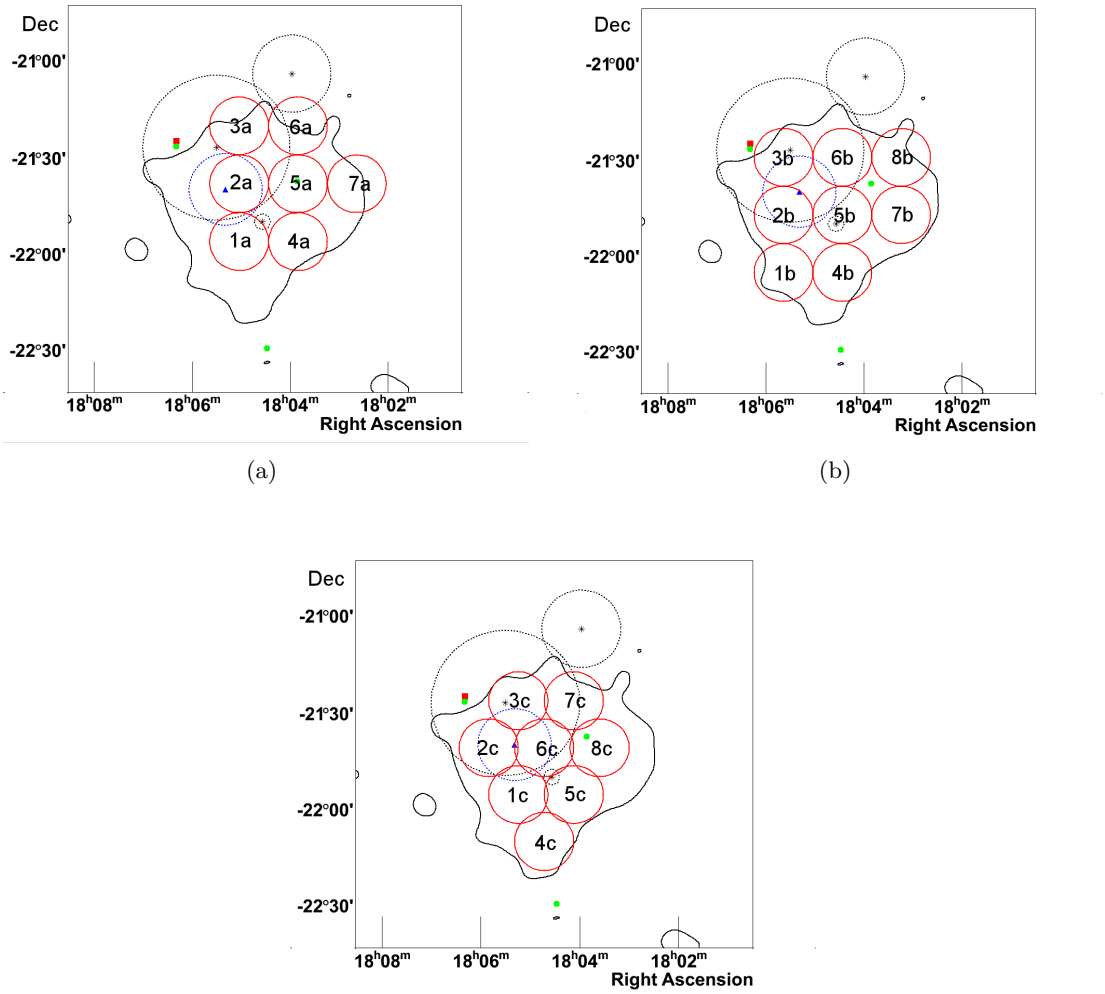


**Fig. 4.9.** The three mapping models used in the work. (a), (b), (c) are the Model A, B and C respectively. The black contours lines are the 20 counts contour lines of Fig. 4.6. Also shown in the pictures are the positions and dimensions of some of the possible counterparts mentioned at the beginning of the chapter. The big circle on the north-east part is SNR G8.7-0.1. SNR G8.31-0.09 is the small circle almost in the center of the emission region. SNR G8.90+0.40 is the circle on the north-west part. The green spots are the three mentioned pulsars: in the middle is PRS B1800-21, on the south PSR J1804-2228 and on the north-east part PSR J1806-2125. The blue triangle represents the emission detected by FERMI and the blue circle the 95% error on the position. The red square is the Maser OH(1720 MHz).

the On-region is not completely contained within the *bgrange* itself and 3.3° in order to take into account a complete ring also in the case of a large offset of the On-region. The importance of taking into account a complete ring, even if it requires to go to extreme large offsets, is that in this way every position in the ring is balanced from another one on the opposite side of the ring.

It must be noted that in the case of a RegionBg analysis some runs are rejected also for a *bgrange* of 2.5° because of the impossibility of finding at least one Off-region. A *bgrange* of 3.3° is not needed in the case of RegionBg since all the On-regions (and hence the Off-regions) are already completely contained within 2.5°.

As first, a comparison between the results obtained from the RegionBg and RingBg analysis taking into account exactly the same runs was performed. Since the RegionBg accepts in general less runs than the RingBg, two other runlists (one for *bgrange*=2.0°, one for *bgrange*=2.5°) had to be made starting from the 2.0°-runlist described in sec. 4.3. These new lists contain only the runs accepted and analysed by the RegionBg. As every subregion has a different set of offsets and therefore its own subset of rejected runs, new runlists were made for each subregion. The analysis were then performed for both *bgrange*, using in the case of the RingBg analysis a *ring-radius* of 0.85°. After that a series of RingBg analysis with different combinations of *ring-radius* and *bgrange* were done using the usual 2.0°-runlist for each subregion. It is necessary to remember that for *bgrange*=2.0° some runs are rejected depending on the subregion, so that no common runlist exists for all the subregions. In all the cases the spectra were fit with a power-law in an energy range between 0.21 and 15.4 TeV. The comparison of the spectral indexes is shown in Fig. 4.10 for the analysis with the same dataset and in Fig. 4.12 for the other RingBg analysis. The correspondent comparisons of the fluxes is shown in Fig. 4.11 and 4.13.

From Fig. 4.10 and 4.11 it is apparent that the results for both spectral index and flux calculated with the RegionBg analysis do not depend on the *bgrange* used. The values are indeed almost all completely coincident between the two analysis and where not they are however well inside the $1\sigma$ error. This means that the RegionBg is able to derive correct values (or at least consistent among themselves) also using runlists with significant different amount of statistic and that it is not affected appreciably by the deteriorating of the system acceptance between 2.0° and 2.5°. About the RingBg results, one can see that the values of the spectral indexes are consistent among the two RingBg analysis and also with those of the RegionBg analysis. The only exceptions are region 3 and 7. This could be due to the combination of their large mean offset and low statistic. Looking at the fluxes, it can be immediately noted that the RingBg values are systematically lower with respect to the RegionBg ones and that probably a *bgrange* dependence is present.

The results of the systematic RingBg analysis (Fig. 4.12 and 4.13) substantially confirm what is seen in the comparison between the RegionBg and RingBg analysis with the same runlist. The RingBg values of the spectral indexes are consistent well within the $1\sigma$ error bar, almost coincident in most of the cases. The most differences are found between analysis that accept a different number of runs and in regions with low statistic, thing that makes the spectral fit be more subject to fluctuations. The comparison of RingBg and RegionBg analysis shows also in this case that the values are consistent in the limit of $1\sigma$ error, even if a shift towards harder spectra

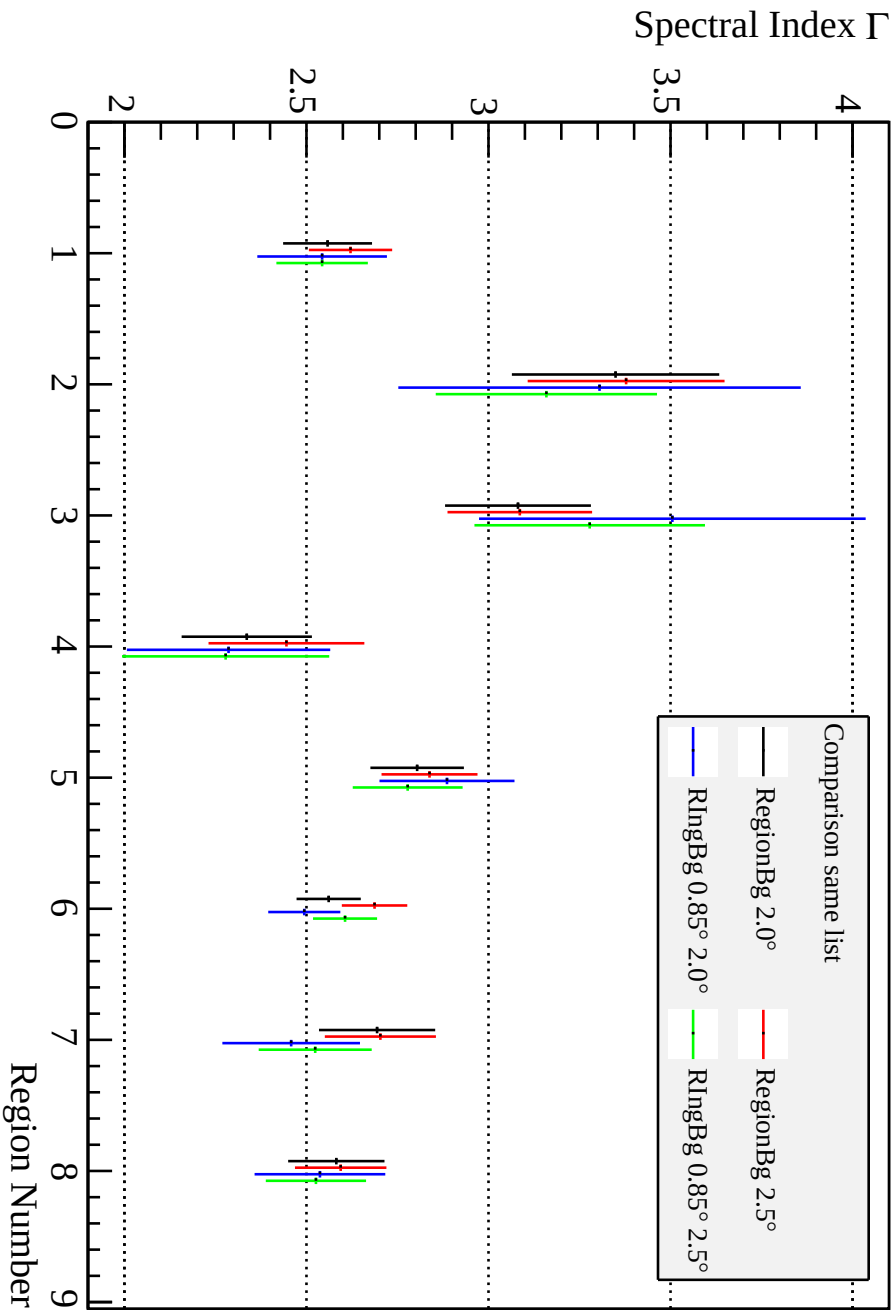


**Fig. 4.10.** Comparison Gamma values for RegionBg and RingBg, same runlist.

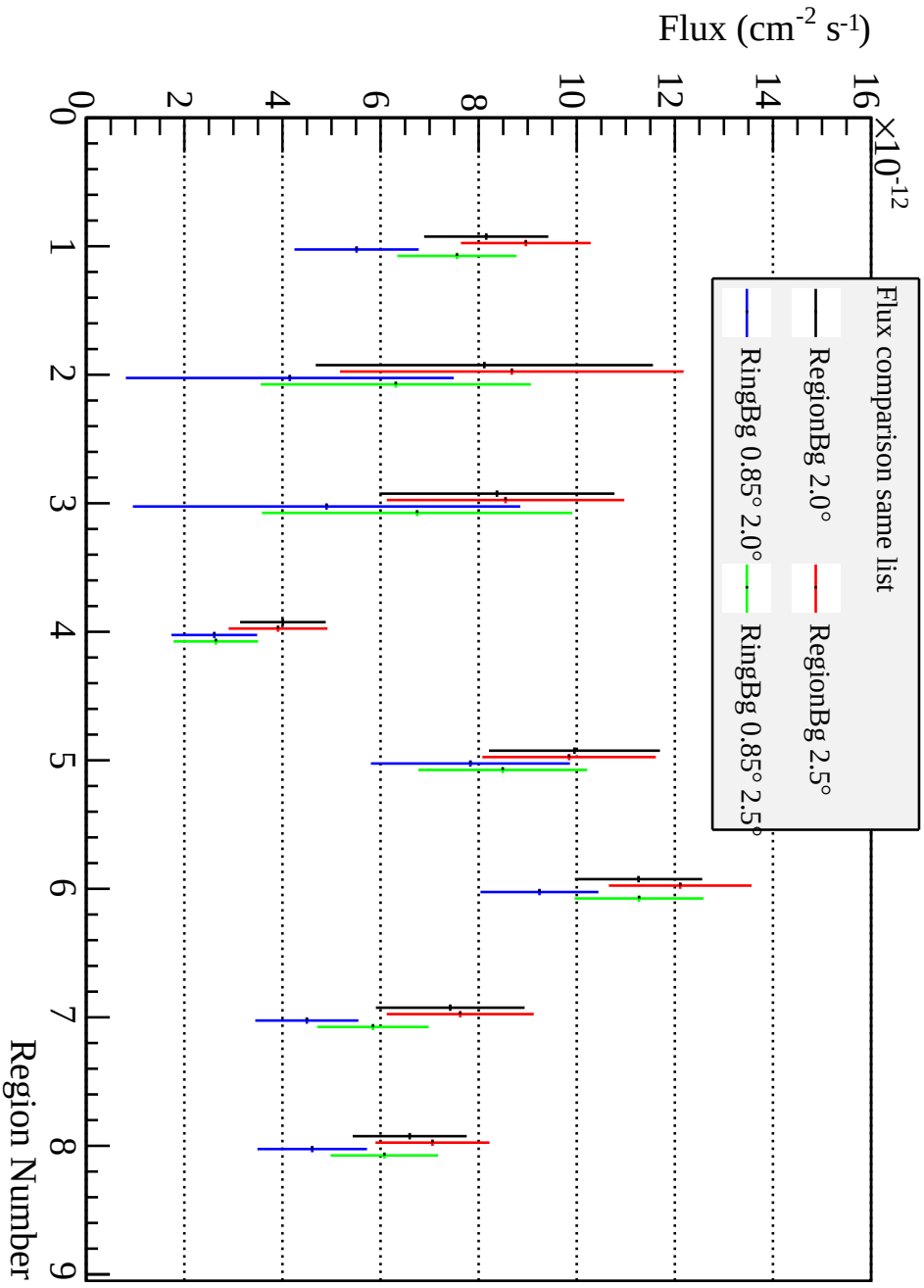


**Fig. 4.11.** Comparison Flux values for RegionBg and RingBg, same runlist.

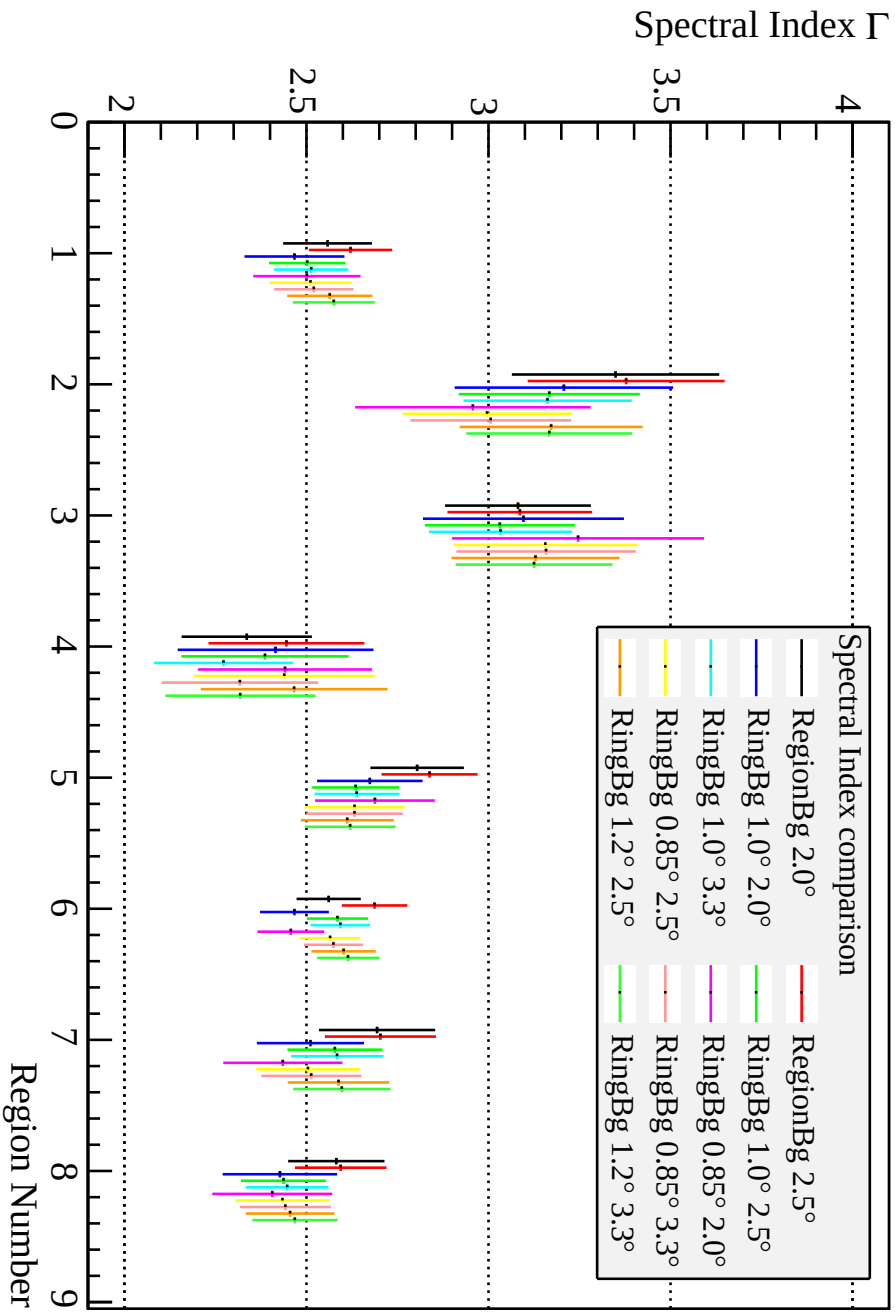


**Fig. 4.12.** Comparison Gamma values for RingBg with different parameters.

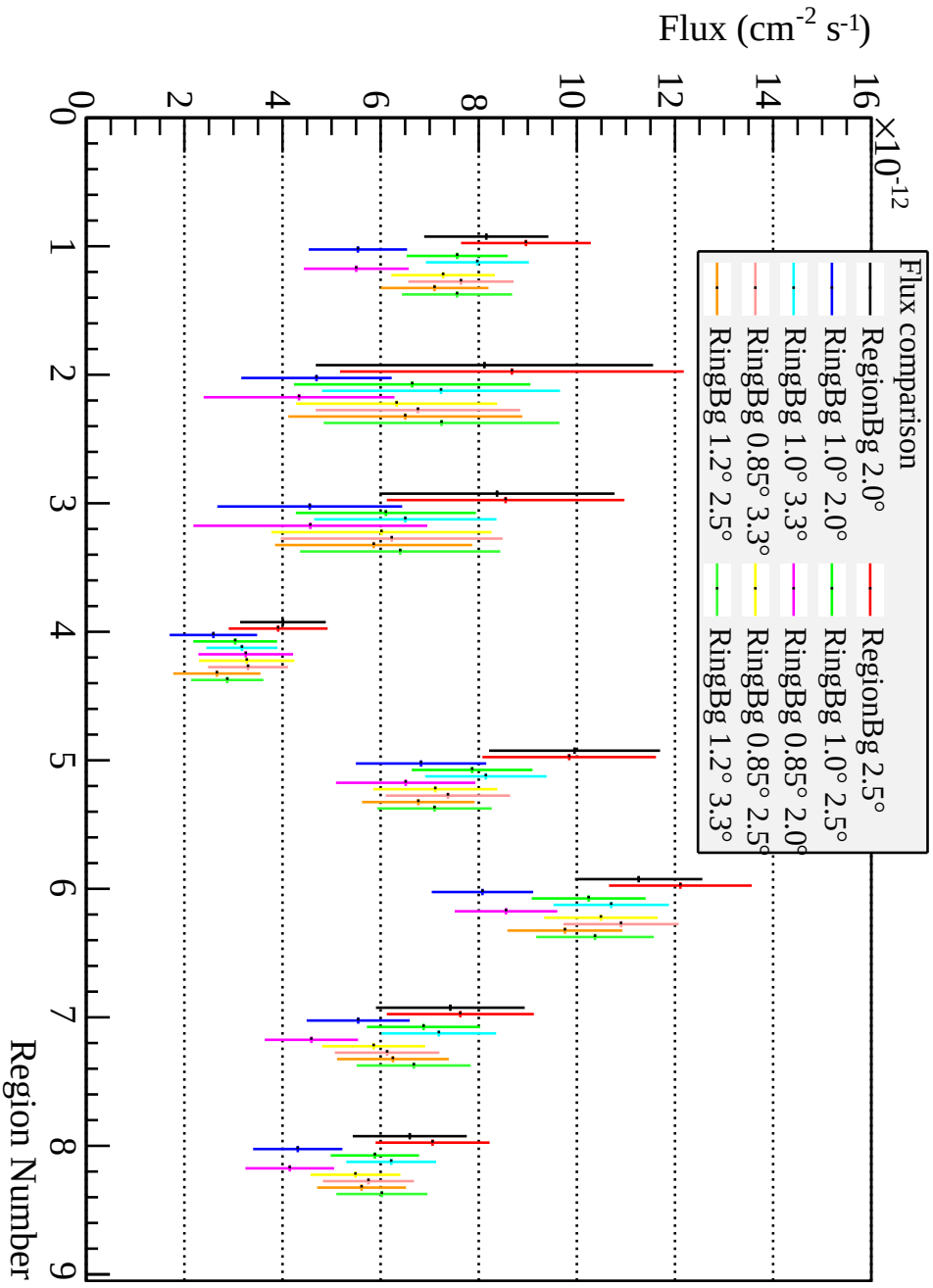


**Fig. 4.13.** Comparison Flux values for RingBg with different parameters.

is apparent in some regions. Such shift is however not constant and not present in all regions, so that it is not possible to quantify an overall difference between the two methods of analysis.

With regard to the flux, the RegionBg values are constantly larger than the RingBg values over each region. This is clearly visible comparing the analysis with the same *bgrange*. In most of the cases the values are barely consistent in the limit of the $1\sigma$ error, even if the error bars are rather large. Moreover also the dependence of the RingBg results from the *bgrange* is visible. Again, the large error bars cover this effect, nevertheless, for all the three *ring-radius* used, the flux increases with increasing *bgrange*. It is likely that this trend is due to the way the background is estimated in the RingBg. In fact, taking into account different *bgrange* means also taking into account different Off-areas $A_{Off}$. For runs in which the sum of run-offset and *ringradius* is larger than the *bgrange* not the entire ring is used to estimate the background. Therefore, the larger is the *bgrange*, the larger is also the part of the ring used. But, as already said, the acceptance gets smaller with increasing offset and less $\gamma$-like events are detected. This means in the end that the ratio $N_{Off}/A_{Off}$ becomes in average smaller with increasing *bgrange*, while $N_{On}/A_{On}$ remains always the same, so that the excess becomes bigger and the flux as well.

At this point some considerations on the use of the RingBg for the spectral analysis can be done:

- looking at the values of the spectral indexes, they are consistent among themselves and seem in good agreement with those derived by the standard RegionBg, within the $1\sigma$ error. Therefore, if probably not indicated for the evaluation of the real spectral index, it seems that the RingBg can be however used to look for variations of the spectrum on the emission region.

- looking at the flux values instead, a inconsistency can be found both between the two background estimation methods and between the RingBg analysis performed with different parameters. In this last case, if the reasoning made above is correct, the inconsistency would get even worse with the increase of the statistic, since the error on the flux would decrease. The RingBg is therefore not appropriate for the estimation of the flux.

- the fact that the flux is constantly lower for the RingBg means that either too much background is subtracted with this estimation method or too few by the other one. Since, how it has been shown, the flux of the RingBg depends on the *bgrange* it is likely that the first hypothesis is the correct one. At this point, the reasonable hope of increasing the statistic by taking into account a larger number of runs using the RingBg clearly vanishes, even if it remains the advantage of having a common runlist for all the subregions.

- an excessive background subtraction could maybe explain the harder spectra calculated by the RingBg. Indeed, since the background spectrum at lower energies is softer than at higher energies, the subtraction of an overestimated background would change the shape of the source spectrum, making it harder, since the larger statistic at lower energies has a higher weight in the fit.

- Another sign in support of the last two point is that the errors on the RingBg values are always comparable (if not even larger) with those of the RegionBg. Exactly the contrary of what should happen in presence of a significant larger statistic.

Considered all these remarks it is apparent that the energy dependence of the acceptance is not the only problem that affects the RingBg in performing a spectral analysis. The overestimation of the background must indeed be taken into consideration and its implications studied deeper. Currently the RingBg seems hence not to be appropriate for the spectral analysis. Nevertheless, similar systematic studies performed on other sources taking into account different ranges of parameters could help to find out if the differences are random or if there is actually a systematic that could be quantified, so that it would be possible to pass from one background estimation method to the other simply applying a numerical correction to the results.

### 4.7.2 Results from the mapping models

The results obtained for the systematic analysis can clearly be used also to comment the differences in the spectral indexes between the different subregions. Since the analysis relative to the mapping models A and B were performed only with the RegionBg, and since the RingBg has shown no real improvement with respect to the standard method, then only the RegionBg results are used here for the mapping model C. In Fig. 4.14 the values of the spectral index relative to RegionBg analysis with *bgrange* 2.0° and 2.5° are plotted for each subregion of the three mapping models. In Fig. 4.15 the correspondent flux values are shown. The colormaps relative to *bgrange*=2.5° are then shown in Fig. 4.16.

- **Model A**: it is clearly visible that the subregion centered on PSR B1800-21 (#5a) has a significantly harder spectrum with respect to all the other regions, maybe with the exception of subregion #1a.

- **Model B**: a rather soft spectrum is present in the eastern part of the HESS J1804-216. The four subregions around PRS B1800-21 show a similar spectral index, with a hardening towards the center of the emission region (subregion #5b). The southern subregion #4b shows a spectrum probably harder than one would expect, since it lies at the edge of HESS J1804-216. However it is not very significant because of the large error bars.

- **Model C**: two really soft subregions (#2c and #3c) are present in the north-east part of HESS J1804-216, beyond the bow-shaped structure in the center of the source, that could be associated with SNR G8.7-0.1. The spectrum has almost the same value in the three subregions crossed by this bow-shaped structure (#1c, #6c and #7c) and in the one that contains PSR B1800-21 (#8c), showing maybe a small softening in subregion #7c. Again a rather hard subregion is found in the southern part of HESS J1804-216 (#4c). It is interesting to note that this hard region is separated from the other hard ones by the subregion #5c, that is instead rather soft, suggesting hence the presence of more than one counterpart for HESS J1804-216.

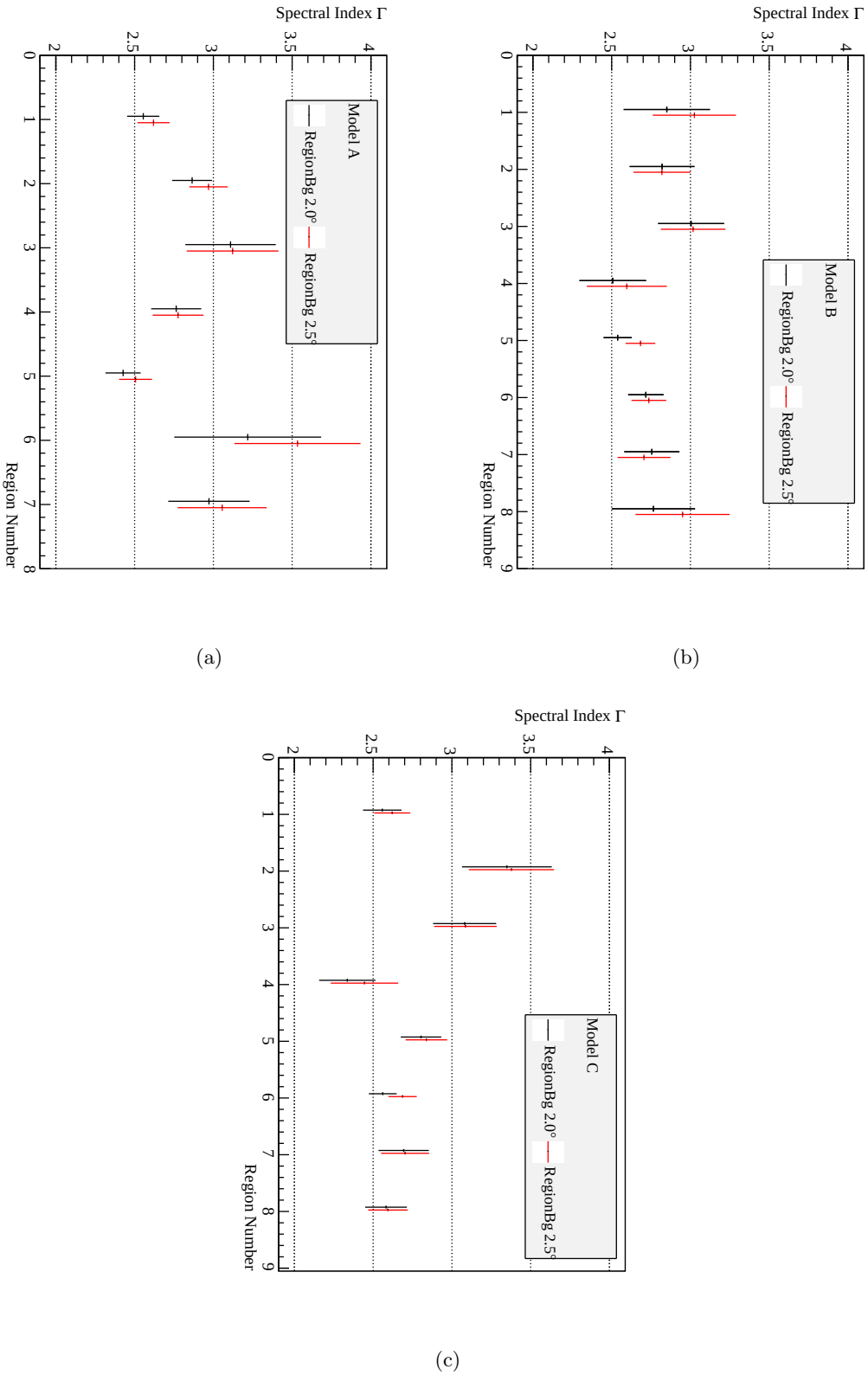


(a) (b)

(c)

**Fig. 4.14.** Spectral indexes relative to RegionBg analysis with *bgrange* 2.0° and 2.5° for **(a)** Model A, **(b)** Model B and **(c)** Model C.

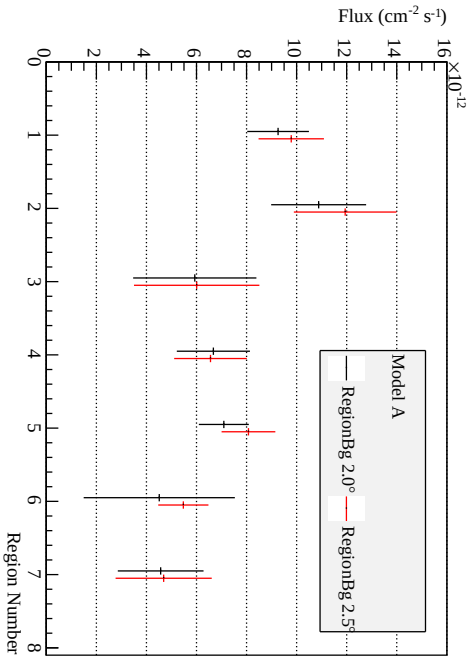


(a)

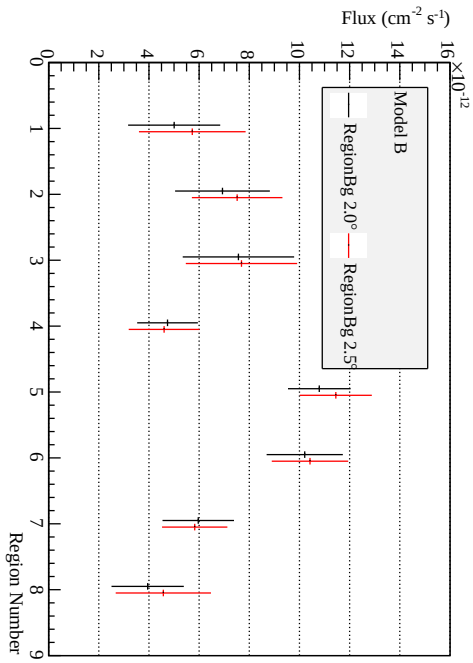


(b)

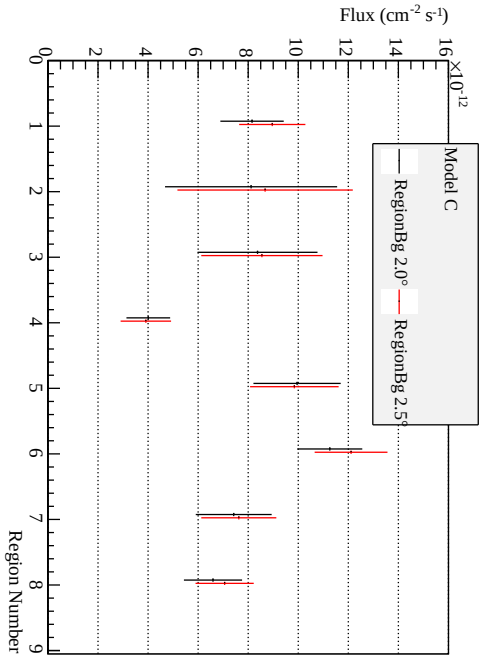


(c)

**Fig. 4.15.** Flux values relative to RegionBg analysis with *bgrange* 2.0° and 2.5° for **(a)** Model A, **(b)** Model B and **(c)** Model C.

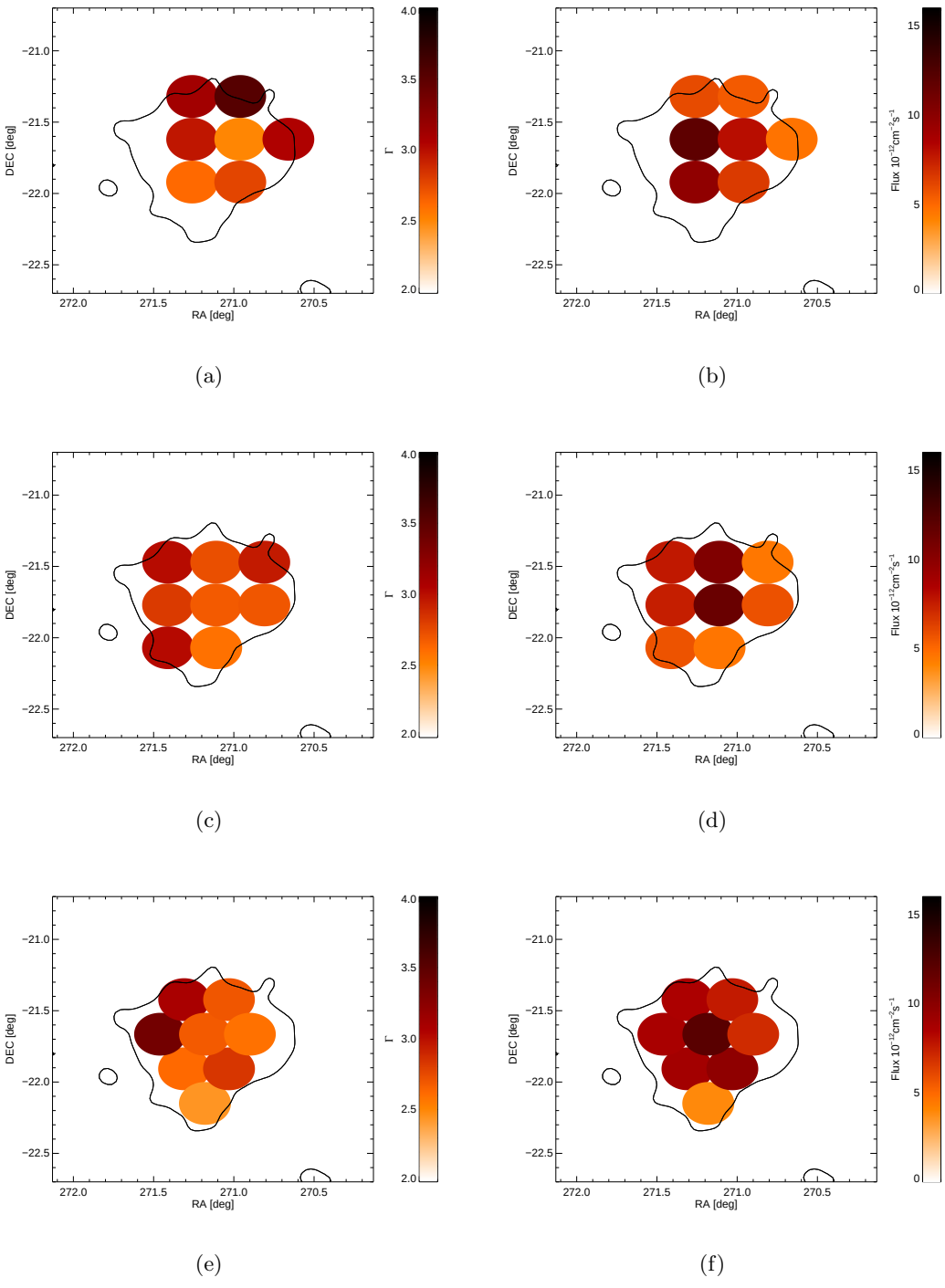


**Fig. 4.16.** Colormaps for RegionBg analysis with *bgrange*=2.5°. (a) and (b) Model A, (c) and (d) Model B, (e) and (f) Model C. On the left the maps relative to the Spectral Index are shown, on the right to the Flux.

Taking into account all the considerations made above about the results of three mapping models, a general comment about the nature of HESS J1804-216 can be summarized:

- although a clear identification as actual counterpart is not possible, it is likely that PSR B1800-21 contributes to the TeV emission of HESS J1804-216. The spectrum becomes indeed harder towards its position;

- it is also possible that SNR G8.7-0.1 is physically associated with the TeV source because the bow-shaped structure in the middle of HESS 1804-216 follows the shape of the SNR radio emission (see Fig. 4.2) and the spectrum becomes softer beyond it;

- as it could be expected, the spectrum gets softer towards the edges of the emission region. However this is not true for the southern region, where a rather hard spectrum is found, on and beyond the bow-shaped structure visible under SNR G8.31-0.09 that follows the shape of the radio emission detected on the region (see Fig. 4.2). However, from these analysis it is not possible to exclude or confirm SNR G8.31-0.09 as counterpart;

- since the spectrum near the centroid position of HESS J1804-216 is not particularly hard, the two sources Suzaku J1804-2142 (Src1) and Suzaku J1804-2140 (Src2) (detected also by Chandra) are not likely to be considered as actual counterparts;

- due to their positions or to the softening of the spectrum towards the edges of HESS J1804-216, the other mentioned objects (PSR J1806-21, PSR J1804-2228 and SNR G8.90+0.40) are not likely to be considered as counterparts.

In conclusion, if the considerations made above are correct, it is most probable that HESS J1804-216 has not only one counterpart, but is associated with several objects, showing a multiple nature.

# 5

# Conclusions

In this work it has been presented the analysis performed on the galactic Very High Energy TeV source HESS J1804-216, discovered during the 2004-2005 Galactic Plane Survey in the inner part of the Galactic Plane by the H.E.S.S. Cherenkov Telescope.

This work is substantially divided in two parts. In the first one the theory of all the processes that permit the VHE $\gamma$-ray emission and the Cherenkov emission visible by the telescope are described, as well as the HESS telescope system, the data collection, the event reconstruction and the data analysis performed by the software.

In the second part the actual analysis of HESS J1804-216 was presented. Standard morphological and spectral analysis were first performed. Their results are in agreement with the data published in [Aharonian et al., 2006b] in the case of the spectral analysis and are slightly improved in the case of the morphological analysis. After that, a spatially resolved spectral analysis was also performed dividing the source emission region into smaller subregions after three different mapping models. The use of the Ring Background Method as an alternative to the standard Region Background Method for this kind of analysis was suggested. The reason was try to overcome some disadvantages of the standard method, especially in relation to the particular dataset available for HESS J1804-216. Systematic studies were therefore carried out in order to proof the consistency of this alternative method. The results were not particularly satisfactory, since, besides the known need of an energy correction, the Ring Background Method showed other intrinsic problematics and no significant improvement with respect to the Region Background Method. The analysis on the three mapping models were therefore performed using the standard Region Background Method.

What can be inferred from the results is that the two possible counterparts suggested in [Aharonian et al., 2006b] (SNR G8.7-0.1 and PSR B1800-21) are most likely physically associated to HESS J1804-216, and in the case of the pulsar a contribution to the TeV emission is surely given. Other objects detected well within the emission region in X-rays by Suzaku, Chandra and Swift do not seem to be associated with HESS J1804-216, while in the case of the supernova remnant detected at radio wavelength nothing can be said after this analysis.

Although the results obtained in this work are sufficient to give indications about a possible composite nature of HESS J1804-216 and show clearly a complex morphological structure, more and dedicated observations are needed, since the statistic is still insufficient to perform a spa-

tially resolved spectral analysis that provides significantly small error bars. Moreover, the Region Background Method shows some important disadvantages in the case of a dataset consisting in survey observations with large offsets. As showed in the work, the suggested alternative does not provide improvements with respect to the standard method, rather could show more important problematics. Nevertheless, other deep systematic studies would help to understand if its utilization is possible or completely to avoid.

# References


A. A. Abdo et al. Fermi Large Area Telescope Bright Gamma-ray Source List. *ArXiv e-prints*, 2009.

F. Aharonian and A. M. Atoyan. Broad-band diffuse gamma ray emission of the galactic disk. *Astronomy and Astrophysics*, 362:937–952, 2000.

F. Aharonian et al. A New Population of Very High Energy Gamma-Ray Sources in the Milky Way. *Science*, 307:1938–1942, 2005a.

F. Aharonian et al. H.E.S.S. observations of PKS 2155-304. *Astronomy and Astrophysics*, 430: 865–875, 2005b.

F. Aharonian et al. Observations of the Crab nebula with HESS. *Astronomy and Astrophysics*, 457:899–915, 2006a.

F. Aharonian et al. The H.E.S.S. Survey of the Inner Galaxy in Very High Energy Gamma Rays. *Astrophysical Journal*, 636:777–797, 2006b.

F. Aharonian et al. Energy dependent $\gamma$-ray morphology in the pulsar wind nebula HESS J1825-137. *Astronomy and Astrophysics*, 460:365–374, 2006c.

F. Aharonian et al. HESS very-high-energy gamma-ray sources without identified counterparts. *Astronomy and Astrophysics*, 477:353–363, 2008.

APOD. `http://apod.nasa.gov/apod/`, 2009.

A. Bamba et al. Discovery of a Possible X-Ray Counterpart to HESS J1804-216. *Publ. Astronomical Society of Japan*, 59:209–214, 2007.

A. R. Bell. The acceleration of cosmic rays in shock fronts. I. *Monthly Notices of the Royal Astronomical Society*, 182:147–156, 1978.

D. Berge. *A detailed study of the gamma-ray supernova remnant RX J1713.7-3946 with H.E.S.S.* PhD thesis, Ruprecht-Karls-Universität Heidelberg, Germany, 2006.

K. Bernlöhr. Monte Carlo images of air showers. `https://www.mpi-hd.mpg.de/hfm/~bernlohr/HESS/`, 2000.

K. Bernlöhr. CORSIKA and sim_hessarray. Simulation of the imaging atmospheric Cherenkov technique for the H.E.S.S. experiment. HESS internal note 02/04, 2002.

K. Bernlöhr et al. The optical system of the H.E.S.S. imaging atmospheric Cherenkov telescopes. Part I: layout and components of the system. *Astroparticle Physics*, 20:111–128, 2003.

R. Blandford and D. Eichler. Particle Acceleration at Astrophysical Shocks - a Theory of Cosmic-Ray Origin. *Physics Reports*, 154, 1987.

G. R. Blumenthal and R. J. Gould. Bremsstrahlung, Synchrotron Radiation, and Compton Scattering of High-Energy Electrons Traversing Dilute Gases. *Reviews of Modern Physics*, 42: 237–271, 1970.

W. F. Brisken, M. Carrillo-Barragán, S. Kurtz, and J. P. Finley. Proper Motion of Pulsar B1800-21. *Astrophysical Journal*, 652:554–558, 2006.

C. L. Brogan et al. Discovery of 35 New Supernova Remnants in the Inner Galaxy. *Astrophysical Journal Letters*, 639:L25–L29, 2006.

E. Cappellaro. The rate of supernovae. *Memorie della Societa Astronomica Italiana*, 72:863–866, 2001.

T. R. Clifton and A. G. Lyne. High-radio-frequency survey for young and millisecond pulsars. *Nature*, 320:43–45, 1986.

R. Cornils et al. The optical system of the H.E.S.S. imaging atmospheric Cherenkov telescopes. Part II: mirror alignment and point spread function. *Astroparticle Physics*, 20:129–143, 2003.

W. Cui and A. Konopelko. Chandra View of the Unidentified TeV Gamma-Ray Source HESS J1804-216. *Astrophysical Journal Letters*, 652:L109–L112, 2006.

A. Daum et al. First results on the performance of the HEGRA IACT array. *Astroparticle Physics*, 8:1–2, 1997.

J.M. Davies and E.S. Cotton. Design of the quartermaster solar furnace. *J. Solar Energy Sci. Eng.*, 1:16, 1957.

O. C. de Jager and A. Djannati-Ataï. Implications of H.E.S.S. observations of pulsar wind nebulae. *ArXiv e-prints*, 2008.

M. Fatuzzo, F. Melia, and R. M. Crocker. High-Energy Activity in the Unusually Soft TeV Source HESS J1804-216 toward the Galactic Center. *ArXiv Astrophysics e-prints*, 2006.

J. P. Finley and H. Ögelman. The PSR 1800-21/G8.7-0.1 association: A view from ROSAT. *Astrophysical Journal Letters*, 434:L25–L28, 1994.

S. Funk. *A new population of very high-energy $\gamma$-ray sources detected with H.E.S.S. in the inner part of the Milky Way.* PhD thesis, Ruprecht-Karls-Universität Heidelberg, Germany, 2005.

S. Funk et al. The trigger system of the H.E.S.S. telescope array. *Astroparticle Physics*, 22: 285–296, 2004.

B. M. Gaensler and P. O. Slane. The Evolution and Structure of Pulsar Wind Nebulae. *Annual Review of Astronomy and Astrophysics*, 44:17–47, 2006.

D. Heck et al. *CORSIKA: a Monte Carlo code to simulate extensive air showers.* 1998.

W. Heitler. *Quantum theory of radiation.* Oxford University Press, 1954.

HESS Collaboration. HESS software code.

HESS website. `http://www.mpi-hd.mpg.de/hfm/HESS/`, 2009.

J. W. Hewitt and F. Yusef-Zadeh. Discovery of New Interacting Supernova Remnants in the Inner Galaxy. *Astrophysical Journal Letters*, 694:L16–L20, 2009.

Y. Higashi et al. Observation of Very High Energy Gamma Rays from HESS J1804-216 with CANGAROO-III Telescopes. *Astrophysical Journal*, 683:957–966, 2008.

A. M. Hillas. Cerenkov light images of EAS produced by primary gamma. In F.C. Jones, editor, *International Cosmic Ray Conference*, volume 3 of *International Cosmic Ray Conference*, pages 445–448, 1985.

J. A. Hinton. The status of the HESS project. *New Astronomy Review*, 48:331–337, 2004.

J. A. Hinton, D. Berge, and S. Funk. Background Modeling in Ground Based Cherenkov Astronomy, 2005.

G. Hobbs et al. A very large glitch in PSR J1806-2125. *Monthly Notices of the Royal Astronomical Society*, 333:L7–L10, 2002.

S. Hoppe. *Emitters of VHE $\gamma$-radiation as revealed by the H.E.S.S. Galactic plane survey.* PhD thesis, Ruprecht-Karls-Universität Heidelberg, Germany, 2008.

O. Kargaltsev, G. G. Pavlov, and G. P. Garmire. X-Ray Emission from PSR B1800-21, Its Wind Nebula, and Similar Systems. *Astrophysical Journal*, 660:1413–1423, 2007a.

O. Kargaltsev, G. G. Pavlov, and G. P. Garmire. The Field of the TeV Source HESS J1804-216 in X-Rays and Other Wavelengths. *Astrophysical Journal*, 670:643–654, 2007b.

N. E. Kassim and K. W. Weiler. A possible new association of a pulsar with a supernova remnant. *Nature*, 343:146–148, 1990a.

N. E. Kassim and K. W. Weiler. W30 revealed - Separation and analysis of thermal and nonthermal emission in a Galactic complex. *Astrophysical Journal*, 360:184–196, 1990b.

H. Kubo et al. Status of the CANGAROOIII project. *New Astronomy Review*, 48:323–329, 2004.

R. Landi et al. Swift XRT Follow-up Observations of TeV Sources of the HESS Inner Galaxy Survey. *Astrophysical Journal*, 651:190–196, 2006.

T.-P. Li and Y.-Q. Ma. Analysis methods for results in gammaray astronomy. *Astrophysical Journal*, 272:317–324, 1983.

M. S. Longair. *High energy astrophysics. Vol.1: Particles, photons and their detection.* Cambridge University Press, 1992.

M. S. Longair. *High energy astrophysics. Vol.2: Stars, the galaxy and the interstellar medium.* Cambridge University Press, 1994.

E. Lorenz. Status of the 17 m MAGIC telescope. *New Astronomy Review*, 48:339–344, 2004.

D. J. Morris et al. The Parkes Multibeam Pulsar Survey - II. Discovery and timing of 120 pulsars. *Monthly Notices of the Royal Astronomical Society*, 335:275–290, 2002.

N. Odegard. 57.5 MHz observations of extended nonthermal sources in the galactic plane. *Astronomical Journal*, 92:1372–1380, 1986.

P. Ojeda-May et al. Massive Star Formation Near the Supernova Remnant W30. *Revista Mexicana de Astronomia y Astrofisica*, 38:111–118, 2002.

G. G. Pavlov, D. Sanwal, and V. E. Zavlin. The Pulsar Wind Nebula of the Geminga Pulsar. *Astrophysical Journal*, 643:1146–1150, 2006.

D. H. Perkins. *Introduction to high energy physics.* Addison-Wesley Publishing Company, 1972.

D. H. Perkins. *Particle astrophysics.* Oxford University Press, 2003.

M. Pohl. *Einführung in die Hochenergieastrophysik.* Shaker-Verlag, 2002.

G. B. Rybicki and A. P. Lightman. *Radiative processes in astrophysics.* John Wiley and Sons, 1979.

S. Schlenker. *Very High Energy Gamma Rays from the Binary Pulsar PSR B125963.* PhD thesis, Humboldt-Universität Berlin, Germany, 2005.

P. Schneider. *Extragalactic Astronomy and Cosmology.* Springer-Verlag, 2006.

Science and technology review. `https://www.llnl.gov/str/SepOct08/hoffman.html`, 2008.

A. Unsöld and B. Baschek. *The new cosmos: an introduction to astronomy and astrophysics.* Springer-Verlag, 2001.

P. Vincent et al. Performance of the H.E.S.S. Cameras. In *International Cosmic Ray Conference*, volume 5 of *International Cosmic Ray Conference*, pages 2887–+, 2003.

T. C. Weekes et al. Observation of TeV gamma rays from the Crab nebula using the atmospheric Cerenkov imaging technique. *Astrophysical Journal*, 342:379–395, 1989.

T. C. Weekes et al. VERITAS: the Very Energetic Radiation Imaging Telescope Array System. *Astroparticle Physics*, 17:221–243, 2002.

W. T. Welford and R. Winston. *High collection nonimaging optics*. Academic Press, 1989.

C.-A. Wiedner. Site aspects of the hess project, astronomical and visibility conditions. HESS internal notes, 1998.

R. Yamazaki et al. TeV $\gamma$-rays from old supernova remnants. *Monthly Notices of the Royal Astronomical Society*, 371:1975–1982, 2006.

L. Zhang, S. B. Chen, and J. Fang. Nonthermal Radiation from Pulsar Wind Nebulae. *Astrophysical Journal*, 676:1210–1217, 2008.

Tübingen, den 16. Juni 2009.

Hiermit erkläre ich, dass ich die Diplomarbeit mit dem Titel "A detailed analysis of the galactic TeV source HESS J1804-216" selbstständig verfasst und dabei keine anderen als die angegebenen Quelle und Hilfsmittel benutzt habe.

Gabriele Cologna